



# University of HUDDERSFIELD

## University of Huddersfield Repository

Xu, Yongjia

RESEARCH ON KEY TECHNOLOGIES FOR IMPROVEMENT OF MEASUREMENT ACCURACY OF STEREO DEFLECTOMETRY

### Original Citation

Xu, Yongjia (2019) RESEARCH ON KEY TECHNOLOGIES FOR IMPROVEMENT OF MEASUREMENT ACCURACY OF STEREO DEFLECTOMETRY. Doctoral thesis, University of Huddersfield.

This version is available at <http://eprints.hud.ac.uk/id/eprint/34826/>

The University Repository is a digital collection of the research output of the University, available on Open Access. Copyright and Moral Rights for the items on this site are retained by the individual author and/or other copyright owners. Users may access full items free of charge; copies of full text items generally can be reproduced, displayed or performed and given to third parties in any format or medium for personal research or study, educational or not-for-profit purposes without prior permission or charge, provided:

- The authors, title and full bibliographic details is credited in any copy;
- A hyperlink and/or URL is included for the original metadata page; and
- The content is not changed in any way.

For more information, including our policy and submission procedure, please contact the Repository Team at: [E.mailbox@hud.ac.uk](mailto:E.mailbox@hud.ac.uk).

<http://eprints.hud.ac.uk/>

**RESEARCH ON KEY TECHNOLOGIES FOR  
IMPROVEMENT OF MEASUREMENT ACCURACY OF  
STEREO DEFLECTOMETRY**

**YONGJIA XU**

A thesis submitted to the University of Huddersfield in partial fulfilment of the requirements for  
the degree of Doctor of Philosophy

The University of Huddersfield

September 2018

### *Acknowledgements (Preface)*

I would like to thank all the people who has helped me in this research.

First and foremost, I would like to express my sincere gratitude to my supervisor Dr. Feng Gao for his support, guidance, motivation and encouragement during my Ph.D. course. I am forever indebted to him for offering me the opportunity to pursue my doctoral degree and have been a great honour to be his student. His advice on both research as well as on career have been priceless and helped me to be able to perform independent research. I really appreciate the time and effort he spent on reviewing my writings including annual reports, conference/journal papers and this thesis.

I would like to express my sincere gratitude to Professor Dame Xiangqian Jiang for her support in my study and living in Huddersfield. Many thanks to her for the valuable advice and technical assistance in the experiments and research direction. Additionally, I really appreciate all her contributions in of the necessary facilities and funding to undertake this research and supporting my attendances at various conferences outside and inside the UK.

Thanks to all members in the EPSRC Centre for Innovative Manufacturing in Advanced Metrology including Professor Liam Blunt, Mr. Chris Dawson, Dr. Haydn Martin, Dr. Wenhan Zeng, Dr. Tukun Li, Dr. Shan Lou, Dr. Hussam Muhamedsalih, Dr. Qunfen Qi, Dr. Zhen Tong, Dr. Dawei Tang, Dr. Prashant Kumar, Dr. Yuchu Qin, Mr. Christian Young, Mr. Zavid Mohamed, Mr. Tao Zhao, Mr. Duo Li, Miss Yue Liu and Mr. Tao Zhao. You have all made for a wonderful and enjoyable place to work. A special thanks to Professor Zonghua Zhang for the time and effort he spent on guiding my experiment and reviewing my writings.

Last, but certainly not least, I would like to thank my family especially my parents for raising me as well as all the strong supports and profound love. Thanks to my beloved wife Xiaoling Zhang for her understanding, patience, and encouragement in all my pursuits. I cannot image how to go through these days when I worked to midnight without her company.

## *Abstract*

Obtaining three-dimensional (3D) shape data of specular surfaces plays an increasingly important role in the quality control and function evaluation of high value-added industry, such as space, automobile, Photovoltaics, integrated circuits and so on.

In recent years, stereo deflectometry has been widely studied and applied for obtaining form information of freeform specular surfaces. Theoretically, the global form measurement accuracy of stereo deflectometry can be up to nanometre. However, the sources of errors limit the measurement accuracy of the current stereo deflectometry application at the scale of submicron.

To this end, this thesis documents the design and development of the calibration methods, error analysis and compensation in the field of stereo deflectometry. To limit the influence of system distortion, a novel holistic calibration technique utilising iterative distortion compensation algorithm has been designed and developed. A search algorithm with an objective function has been developed to solve the low-accuracy initial value problem caused by image distortion and imaging model error. With the intention of decreasing the impact of the phase error in stereo deflectometry, a novel imaging model has been explored the nexus between phase inaccuracy and gradient error. The period of fringe displayed on displaying screen and pixel size of the screen has been studied to augment measurement accuracy through taking into account their impact on sampling phase inaccuracy and gradient miscalculation. In addition, four geometric parameters of a stereo deflectometry system are analysed and evaluated. These are the distance between the main camera and the measured object surface, the angle between main camera ray and surface normal, the distance between the fringe-displaying screen and object and the angle between the main camera and the reference camera. The influence of the geometric parameters on the measurement accuracy is evaluated.

A stereo deflectometry system is designed, optimised and calibrated based on the investigation of this thesis. Two evaluation experiments have been conducted and experimental results indicate the system's measurement accuracy can achieve tens of nanometres.

## Publications

Six peer-reviewed journal papers and three conference papers have been produced based on the works in this thesis.

### Peer-reviewed Journal Papers

**Y. Xu**, F. Gao and X. Jiang (2018). "Enhancement of measurement accuracy of optical stereo deflectometry based on imaging model analysis." Optics and Lasers in Engineering **111**: 1-7.

**Y. Xu**, F. Gao, Z. Zhang and X. Jiang (2018). "A holistic calibration method with iterative distortion compensation for stereo deflectometry." Optics and Lasers in Engineering **106**: 111-118.

**Y. Xu**, F. Gao, Z. Zhang and X. Jiang (2018). "A calibration method for non-overlapping cameras based on mirrored absolute phase target." The International Journal of Advanced Manufacturing Technology: 1-7.

**Y. Xu** , F. Gao, H. Ren, Z. Zhang and X. Jiang (2017). "An iterative distortion compensation algorithm for camera calibration based on phase target." Sensors **17**(6): 1188.

**Y. Xu**, F. Gao and X. Jiang (2018). "A search algorithm for accuracy improvement of holistic calibration of stereo deflectometry." Sensors In peer review.

**Y. Xu**, F. Gao and X. Jiang (2018). "performance analysis and evaluation of geometric parameters in stereo deflectometry." Engineering accepted.

### Refereed Conference Papers

**Y. Xu**, F. Gao, Z. Zhang and X. Jiang (2017). "A calibration method for non-overlapping cameras based on mirrored phase target." In: The 13th International Symposium on Measurement Technology and Intelligent Instruments, 22-25 September 2017, Xi'an, Shanxi, China

F. Gao, **Y. Xu**, H. Ren, Z. Zhang and X. Jiang (2016). "A novel camera calibration method for deflectometry system." In: 16th International Conference and Exhibition, 30<sup>th</sup> May-3rd June 2016, Nottingham, UK , pp. 527-531

F. Gao, **Y. Xu**, and X. Jiang (2018). "Stereo deflectometry imaging system optimisation for high accurate surface form measurement." In: euspen's SIG meeting committee, 27<sup>th</sup>-29<sup>th</sup> November 2018, Cachan, France, accepted.

## Statement of Publications Arising from this Thesis

The following publications have arisen from my research detailed in this thesis:

1. "Enhancement of measurement accuracy of optical stereo deflectometry based on imaging model analysis."

Y. Xu, F. Gao and X. Jiang (2018) Optics and Lasers in Engineering **111**: 1-7.

2. "A holistic calibration method with iterative distortion compensation for stereo deflectometry."

Y. Xu, F. Gao, Z. Zhang and X. Jiang (2018) Optics and Lasers in Engineering **106**: 111-118.

3. "A calibration method for non-overlapping cameras based on mirrored absolute phase target."

Y. Xu, F. Gao, Z. Zhang and X. Jiang (2018) The International Journal of Advanced Manufacturing Technology: 1-7.

4. "An iterative distortion compensation algorithm for camera calibration based on phase target."

Y. Xu, F. Gao, H. Ren, Z. Zhang and X. Jiang (2017) Sensors **17**(6): 1188.

5. "Performance analysis and evaluation of geometric parameters in stereo deflectometry."

Y. Xu, F. Gao and X. Jiang (2018). Engineering **4**(6), 806-815.

6. "A search algorithm for accuracy improvement of holistic calibration of stereo deflectometry."

Y. Xu, F. Gao and X. Jiang (2018) Sensors In peer review.

7. "A calibration method for non-overlapping cameras based on mirrored phase target."

Y. Xu, F. Gao, Z. Zhang and X. Jiang (2017). In: The 13th International Symposium on Measurement Technology and Intelligent Instruments, 22-25 September 2017, Xi'an, Shanxi, China

8. "A novel camera calibration method for deflectometry system."

F. Gao, Y. Xu, H. Ren, Z. Zhang and X. Jiang (2016). In: 16th International Conference and Exhibition, 30th May-3rd June 2016, Nottingham, UK , pp. 527-531

9. "Stereo deflectometry imaging system optimisation for high accurate surface form measurement."

F. Gao, Y. Xu, and X. Jiang (2018). In: euspen's SIG meeting committee, 27<sup>th</sup>-29<sup>th</sup> November 2018, Cachan, France, accepted.

**Contribution of the candidate for the above publications: I performed all the researches and wrote the entire manuscripts with minor input and editorial changes from my co-author. It is indicated where text from these publications have been reproduced in this thesis.**

## *Table of Contents*

### **Contents**

<b>1. Introduction .....</b>	<b>21</b>
1.1 Overview .....	21
1.1.1 Coordinate measuring machine .....	21
1.1.2 Interferometer .....	22
1.1.3 Structure light projection .....	24
1.1.4 Phase measuring deflectometry .....	25
1.2 Motivation .....	26
1.3 Aim and objectives .....	27
1.4 Thesis organization.....	27
<b>2. Overview of deflectometry .....</b>	<b>29</b>
2.1 Basic measurement principle.....	29
2.2 Applications of deflectometry .....	30
2.3 Typical technologies based on deflectometry .....	33
2.3.1 Active fringe reflection deflectometry .....	33
2.3.2 Software configurable optical test system (SCOTS).....	34
2.3.3 Microdeflectometry .....	36
2.3.4 Direct phase measuring deflectometry .....	37
2.3.5 Stereo deflectometry.....	38
2.4 The challenges in stereo deflectometry .....	39
2.5 Summary.....	45
<b>3. Key techniques in stereo deflectometry .....</b>	<b>47</b>
3.1 Phase shifting algorithm .....	47
3.2 Phase unwrapping algorithm .....	50

3.3	Gradient calculation algorithm .....	55
3.4	Reconstruction algorithms based on gradient integration .....	56
3.5	Summary.....	60
<b>4.</b>	<b>Improvement of camera calibration accuracy .....</b>	<b>61</b>
4.1	Principle of camera calibration method.....	61
4.1.1	Phase target.....	61
4.1.2	Calibration with iterative distortion compensation algorithm .....	62
4.1.3	Compensation algorithm for phase target error .....	64
4.2	Results and discussion .....	67
4.2.1	Simulation study .....	67
4.2.2	Experiment study .....	69
4.3	Summary.....	72
<b>5.</b>	<b>Calibration of non-overlapping camera system.....</b>	<b>73</b>
5.1	Principle of the proposed calibration method for non-overlapping cameras system .....	74
5.2	Experiment and results .....	77
5.2.1	Simulation study .....	77
5.2.2	Experimental study and discussion.....	78
5.3	Summary.....	79
<b>6.</b>	<b>Holistic system calibration method for stereo deflectometry .....</b>	<b>81</b>
6.1	Holistic calibration method with iterative distortion compensation.....	81
6.1.1	Principle of the proposed holistic calibration method .....	81
6.1.2	Experiment and results .....	86
6.2	Robustness improvement of holistic calibration .....	92
6.2.1	Principle of the proposed search algorithm with an evaluation function .....	92
6.2.2	Experiment and results .....	96

6.3	Summary.....	102
<b>7.</b>	<b>Analysis of phase error influence .....</b>	<b>103</b>
7.1	Principle of the analysis method.....	103
7.2	Experiments and results.....	108
7.3	Summary.....	112
<b>8.</b>	<b>Analysis of geometric parameters influence .....</b>	<b>113</b>
8.1	Principle of the analysis method of the geometric parameters.....	113
8.1.1	Influence of $\gamma$ .....	115
8.1.2	Influence of $L_s$ .....	116
8.1.3	Influence of $L_d$ .....	118
8.1.4	Influence of $\mathcal{G}$ .....	119
8.2	Simulation test.....	121
8.2.1	Verification of the analysis of $\gamma$ .....	121
8.2.2	Verification of the analysis of $L_s$ .....	122
8.2.3	Verification of the analysis of $L_d$ .....	122
8.2.4	Verification of the analysis of $\mathcal{G}$ .....	123
8.3	Actual experiments.....	124
8.4	Summary.....	128
<b>9.</b>	<b>Experiment evaluation and future work .....</b>	<b>129</b>
9.1	Experiment evaluation.....	129
9.1.1	System and measurement results.....	129
9.1.2	Summary.....	134
9.2	Conclusions and future work.....	135
9.2.1	Summary of contributions .....	135

9.2.2 Future work.....	136
<b>References .....</b>	<b>138</b>

### *List of Tables*

Table 5.1 Comparison between the calibration results and the true value. 78

Table 5.2 Calibration result with experimental data. 79

## *List of Figures*

Figure 2.1 Basic measurement principle of deflectometry. ....	29
Figure 2.2 Measurement of a car window using deflectometry. (a) The measured car window; (b) the obtained window shape using deflectometry; (c) shape after removing parabolic; (d) measurement fragment; (e) the acquired curvature. (Bothe, Li et al. 2004) .....	30
Figure 2.3 Measurement of a painted car door. (a) The measured car door; (b) the obtained form information of the door; (c) the obtained microstructure. (Bothe, Li et al. 2004) .....	31
Figure 2.4 Measurement of an eyeglass. (a) The measured glass; (b) an image of the glass with fringe information; (c) the obtained form of the glass. (Bothe, Li et al. 2004).....	31
Figure 2.5 Some reconstructed 3D data of the measured water wave. (a) , (b), (c), (d) , (e), (f) demonstrate the water wave at different moments. (Huang, Ng et al. 2011).....	32
Figure 2.6 Measure a multi-mirror array based on deflectometry. (a) The measured array; (b) the measurement result. (Liu, Huang et al. 2017) .....	32
Figure 2.7 Measurement principle of AFRD. ....	34
Figure 2.8 Comparison of SCOTS and Hartmann test (a) Principle of SCOTS, (b) principle of Hartmann test. (Su, Parks et al. 2010).....	35
Figure 2.9 Principle of microdeflectometry (G.Hausler, C.Richter et al. 2008).....	36
Figure 2.10 Principle of DPMD (Liu, Huang et al. 2017, Zhao, Gao et al. 2018).....	37
Figure 2.11 The measurement principle of stereo deflectometry.....	38
Figure 3.1 Horizontal fringe patterns. (a) $n=0$ ; (b) $n=1$ ; (c) $n=2$ ; (d) $n=3$ ; (e) $n=4$ ; (f) $n=5$ ; (g) $n=6$ ; (h) $n=7$ . ....	48
Figure 3.2 Vertical fringe patterns. (a) $n=0$ ; (b) $n=1$ ; (c) $n=2$ ; (d) $n=3$ ; (e) $n=4$ ; (f) $n=5$ ; (g) $n=6$ ; (h) $n=7$ . ....	48

Figure 3.3 Wrapped phase map of horizontal fringe patterns. ....	49
Figure 3.4 Wrapped phase map of vertical fringe patterns. ....	50
Figure 3.5 The principle of heterodyne phase unwrapping algorithm. ....	51
Figure 3.6 Horizontal wrapped phase maps. (a) Fringe number is 9; (b) fringe number is 8; (c) fringe number is 6. ....	53
Figure 3.7 Vertical wrapped phase maps. (a) Fringe number is 9; (b) fringe number is 8; (c) fringe number is 6. ....	53
Figure 3.8 Horizontal absolute unwrapped phase map. ....	54
Figure 3.9 Vertical absolute unwrapped phase map. ....	54
Figure 3.10 The measurement principle of stereo deflectometry.....	55
Figure 3.11 Principle of gradient integration method. ....	56
Figure 4.1 The phase target used in camera calibration process. (a) One of vertical sinusoidal fringe patterns; (b) one of horizontal sinusoidal fringe patterns; (c) vertical absolute phase; (d) horizontal absolute phase. ....	62
Figure 4.2 Phase target is placed at arbitrary poses. ....	62
Figure 4.3 Summary the calibration process. ....	64
Figure 4.4 Fringe distortion on a captured fringe pattern. (a) A pattern captured by CCD camera when phase target is placed at camera's focus position; (b) phase error; (c) a pattern captured by CCD camera when phase target is placed at camera's defocus position. ....	65
Figure 4.5 Principle of fitting and interpolation method.....	66
Figure 4.6 The variety of reprojection error, error of rotation matrix and error of translation matrix along with the variety of window size. ....	67

Figure 4.7 True camera pixel and distorted camera pixel. (a) Influence of radial distortion ; (b) influence of eccentric distortion; (c) influence of thin prism distortion; (d) overall influence of radial distortion, eccentric distortion and thin prism distortion. .... 69

Figure 4.8 Calibration result obtained with the studied camera calibration technique. (a) Reprojection error of calibration along x and y direction; (b) reprojection error expressed in terms of pixel coordinate. 8 colours are used to distinguish different calibration poses. .... 69

Figure 4.9 Setup for testing the studied camera calibration technique. .... 70

Figure 4.10 The obtained camera distortion. (a) Camera distortion of the chosen camera pixels; (b) enlargement of the right-top corner of (a). Different colours are used to distinguish different calibration poses. .... 71

Figure 4.11 Comparison between the studied camera calibration technique and Zhang’s calibration method. (a) Calibration error obtained of Zhang’s method without using fitting optimization technique; (b) calibration error expressed in pixel coordinate of Zhang’s method without using fitting optimization technique; (c) calibration error expressed in pixel coordinate of Zhang’s method by using fitting optimization technique; (d) calibration error of the studied camera calibration technique without using fitting optimization technique; (e) calibration error expressed in pixel coordinate of the studied camera calibration technique without using fitting optimization technique; (f) calibration error expressed in pixel coordinate of the studied camera calibration technique by using fitting optimization technique. Different colours are used to distinguish different calibration poses..... 71

Figure 5.1 Stereo deflectometry can be treated as a non-overlapping camera systems when doing calibration..... 73

Figure 5.2 The principle of the studied calibration technique..... 74

Figure 5.3 Summary of the studied calibration technique’s workflow. .... 76

Figure 5.4 A simulated non-overlapping camera system. .... 77

Figure 6.1 The structure of a stereo deflectometry system. ....	82
Figure 6.2 Summarization of the calibration process of the studied calibration technique. ....	85
Figure 6.3 The simulation setup. ....	86
Figure 6.4 Effect of the simulated camera distortion. (a) Effect of radial distortion ; (b) effect of eccentric distortion; (c) effect of thin prism distortion; (d) an overall effect of three kinds of camera distortion. ....	87
Figure 6.5 Comparison of calibration results. (a) Calibration results calculated when no distortion exists in the system; (b) calibration result calculated based on traditional calibration approach; (c) calibration result obtained with the studied calibration technique. ....	88
Figure 6.6 Comparison of measurement results. (a) Measurement result acquired based on the standard calibration result; (b) measurement result acquired based on traditional calibration approach; (c) measurement result acquired based on the studied calibration approach. ....	88
Figure 6.7 The experiment setup. ....	89
Figure 6.8 Calibration result of main camera and reference camera. (a) Calibration error along x direction of main camera obtained based on traditional calibration method; (b) calibration error along y direction of main camera obtained based on traditional calibration method; (c) calibration error along x direction of reference camera obtained based on traditional calibration method; (d) calibration error along y direction of reference camera obtained based on traditional calibration method; (e) calibration error along x direction of main camera obtained based on the studied calibration technique; (f) calibration error along y direction of main camera obtained based on the studied calibration technique; (g) calibration error along x direction of reference camera obtained based on the studied calibration technique; (h) calibration error along y direction of reference camera obtained based on the studied calibration technique. ....	89
Figure 6.9 The calculated gradient data with traditional calibration method and the studied calibration technique. (a) Gradient data along x direction obtained with traditional calibration method; (b) gradient data along y direction obtained with traditional calibration method; (c)	

gradient data along x direction obtained with the studied calibration technique; (d) gradient data along y direction obtained with the studied calibration technique. ....	91
Figure 6.10 A comparison between the measurement results. (a) The measurement error of traditional calibration method; (b) the measurement error of the studied calibration technique. .	92
Figure 6.11 The chosen camera pixels for calibration calculation. (a) Previous holistic calibration technique; (b) the proposed calibration method. ....	92
Figure 6.12 The flowchart of the studied calibration technique. ....	96
Figure 6.13 The tested stereo deflectometry system. ....	97
Figure 6.14 Relation between $RMS(p)$ and $2d$ . ....	98
Figure 6.15 Relation between $\lambda$ and $2d$ . ....	98
Figure 6.16 Comparison of accuracy of initial value calculation. (a) Without the proposed calibration method; (b) with the proposed calibration method. ....	99
Figure 6.17 RMS of $\Delta m$ . ....	100
Figure 6.18 Calibration error. (a) Based on the initial value obtained without the studied calibration technique; (b) based on the initial value obtained with the studied calibration technique. ....	100
Figure 6.19 RMS of calibration error. ....	101
Figure 6.20 Comparison of measurement results. (a) Measurement result without the studied calibration technique; (b) measurement result with the studied calibration technique. ....	102
Figure 7.1 The studied mathematical model for stereo deflectometry. ....	103
Figure 7.2 The relation between $n_p$ and phase error. ....	109
Figure 7.3 The variation of gradient error. ....	109

Figure 7.4 Phase error of iPad Pro and traditional screen.....	110
Figure 7.5 The simulation setup.....	111
Figure 7.6 Measurement result. (a) Measurement result obtained when $p$ equals 0.297 mm; (b) measurement result obtained when $p$ equals 0.128 mm.....	112
Figure 8.1 The arrangement of stereo deflectometry. ....	113
Figure 8.2 The relationship between the geometric parameters and error sources. ....	114
Figure 8.3 The procedures of error analysis.....	115
Figure 8.4 Relative positions of the imaging plane of a camera, the measured surface, and the mirrored screen.....	115
Figure 8.5 Illustration of the influence of $L_s$ .....	116
Figure 8.6 Illustration of the influence of $L_d$ .....	118
Figure 8.7 Illustration of the influence of $\vartheta$ .....	119
Figure 8.8 Enlarged view of the calculated normal values. (a) The enlarged view of $S_1$ ; (a) The enlarged view of $S_2$ .....	120
Figure 8.9 The obtained relation between geometric parameters and measurement error based on simulation results. (a) Relation between $\gamma$ and measurement error; (b) relation between $L_s$ and measurement error; (c) relation between $L_d$ and measurement error; (d) relation between $\vartheta$ and measurement error.....	123
Figure 8.10 The setup of stereo deflectometry system.....	124
Figure 8.11 Relation between $L_s$ and phase error. ....	125

Figure 8.12 Relation between mirrored fringe pattern and mirror curvature. (a) Flat mirror when  $L_s$  is 80 mm; (b) concave mirror with 200 mm radius of curvature when  $L_s$  is 80 mm; (c) concave mirror with 100 mm radius of curvature when  $L_s$  is 80 mm; (d) flat mirror when  $L_s$  is 120 mm; (e) concave mirror with 200 mm radius of curvature when  $L_s$  is 120 mm; (f) concave mirror with 100 mm radius of curvature when  $L_s$  is 120 mm..... 126

Figure 8.13 The obtained relation between geometric parameters and measurement error based on actual experimental results. (a) Relation between  $\gamma$  and measurement error; (b) relation between  $L_s$  and measurement error; (c) relation between  $L_d$  and measurement error; (d) relation between  $\rho$  and measurement error. .... 127

Figure 9.1 A designed stereo deflectometry system. .... 130

Figure 9.2 One of the captured images with fringe information in the main camera. (a) One of the captured images with horizontal fringe pattern; (b) one of the captured images with vertical fringe pattern. .... 131

Figure 9.3 The obtained absolute phase maps of the measured optical flat in main camera. (a) Horizontal absolute phase map; (b) vertical absolute phase map. .... 131

Figure 9.4 The obtained gradient information. (a) Gradient data along x direction; (b) gradient data along y direction. .... 132

Figure 9.5 Measurement error of an optical flat..... 132

Figure 9.6 A concave mirror was measured by the system. (a) The measured concave mirror; (b) one of the captured images from the main camera with deformed fringe information..... 133

Figure 9.7 The obtained absolute phase maps of the measured concave mirror in the main camera. (a) Horizontal absolute phase map; (b) vertical absolute phase map. .... 134

Figure 9.8 Measurement result of a stock concave mirror. (a) The obtained form of the mirror; (b) the difference between the measurement result and the surface parameters provided by the manufacturer..... 134

*List of abbreviations*

CMM	Coordinate measuring machine
CNC	Computerized numerical control
OPD	Optical path difference
PSI	Phase shifting interferometer
WLI	White light interferometry
PMD	Phase measuring deflectometry
CCD	Charge coupled device
SCOTS	Software Configurable Optical Test System
DPMD	Direct phase measuring deflectometry
SWLI	Scanning white light interferometry
LCD	Liquid crystal display
3D	Three-dimensional
2D	Two-dimensional
FOV	Field of view
HEC	Hand-eye calibration
DOF	Depth of field
CSI	Coherence scanning interferometry
TFHTPU	Three-frequency heterodyne temporary phase unwrapping

RMS	Root mean square
PV	Peak-Value
VSI	Vertical scanning interferometry

# 1. Introduction

## 1.1 Overview

Freeform specular surface commonly refers to the surfaces having non-symmetric shapes and reflection property ([Pollicove 2000](#), [Nelson E. Claytor 2004](#), [Jiang, Scott et al. 2007](#), [Jiang and Whitehouse 2012](#), [Thompson 2012](#), [Evans and Davies 2015](#)). Freeform specular surfaces can boost systemic function, shorten the complexity of system design and structure, and/or enhance systemic aesthetic and integrities ([Fang, Zhang et al. 2013](#), [Duerr, Nie et al. 2015](#)) ([Fang, Zhang et al. 2013](#), [Duerr, Nie et al. 2015](#)). Over the past decades freeform specular surfaces are applied in various applications, for instance green energy, aerospace, automotive, illumination, biomedical engineering, for attractive functional, geometric features and aesthetical reasons ([Savio, De Chiffre et al. 2007](#), [Fang, Zhang et al. 2013](#), [Evans and Davies 2015](#), [Williamson 2015](#)).

Numbers of methods have been investigated for measuring the form of freeform surface ([Whitehouse 2002](#)). According to whether the sensing probe is in contact with the measured object during a measurement, these methods can be categorised as non-contact measurement and contact measurement. Contact measurement generally uses tactile sensors such as gauges and probes to gather shape data via physically touching the measured surface. Probes are required to run perpendicular to the surface under test for contact measurement methods ([Li and Gu 2004](#), [Li and Gu 2005](#)). Contact type coordinate measuring machine (CMM) is a common example of this kind of methods. When contact type CMM operates, a contact probe moves along the measured workpiece surface to amass the surface's meticulous dimensional information. Optical surface measurement technique is an important type of non-contact measurement, which operates based on the principle that light can travel without any contact. Several optical surface measurement methods with different optical principle have been developed such as non-contact CMM technology, interferometry, structure light projection technique, and phase measuring deflectometry.

### 1.1.1 Coordinate measuring machine

The first CMM ([McMurtry 1982](#), [Hemmelgarn, Bell et al. 2000](#), [Pettersson 2009](#), [Ferrari 2010](#)) was developed by a British company named FERRANTI ([Hocken and Pereira 2016](#)). Measuring

method of the machine is to record coordinate value by foot pedal after its probe touches the measured workpiece, and then use calculator to calculate the location relationship between elements. With the rapid development of computer technology, CMM entered the era of CNC (Computerized numerical control) control and became capable of completing the measurement of complex mechanical parts and freeform surface. CMM consists of a measurement probe and a rectangular coordinate system established by three mutually perpendicular motion axes. When conducting measurement, the probe moves along the form of the measured surface. The trajectory of the probe within the rectangular coordinate system is recorded in a computer and is processed by corresponding software. After conducting the process, point cloud data reflecting the form of the measured object can be obtained. According to the type of probe, CMM can be divided into non-contact CMM and contact type CMM ([Malacara 2007](#), [Leach 2011](#), [Fang, Zhang et al. 2013](#)). The probe of contact type CMM is required to touch the measured surface and therefore has a potential to damage the tested surface by stylus tip, especially when optical components are being inspected. In addition, contact type CMM are not capable of measuring soft surface. Moreover, non-contact CMM uses probe based on optical principle and can achieve non-contact scanning. However, non-contact CMM is affected by the reflection characteristics of the measured surface, such as colour, slope and so on. Environmental light and the focalization of the measuring lens have an impact on its measurement accuracy as well.

CMM has been well accepted in industry because its large measurement range. However, CMM is point-by-point measurement and therefore has low measurement speed.

### **1.1.2 Interferometer**

Optical interferometry ([Dörband and Seitz 2001](#), [Hariharan 2003](#), [Wyant 2003](#)) is a technology based on interference phenomena. The interference phenomena of light are commonly seen in daily life, such as the multi-coloured fringes in oil slick or soap bubble. Another example is the colour fringes in a thin film bounded by two transparent plates when they are tightly placed, which is also known as Newton rings. Newton rings were described by Boyle and Hooke independently in 17th century and were widely adopted to inspect optical components from then on ([Wyant 2002](#), [Schreiber and Bruning 2007](#)). Newton rings are commonly regarded as the starting point of optical interferometry. In 1882, the first interferometric instrument was developed by the renowned

physicist Albert Michelson ([Wyant 2002](#), [Schreiber and Bruning 2007](#)). Light in an interferometer is produced from an illuminating source. Two beams are split from the light and propagate in different optical paths. Interference fringes are generated when the beams with optical path difference (OPD) recombine. The interference fringes exhibit high sensitivity to the OPD. In the beginning, interferometers were mainly applied in dimensional metrology. Since the 1970s, with the development of the relevant fundamental technologies, such as computer science, laser technology and image sensors, interferometers found wide applications in surface metrology and became increasingly important. Interferometry technology developed rapidly due to the driving force brought by the huge market.

Interferometric technologies can be classified into two types according to the employed illuminating source, namely monochromatic interferometry and white light interferometry. Monochromatic interferometry, such as phase shifting interferometer (PSI) ([Sommargren 1999](#), [Schreiber and Bruning 2007](#)), is able to inspect surfaces with subnanometer scale vertical resolution and finds broad applications in the quality check of components with relatively smooth surfaces. However, due to the limitation posed by the well-defined  $2\pi$  phase ambiguity problem, PSI is not appropriate to inspect discontinuous surfaces. White light interferometry (WLI) ([Deck and De Groot 1994](#), [Larkin 1996](#), [Wyant 2002](#)) which adopts a broadband illumination source is widely adopted for determining the optical path differences between the points on the surface under test and the corresponding points on the reference surface with no ambiguity ([Bowe and Toal 1998](#), [Kou, Wang et al. 2012](#), [Tang, Zhou et al. 2014](#)). Apart from academic research, optical interferometry is also very popular in industries. For instance, vertical scanning interferometry (VSI) ([Harasaki, Schmit et al. 2000](#), [Harasaki and Wyant 2000](#)), also known as scanning white light interferometry (SWLI) ([Deck and De Groot 1994](#), [Sandoz 1997](#)) or coherence scanning interferometry (CSI) ([Lee and Strand 1990](#), [de Groot 2011](#)), are widely utilized in micro-optic and micro-electronic manufacturing industries.

Although optical interferometry features non-contact measurement with high accuracy, it has a shortcoming of being sensitive to environmental noise ([Adhikari 2004](#)). To overcome this issue, interferograms ought to be captured very fast by adopting a high-speed camera. Besides,

compensation of the environmental noise can also effectively increase the stability of the instruments and improve the measurement accuracy ([Jiang, Wang et al. 2010](#)).

### 1.1.3 Structure light projection

Structure light projection techniques ([Pages, Salvi et al. 2003](#), [Gorthi and Rastogi 2010](#), [Zhang 2010](#)) utilizes a light resource, such as a projector, to project encoded patterns to the measured surface. The patterns can be sinusoidal ([Gorthi and Rastogi 2010](#)), binary or Ronchi ([Pan, Huang et al. 2005](#)), triangular ([Jia, Kofman et al. 2007](#)), saw tooth ([Quan, Chen et al. 2010](#)), and so on. The form of the object surface leads to a deformation of the encoded patterns. Form data of the surface are obtained based on the deformation through the calculation of particular algorithms. Among these patterns, sinusoidal pattern is most commonly investigated because absolute phase maps with sub-pixel accuracy can be obtained. Depth data are acquired by applying calibration to create the association between absolute phase and depth data. Phase wrapping techniques, such as phase shifting technique ([Pan, Huang et al. 2006](#), [Quan, Chen et al. 2010](#), [Zhang, Van Der Weide et al. 2010](#)), Fourier transform technique ([Takeda, Ina et al. 1982](#), [Brigham and Brigham 1988](#), [Kemao 2007](#)), and wavelet transform technique ([Dursun, Özder et al. 2004](#), [Huang, Kemao et al. 2010](#)), have been investigated to extract phase information from a captured single fringe pattern or multiple patterns. Phase shifting technique demands  $n$  ( $n \geq 3$ ) fringe patterns to obtain a wrapping phase map and the fringe patterns are required to be moved according to a specified sequence with a step size of  $2\pi/n$ . Fourier transform technique and wavelet transform technique transform fringes information from time domain to frequency domain, and extract useful frequency information for analysis. Though Fourier transform technique and wavelet transform technique only demands one fringe pattern to acquire a wrapping phase map, the phase calculation accuracy of a surface with large gradient or discontinuities based on the two techniques cannot reach the accuracy level of phase shifting technique. Phase unwrapping algorithms have been studied for acquiring absolute phase map from wrapped phase map. Spatial phase unwrapping algorithm unwraps a wrapped phase map by simply adding or subtracting multiples of  $2\pi$  and therefore has a disadvantage of error inheritance. Temporal phase unwrapping algorithm ([Huntley and Saldner 1997](#), [Huntley and Saldner 1997](#), [Saldner and Huntley 1997](#)) are proposed to solve the error inheritance problem, however the algorithm requires multiple patterns with different fringe frequency and therefore decreases measurement speed. In order to increase measurement

speed, colour fringe projection technique ([Huang, Hu et al. 1999](#), [Zhang, Towers et al. 2006](#), [Zhang 2012](#)) has been researched. In this technique, different colour channels encode fringe patterns with different frequencies; therefore, several patterns can be combined in a colour fringe pattern.

Although structure light projection techniques can measure form information of a diffused object surface in a non-contact manner with a good speed, it cannot measure specular surface due to the limit of measurement principle.

#### **1.1.4 Phase measuring deflectometry**

Phase measuring deflectometry (PMD) ([Knauer, Kaminski et al. 2004](#), [Tang, Su et al. 2008](#), [Tang, Su et al. 2009](#)) utilizes the reflective properties of specular surfaces and extracts 3D shape of the work piece under test by analysing the reflected phase information. The measured surface can be reconstructed based on gradient information ([Ettl, Kaminski et al. 2008](#), [Huang, Idir et al. 2015](#), [Ren, Gao et al. 2016](#)) or the relationship between depth and phase data ([Liu, Huang et al. 2017](#), [Zhao, Gao et al. 2018](#)). Decades ago, the pioneers in shape measurement had already used the basic measurement principle of this technology to measure specular surface. For example, Ritter et al. ([Ritter and Hahn 1983](#)) published a paper in 1983 to analyse reflection grating method. A camera is utilized to capture a grating plane through the reflection of surface under test. Gradient of the surface point is calculated based on the corresponding grating plane point and its image point in a camera. However, there is still one degree of freedom remains because series of combinations of positions and gradients can result in the same observed result. Therefore, this method can only qualitatively inspect a specular surface. In the early 2000s, Petz et al. ([Petz and Ritter 2001](#)) investigated a reflection grating method based on two parallel grating planes, which can realize quantitative measurement of a reflecting surface. Knauer et al. ([Knauer, Kaminski et al. 2004](#)) presents a method for measuring freeform specular objects and used the name of phase measuring deflectometry for the first time in 2004. In Knauer's paper, measurement principle, physical limits, and calibration process of PMD are discussed in detail. In addition, the concept and measurement principle of stereo deflectometry are first proposed in this paper. After that, PMD has been widely spread, and numbers of research institutes in the world have begun to study this technology. There are many advantages for PMD compared with other specular surface measurement techniques. Firstly, PMD is a full-field measurement technique and have a large

measurement field, which makes it have a superiority compared with interferometer and non-contact CMM in measurement speed when inspecting large specular surface. Secondly, PMD can measure freeform reflective surface in a non-contact manner, which is a protruding advantage over contact type CMM and fringe projection technique.

## 1.2 Motivation

Stereo deflectometry ([Knauer, Kaminski et al. 2004](#), [Häusler, Faber et al. 2013](#), [Ren, Gao et al. 2016](#)) is an important PMD technique. Theoretically, the form measurement accuracy of stereo deflectometry can be up to nanometre, which makes this technology to be a comparable method to interferometry ([Häusler, Faber et al. 2013](#)). However, error sources such as calibration error, phase error, and imperfect performance of the components in stereo deflectometry, limit the measurement accuracy of the current stereo deflectometry to submicron level ([Knauer, Kaminski et al. 2004](#), [Häusler, Faber et al. 2013](#), [Ren, Gao et al. 2016](#)). Therefore, it is essential to research the key techniques of stereo deflectometry in order to improve the measurement accuracy of the system.

Calibration ([Zhang 2000](#), [Bittar and Bartel 2001](#), [Heuermann 2006](#)) is an important step for any measurement system. Stereo deflectometry carries out measurement based on the principle of geometrical optics. Imaging relations in terms of stereo deflectometry is expressed with mathematical model ([Knauer, Kaminski et al. 2004](#), [Häusler, Faber et al. 2013](#), [Ren, Gao et al. 2016](#)). However, the difference between real imaging relations and the mathematical model affects calibration accuracy ([Knauer, Kaminski et al. 2004](#), [Ren, Gao et al. 2015](#)). Therefore, new camera and system calibration methods are required to be explored to eliminate the influence of imaging model error and to increase stereo deflectometry's calibration accuracy. Moreover, iterative optimization algorithm is commonly applied in calibration ([Huang, Idir et al. 2015](#), [Ren, Gao et al. 2015](#), [Ren, Gao et al. 2016](#)). Factors, distortion ([Weng, Cohen et al. 1992](#), [Zhang, He et al. 2003](#)) for instance, lead to the iterative process cannot converge correctly. Therefore, a calibration method is needed to be investigated for improving calibration stability.

Stereo deflectometry extracts shape data of an object under test from phase information, hence phase error has a serious impact on measurement accuracy ([Wu, Yue et al. 2015](#)). Plenty of factors, such as characteristic of fringe-displaying screen ([Petz, Fischer et al. 2013](#)) and layout of

components in stereo deflectometry, have an influence on the level of phase noise. Moreover, these factors affect phase noise level in comprehensive ways. Therefore, it is essential to study influence factors of phase error in a stereo deflectometry through mathematical modelling analysis, simulation and experiment.

### **1.3 Aim and objectives**

The aim of this research is to improve the measurement accuracy of stereo deflectometry by investigating key techniques of the system. The objectives of this research are listed as follows:

- To study a new camera calibration method for stereo deflectometry. This method will also benefit other camera-based optical measurement systems to improve calibration accuracy.
- To investigate a new method for the calibration of non-overlapping camera system. This method will be helpful to investigate the systemic calibration of stereo deflectometry.
- To develop a new systemic calibration method for a stereo deflectometry system. This method will improve the systemic calibration accuracy of stereo deflectometry.
- To research a mathematic model for analysing the impact of phase error. Methods will be discovered based on this model to decrease phase error's influence in a stereo deflectometry system.
- To develop a mathematic model to analyse the influence of the geometric parameters of stereo deflectometry on gradient calculation accuracy. Geometric parameters of a stereo deflectometry system will be optimised based on this analysis to increase measurement accuracy.

### **1.4 Thesis organization**

In-depth analyses and techniques are presented in this thesis to improve stereo deflectometry's measurement accuracy. Nine chapters are organised:

- Chapter 2 gives an overview of deflectometry. The basic measurement principle and the applications of deflectometry are introduced. Several typical technologies based on deflectometry are briefly described. In addition, a detailed literature review of stereo deflectometry is presented in this chapter.

- Chapter 3 gives an overview of some important algorithms of stereo deflectometry by introducing coding technique of the displayed fringe patterns, phase unwrapping algorithm, normal calculation algorithm and reconstruction algorithm.
- Chapter 4 describes a camera calibration method based on phase target to increase camera calibration accuracy.
- Chapter 5 presents a calibration method for non-overlapping camera system.
- Chapter 6 describes a systemic calibration method for stereo deflectometry. A search algorithm is also presented for the improvement of systemic calibration stability.
- Chapter 7 represents an imaging model to study the relationship between phase error and gradient miscalculation.
- Chapter 8 describes an analysis of the influence of a stereo deflectometry system's geometric parameters.
- Chapter 9 presents evaluation experiments to test the measurement accuracy of a stereo deflectometry system that is optimized and calibrated based on the above investigations. A summary of contributions and future work are also given.

## 2. Overview of deflectometry

An overview of deflectometry is presented in this chapter. Section 2.1 introduces the basic measurement principle of deflectometry, and section 2.2 presents the applications of current deflectometry. Several typical technologies based on deflectometry are described in section 2.3. In section 2.4, a detailed literature review of stereo deflectometry is presented. A brief summary is given in the last section of this chapter.

### 2.1 Basic measurement principle

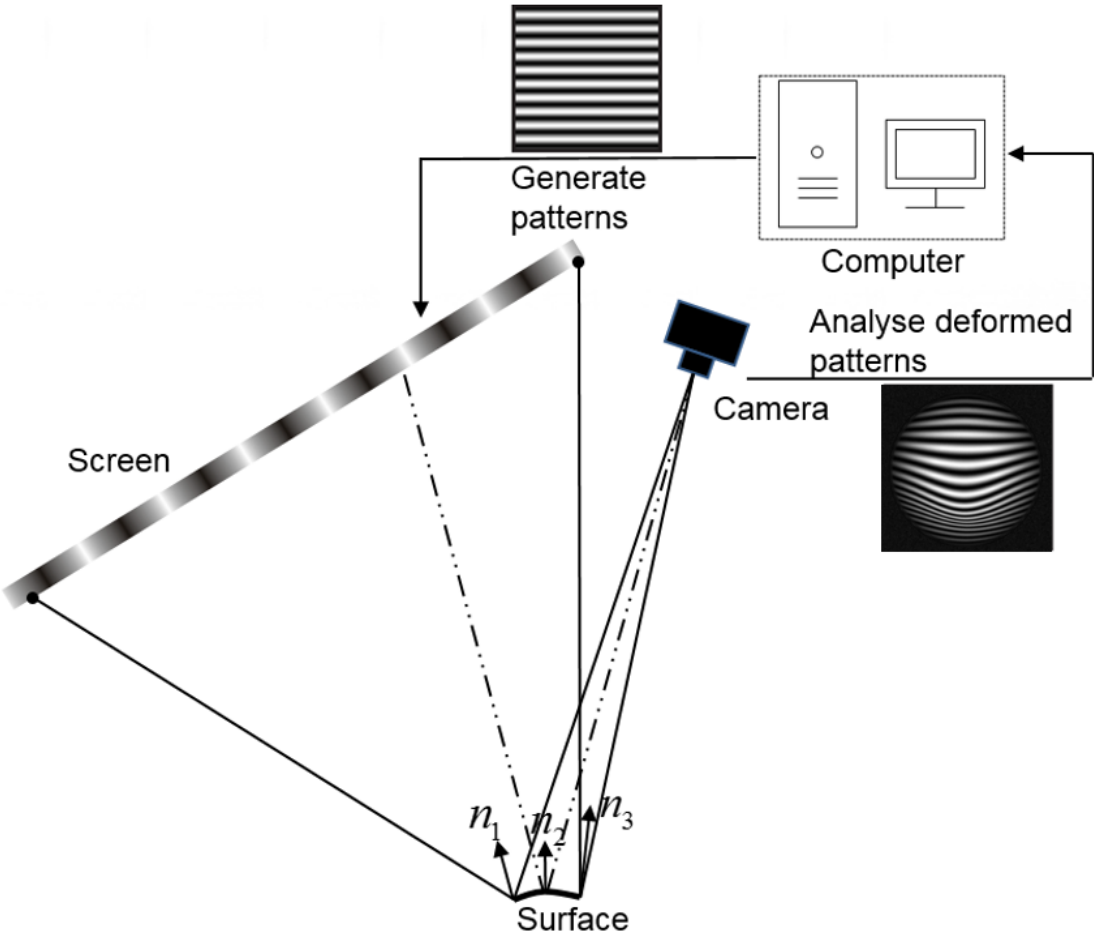


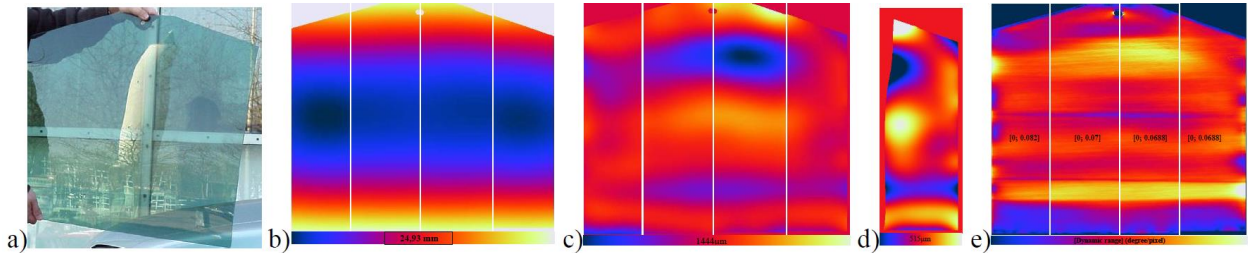
Figure 2.1 Basic measurement principle of deflectometry.

Fig. 2.1 shows the measurement principle of deflectometry. Coded patterns are produced from a computer and are projected onto or displayed on a screen. A camera captures these patterns via the reflection of a specular surface under test. The captured patterns are deformed because of the modulation by the form of the measured surface. By analysing the deformed information, the form

of the measured surface can be obtained. When conducting the measurement, using a camera and a screen is unable to extract the form information successfully (Knauer, Kaminski et al. 2004). Therefore, more constraint is required, such as moving the screen (Petz and Tutsch 2005), adding another camera (Knauer, Kaminski et al. 2004, Ren, Gao et al. 2015) or a virtual screen (Liu, Huang et al. 2017, Zhao, Gao et al. 2018) into the system.

**2.2 Applications of deflectometry**

Deflectometry can be used in many applications. In automotive industry, deflectometry can be applied to measure car window and car finish (Bothe, Li et al. 2004). During the manufacturing process of car window, a wavy surface often exists on the window border. Deflectometry can be used to measure the wavy surface with quantity and to monitor the quality of car window production, as shown in Fig. 2.2 (Bothe, Li et al. 2004). The measured car window is shown in Fig. 2.2(a). The obtained window shape using deflectometry is shown in Fig. 2.2(b). The shape after removing parabolic is given in Fig. 2.2(c). Part measurement with optimized palette range is presented in Fig. 2.2(d). The obtained curvature is shown in Fig. 2.2(d). Orange-peel effect is a long-standing problem in the varnish manufacture of a car. Microstructures remain on car surface when powder lacquer finishes work on the surface. Deflectometry is able to detect this microstructure by quantitatively obtaining the 3D information of car surface, monitoring the varnishing process on line, and optimisation the varnishing parameters. A measurement of a car door using deflectometry is shown in Fig. 2.3 (Bothe, Li et al. 2004). The measured car door is given in Fig. 2.3(a). The obtained form information of the door and the obtained microstructure using deflectometry are represented in Fig. 2.3(b) and Fig. 2.3(c) respectively.



**Figure 2.2 Measurement of a car window using deflectometry. (a) The measured car window; (b) the obtained window shape using deflectometry; (c) shape after removing parabolic; (d) measurement fragment; (e) the acquired curvature. (Bothe, Li et al. 2004)**

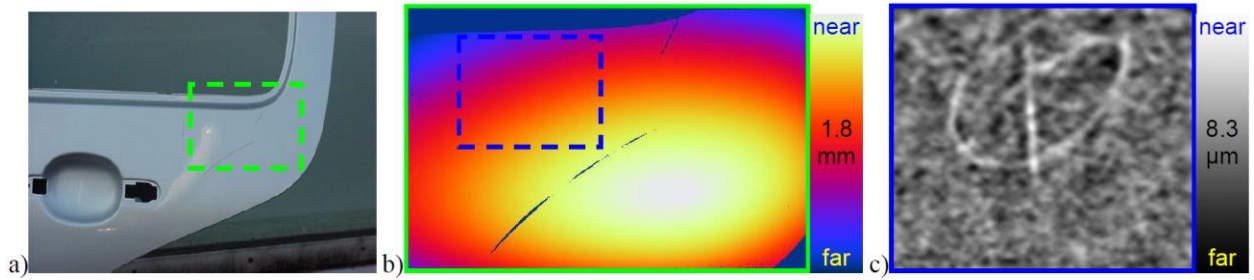


**Figure 2.3** Measurement of a painted car door. (a) The measured car door; (b) the obtained form information of the door; (c) the obtained microstructure. (Bothe, Li et al. 2004)

Plastic eyeglasses have a complicated freeform surface considering the symmetric and torus shapes that guarantee the spectacle wearer to have a good view on objects locating at both near and far distance. Using common non-contact measurement methods is difficult to measure the glasses' surface because of its high dynamic range and the required accuracy. In contrast, deflectometry can have a robust inspection for the eyeglasses. An example is shown in Fig. 2.4 (Bothe, Li et al. 2004). The measured glass is given in Fig. 2.4(a). The captured glass with fringe information is shown in Fig. 2.4(b). The obtained form of the glass by deflectometry is given in Fig. 2.4(c). Deflectometry is capable to measure dynamic specular surface such as fluid water surfaces. Huang et al. (Huang, Ng et al. 2011) proposed a dynamic full-field 3D measuring system. Fig. 2.5 (Huang, Ng et al. 2011) shows the measured water wave variations.

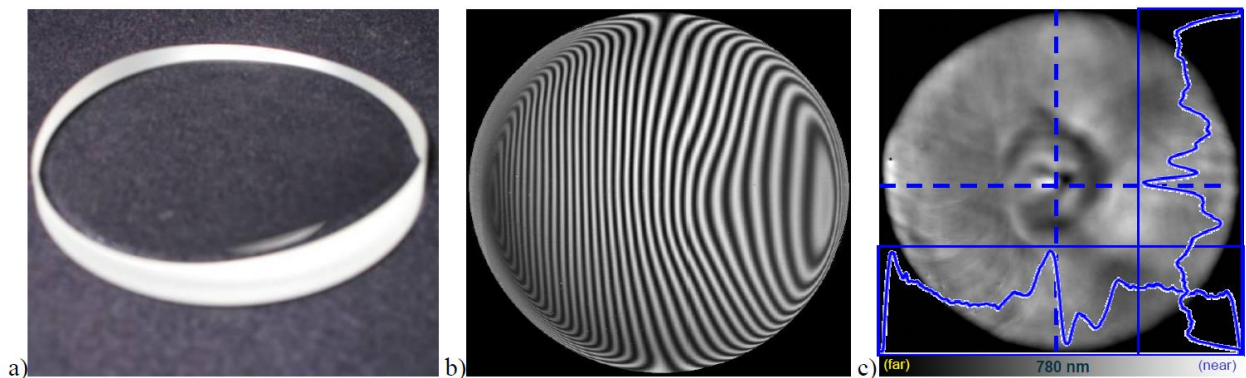


**Figure 2.4** Measurement of an eyeglass. (a) The measured glass; (b) an image of the glass with fringe information; (c) the obtained form of the glass. (Bothe, Li et al. 2004)

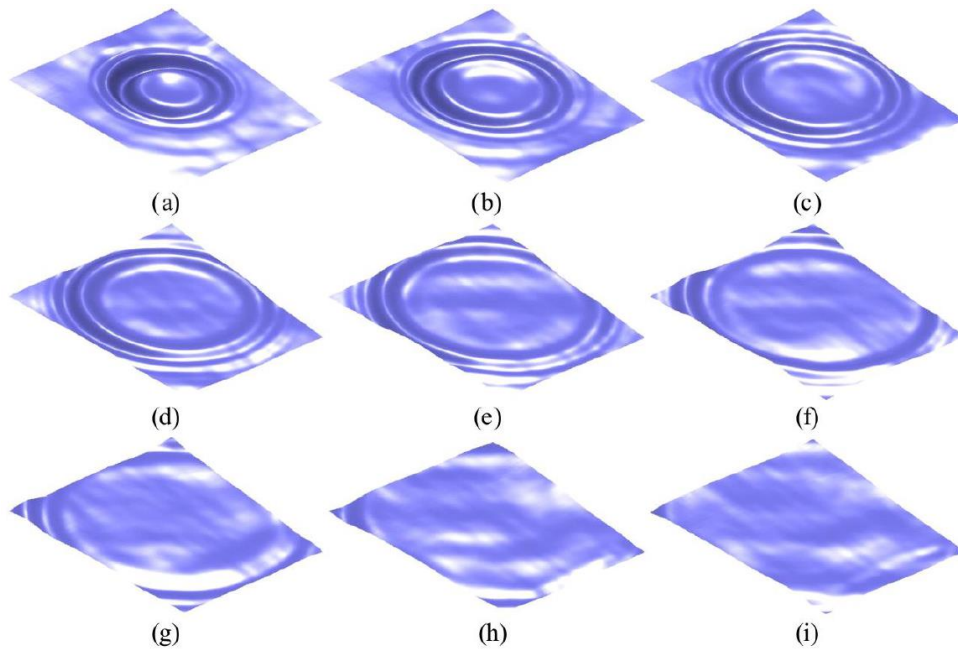


**Figure 2.5** Some reconstructed 3D data of the measured water wave. (a) , (b) , (c) , (d) , (e) , (f) demonstrate the water wave at different moments. ([Huang, Ng et al. 2011](#))

Deflectometry can also be applicable in the measurement of optical element of astronomical telescope. A multi-mirror array with multiple discontinuous specular surfaces (shown in Fig. 2.6(a)) is an essential element in the James Webb Telescope (<https://www.jwst.nasa.gov/>). Zhang et al. ([Liu, Huang et al. 2017](#), [Zhao, Gao et al. 2018](#)) studied a method based on deflectometry to calculate the form of the array, as shown in Fig. 2.6. The measured optical array is shown in Fig. 2.6(a). Measurement result of the array by deflectometry is given in Fig. 2.6(b).

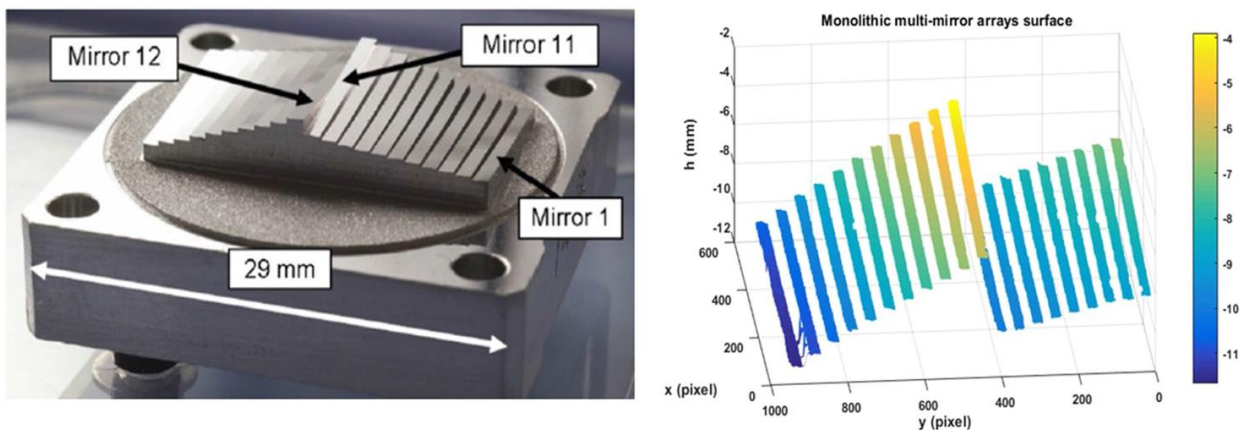


**Figure 2.6** Measure a multi-mirror array based on deflectometry. (a) The measured array; (b) the measurement result. ([Liu, Huang et al. 2017](#))

## 2.3 Typical technologies based on deflectometry

Several typical technologies based on deflectometry have been researched, including active fringe reflection deflectometry ([Zhao, Su et al. 2009](#), [Xiao, Su et al. 2012](#), [Zhang, Ji et al. 2012](#)), software configurable optical test system ([Su, Parks et al. 2010](#), [Su, Khreishi et al. 2013](#), [Huang, Su et al. 2014](#)), microdeflectometry ([Häusler, Richter et al. 2008](#), [Häusler, Vogel et al. 2010](#)), direct phase measuring deflectometry ([Liu, Huang et al. 2017](#), [Zhao, Gao et al. 2018](#)), and stereo deflectometry ([Knauer, Kaminski et al. 2004](#), [Häusler, Faber et al. 2013](#), [Ren, Gao et al. 2015](#)). A description of the principle of these techniques are presented in this section.

### 2.3.1 Active fringe reflection deflectometry

Active fringe reflection deflectometry (AFRD) ([Zhao, Su et al. 2009](#), [Xiao, Su et al. 2012](#), [Zhang, Ji et al. 2012](#)) is a typical method based on deflectometry to measure the specular surface by moving the displaying screen along its axis with a certain distance. The principle of the method is demonstrated in Fig. 2.7. A screen displays coded standard patterns. The patterns are reflected by the measured surface. A CCD (Charge coupled device) camera captures the reflected patterns simultaneously. The optical centre of the CCD camera is defined as  $O$ .  $S$  represents a point on the measured surface. Image of  $S$  on the CCD is represented with  $P$ . Knowing the distance  $\Delta d$  of two parallel positions of the screen, the normal  $n$  of a point  $S$  can be calculated based on incident beam  $O_1O_2$  and reflected beam  $SP$  according to the reflection law. Then the measured surface can be reconstructed based on gradient data.

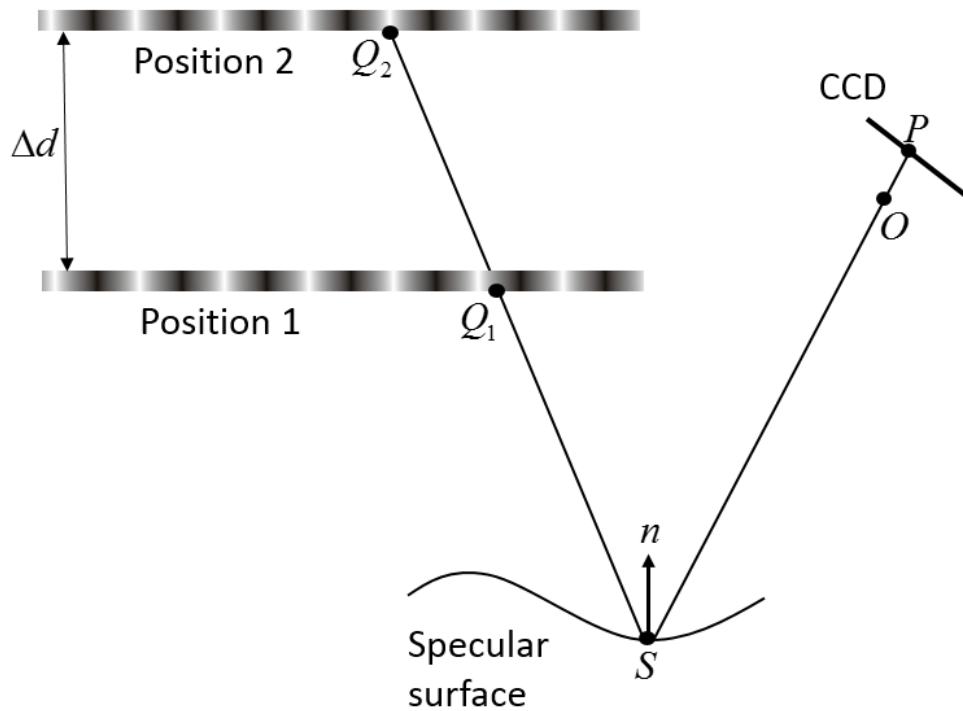
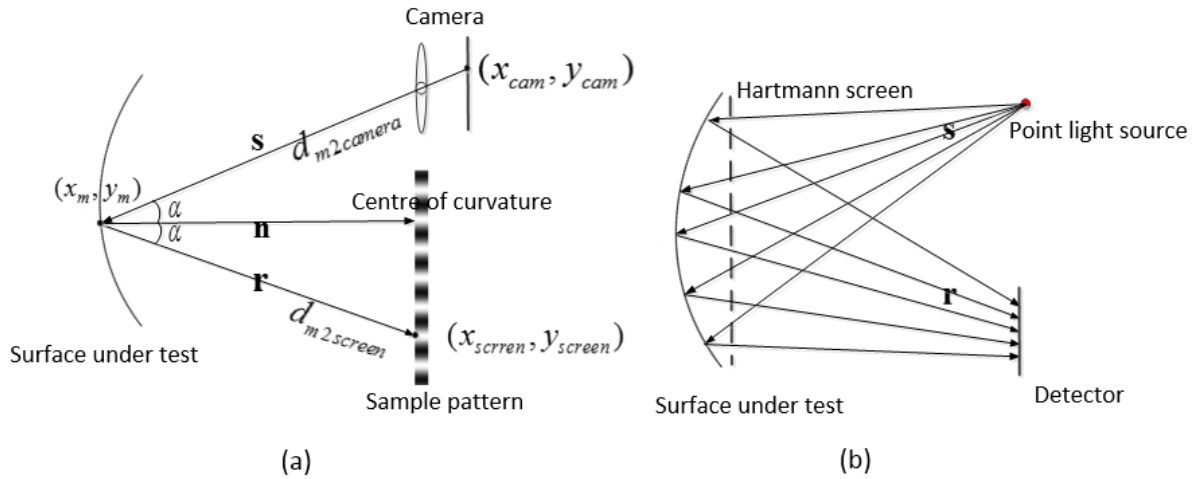


Figure 2.7 Measurement principle of AFRD.

Measurement accuracy of AFRD is limited by the screen's translation accuracy ([Zhao, Su et al. 2009](#), [Xiao, Su et al. 2012](#), [Zhang, Ji et al. 2012](#)). To obtain an accurate incident beam  $Q_1Q_2$ , the shifting distance  $\Delta d$  of the screen have to be accurately acquired. However, in a real measurement, travel distance of the screen and the setup of high precise translation stage are commonly limited by measurement space, which has a serious impact on the accuracy of the measurement. Additionally, screen may move to a position which is out of CCD camera's DOF (depth of focus).

### 2.3.2 Software configurable optical test system (SCOTS)

Software configurable optical test system (SCOTS) ([Su, Parks et al. 2010](#), [Su, Khreishi et al. 2013](#), [Huang, Su et al. 2014](#)) is a technique based on deflectometry developed in University of Arizona. The principle of SCOTS can be seen as the reverse of a Hartmann test. Fig. 2.8 compares the measurement principle of SCOTS and Hartmann test.



**Figure 2.8 Comparison of SCOTS and Hartmann test (a) Principle of SCOTS, (b) principle of Hartmann test. (Su, Parks et al. 2010)**

The principle of a Hartmann test ([Malacara - Doblado and Ghozeil 2007](#), [Malacara 2007](#)) is shown in Fig.2.8(b). Neighbouring the curvature centre of the measured surface, there is a point light source. In front of the surface, a Hartmann screen exists. Hartmann screen is generally a plate with holes. The reflected rays of the light source are caught by a detector during measurement. Gradient of the surface under test is acquired based on transverse aberrations.

Fig.2.8(a) demonstrates the principle of SCOTS. A screen displaying structured patterns is applied to substitute the detector in Hartmann test to light up the measured surface. In addition, a camera capturing distorted structured patterns through the reflection of the surface under test is used to substitute the point light source in Hartmann test. Discrete camera pixels acts as Hartmann screen to take sample of the measured surface. Therefore, holes are not required in SCOTS. Incident ray **S** can be calculated from camera optical centre and camera pixel  $(x_{cam}, y_{cam})$ . Emergent ray **r** can be obtained based on the reflection regions  $(x_m, y_m)$  on the surface and the physical location  $(x_{screen}, y_{screen})$  on the screen. Therefore, the gradients of the measured object can be calculated based on the optical geometric trigonometric relation consisting of target point, the lighting screen's pixel, and camera pixel.

SCOTS can achieve root mean square (RMS) value of surface slope errors better than 100 nano-radian precision when measuring a X-ray mirror ([Su, Wang et al. 2012](#)). However, this technology assumes the change of height is much smaller than the system working distance. Therefore, only

specular surface with large size and small height variance is suitable to be measured with this technique.

### 2.3.3 Microdeflectometry

Another deflectometry-based method is microdeflectometry ([G.Hausler, C.Richter et al. 2008](#)). The measurement principle of microdeflectometry is shown in Fig. 2.9. An electronically controllable light modulator (such as eMagin’s OLED microdisplays) generates fringe patterns. The patterns are enlarged by a tube lens. The light of the enlarged fringe patterns go into a microscope objective through the reflection of a beam splitter. The reflected patterns are focused by a lens and generate an aerial fringe image in front of the measured specimen. A CCD camera focuses on the measured surface and the aerial fringe image.

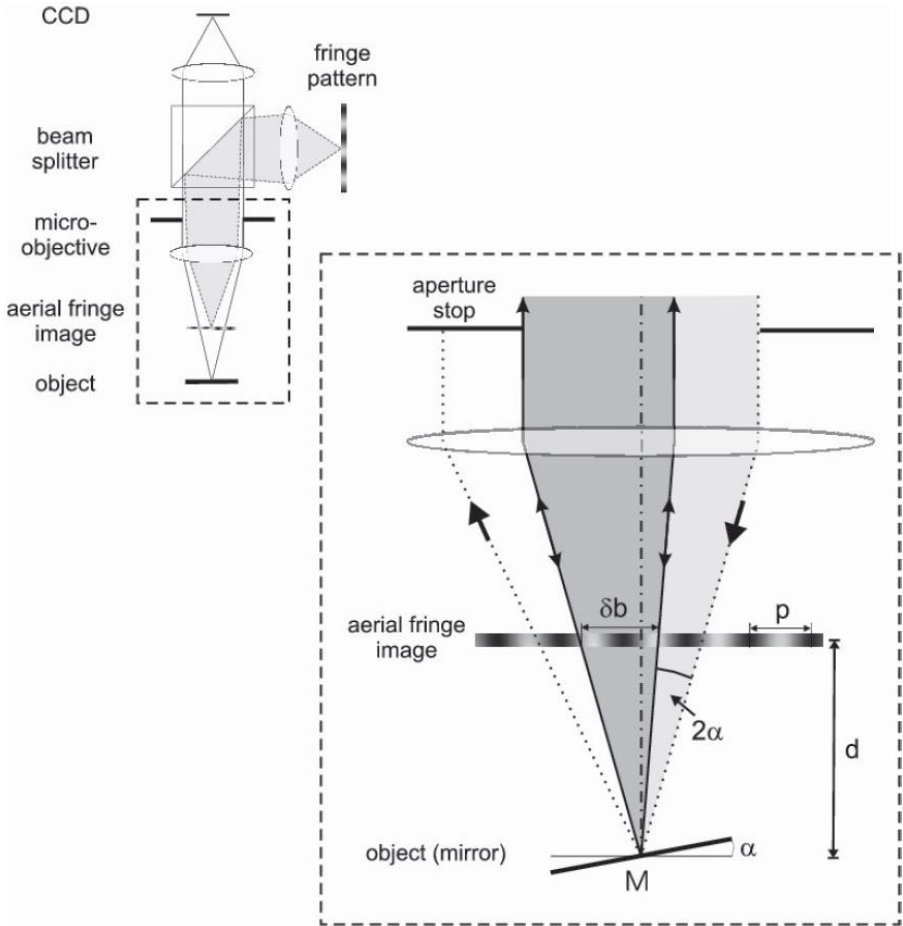


Figure 2.9 Principle of microdeflectometry ([G.Hausler, C.Richter et al. 2008](#)).

The major disadvantage of the method is the small depth of focus of the objectives, which means it requires taking multiple measurements when measuring a large depth sample.

### 2.3.4 Direct phase measuring deflectometry

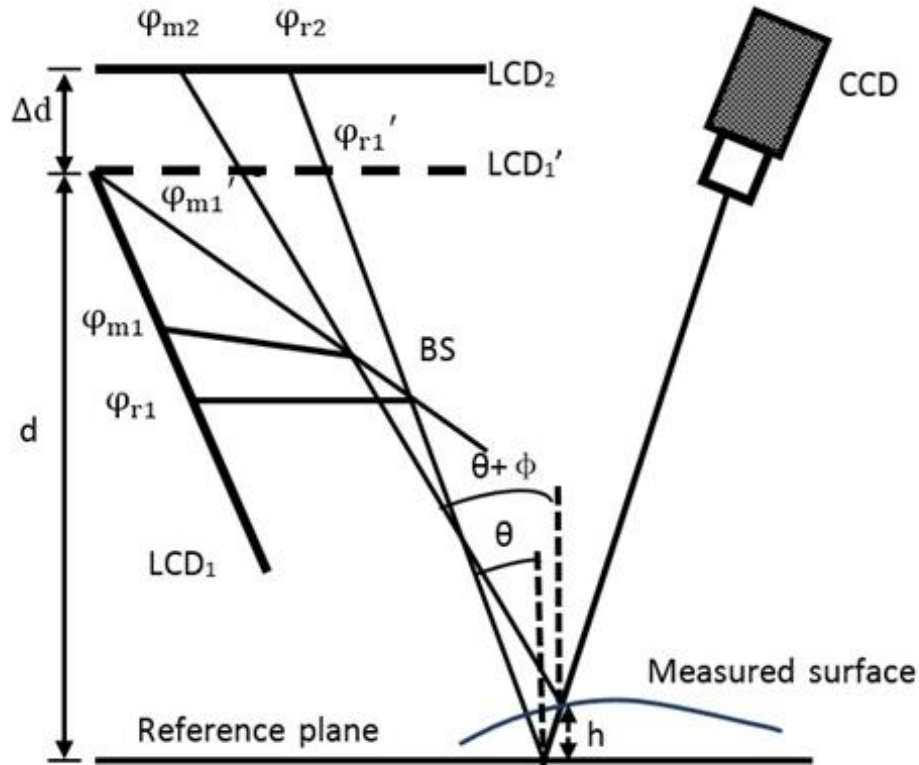


Figure 2.10 Principle of DPMD (Liu, Huang et al. 2017, Zhao, Gao et al. 2018).

Direct phase measuring deflectometry (DPMD) (Liu, Huang et al. 2017, Zhao, Gao et al. 2018) directly calculates the depth information based on phase information instead of integrating the gradients. A CCD camera, a beam splitter (BS) and two LCD (Liquid crystal display) screens made up a DPMD system. Principle of DPMD is demonstrated in Fig. 2.10 (Liu, Huang et al. 2017, Zhao, Gao et al. 2018). A virtual screen  $LCD_1'$  of  $LCD_1$  is adjusted to be parallel to  $LCD_2$  through placing BS at a correct position. Meanwhile, a reference plane is defined to be parallel to  $LCD_1'$  and  $LCD_2$ . A relationship between absolute phase and depth information is established through 3D calibration. Automatic pattern analysis algorithms are implemented to realize 3D reconstruction of the highly reflected and specular surfaces.

Though DPMD can measurement specular object with discontinuous surface, the measurement accuracy can only reach tens of micrometers ([Liu, Huang et al. 2017](#), [Zhao, Gao et al. 2018](#)).

### 2.3.5 Stereo deflectometry

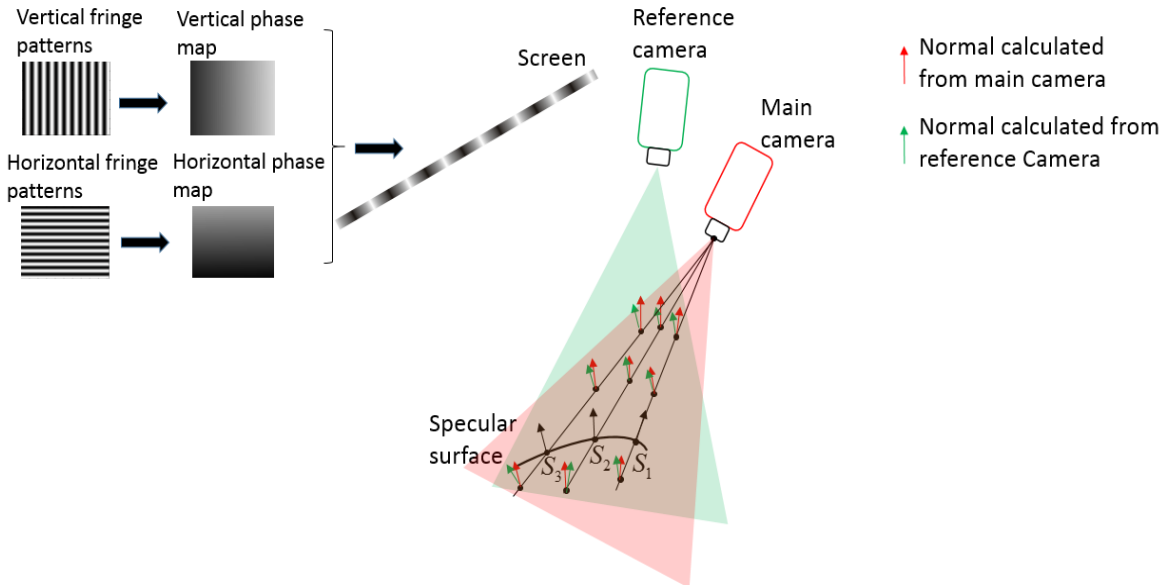


Figure 2.11 The measurement principle of stereo deflectometry.

Stereo deflectometry ([Knauer, Kaminski et al. 2004](#), [Häusler, Faber et al. 2013](#), [Ren, Gao et al. 2015](#)) solves the ambiguity problem of deflectometry by adding another camera into measurement system. Fig. 2.11 demonstrates measurement principle of stereo deflectometry. A stereo deflectometry system is typically composed of a LCD screen displaying coded patterns and two CCD cameras capturing the reflected patterns through the reflection of the measured surface. The screen displays phase-shifting sinusoidal fringe patterns in sequence. The cameras capture the patterns reflected by the measured surface synchronously. Because of the displayed patterns are mutually perpendicular, two orthogonal absolute phase maps in terms of each camera can be acquired by using phase wrapping and unwrapping methods ([Towers, Towers et al. 2005](#), [Zhang, Towers et al. 2006](#)). For an arbitrary space point, its image on the camera's image plane can be calculated based on camera calibration. Its corresponding physical point on the fringe displaying screen can be obtained according to the relation between the absolute phase value and the physical coordinate on the screen. Therefore, the equivalent normal of the space point can be acquired from a triangular geometric relationship composed of the space point, the corresponding point on camera image plane, and the corresponding point on the screen. During the measurement process,

one camera acts as main camera. Space points are searched along camera rays of the main camera. The other camera is a reference camera. The data from this camera are used to define the position of the searched space points. Since normal vectors of the a surface point calculated from main camera and reference camera should be overlapped, initial 3D data with gradient information of the test surface can be calculated by searching points in the space and matching the normal vectors from the cameras. The form of the measured surface is reconstructed by integrating the acquired gradient information ([Huang, Idir et al. 2015](#), [Ren, Gao et al. 2015](#), [Ren, Gao et al. 2016](#)).

Compared with other deflectometry-based techniques, stereo deflectometry can reach relative high accurate measurement accuracy. In addition, the screen of the system is not required to have a movement, therefore the technique has a better advantage in a realistic measurement environment.

#### **2.4 The challenges in stereo deflectometry**

Stereo deflectometry is a method for 3D measurement of freeform specular surfaces ([Knauer, Kaminski et al. 2004](#), [Häusler, Faber et al. 2013](#), [Ren, Gao et al. 2015](#)) . There are still some challenges for this method to achieve a comparable measurement accuracy with interferometers.

Stereo deflectometry consists of two cameras and a screen. It reconstructs the measured surface based on gradient information that is calculated according to the optical relation of systemic components. How to increase stereo deflectometry's calibration accuracy is research hotspots in academic field ([Knauer, Kaminski et al. 2004](#), [Breitbarth, Kühmstedt et al. 2009](#), [Rapp 2012](#), [Häusler, Faber et al. 2013](#), [Ren, Gao et al. 2015](#)). Generally, three aspects ([Knauer, Kaminski et al. 2004](#), [Ren, Gao et al. 2015](#)) of the system are required to be calibrated: screen calibration, camera calibration, and systemic calibration.

Screen calibration is to obtain the relation between the phase value calculated from fringe patterns and the corresponding physical location on the screen. Currently, most deflectometry systems ([Knauer, Kaminski et al. 2004](#), [Breitbarth, Kühmstedt et al. 2009](#), [Rapp 2012](#), [Häusler, Faber et al. 2013](#), [Ren, Gao et al. 2015](#)) apply an electronic screen to display fringe patterns instead of projecting the patterns on a screen, therefore the relation between phase value and physical location can be easily obtained according to fringe density and the size of screen pixel provided by manufactories.

Camera is an elementary component in optical measurement systems such as stereo vision ([Zhang 2000](#), [Wei and Zhao 2016](#)), fringe projection techniques ([Xu, Liu et al. 2012](#), [Zuo, Chen et al. 2013](#), [Xu, Chen et al. 2014](#)) and deflectometry ([Huang, Ng et al. 2011](#), [Ren, Gao et al. 2015](#)). A necessary step in camera-based optical measurement system is camera calibration. Commonly two principle factors affect camera calibration's accuracy. Feature points' position accuracy is one of the factors. The other factor is imaging model accuracy. Current camera calibration processes commonly accept pinhole model. This model assumes the relation between a point in 3D space and its corresponding image in 2D (Two-dimensional) CCD plane is a linear projection. Nevertheless, there is camera distortion in a real imaging. Camera distortion is produced by a number of reasons and can be roughly divided into eccentric distortion, radial distortion, and thin prism distortion. Because of influence of camera distortion, real projection between space and its image is a nonlinear. With the intention of eliminating camera distortion, methods based on mathematical model with parameters have been widely investigated ([Xu, Douet et al. 2013](#)). By means of minimizing reprojection error, Santana-Cedr s et al. ([Santana-Cedr s, Gomez et al. 2017](#)) investigated to estimate a distortion model. Difference of zoom lenses' distortion was studied by Alvarez et al. ([Alvarez, G mez et al. 2012](#)). Infinite high order polynomials are applied to represent camera distortion in traditional camera calibration methods ([Xu, Douet et al. 2013](#)). The first step of traditional methods is to estimate initial camera parameter and distortion parameters. Afterwards, these parameters are optimized through iterative calculation with least squares method.

Camera calibration accuracy is sensitive to the accuracy of initial parameters, because initial values' accuracy affects the constringency of iterative optimization. Real imaging system is complex. Effects such as camera geometry error and imperfect shape of the image sensor all contribute to camera distortion. Nevertheless, a distortion model only containing partial distortion parameters of radial distortion and eccentric distortion is adopted by traditional calibration method ([Zhang 2000](#), [Sanz-Ablanedo, Rodr guez-P rez et al. 2010](#), [Alvarez, G mez et al. 2012](#), [Santana-Cedr s, Gomez et al. 2017](#), [Tang, von Gioi et al. 2017](#)). Because experimental results reflect that a more elaborative model would result in numerical instability rather than increasing calibration accuracy ([Zhang 2000](#)). Consequently, parameter-based distortion mathematical model cannot reflect true distortion and limits traditional calibration methods' accuracy. Researchers

investigated non-parametric calibration approaches to improve distortion compensation accuracy. A method compensating distortion based on binary structured-light is researched by Ryusuke et al. ([Sagawa, Takatsuji et al. 2005](#)). Ryusuke's method cannot obtain camera's internal parameter. A parameter-free calibration method is investigated by Hartley et al. ([Hartley and Kang 2007](#)). Radial distortion is only considered in Hartley's method. A method recovering radial distortion based on multifocal tensors was studied by Thirthala et al. ([Thirthala and Pollefeys 2005](#)). Thirthala's method image centre coincides with distortion centre. Consequently, new method is necessary to be investigated to make camera calibration more flexible and stable.

Traditional calibration methods commonly apply 2D or 3D targets. Control points are designed on the targets. With knowing the physical positions of the points, these points are extracted by algorithms and are applied as a camera calibration input data ([Maoling, Songde et al. 2000](#), [Zhang 2000](#)). 2D targets contains circles, squares, and checkerboards. Because the manufacture of 2D target is much easier than 3D target, 2D target is popularly adopted in practical application ([Zhang 2000](#), [De la Escalera and Armingol 2010](#), [Donné, De Vylder et al. 2016](#)). Owing benefits of massive arbitrary providing of feature points, good position extraction accuracy, and robust to camera defocus, phase target ([Schmalz, Forster et al. 2011](#), [Huang, Zhang et al. 2013](#)) is investigated to replace conventional 2D target. For example, A feature extraction method based on fringe pattern groups is presented by Ma et al. ([Ma, Chen et al. 2014](#)). A calibration target with crossed-fringe pattern is designed by Liu et al. ([Liu and Su 2012](#)). A camera calibration method based on concentric circles grating and wedge grating is studied by Xue et al. ([Xue, Su et al. 2012](#)). Phase target utilizes sinusoidal fringes to produce phase value. The sinusoidal fringes are robust to camera defocus. Because the obtained phase from sinusoidal fringe has little influence on out-of-focus images ([Bell, Xu et al. 2016](#), [Wang, Chen et al. 2016](#)). In order to present the advantage of phase target, a comparison between classic calibration target and phase target have been conducted by Schmalz et al. ([Schmalz, Forster et al. 2011](#)). With the purpose of increasing the feature extraction accuracy of phase target, several techniques have been investigated. A approach based on windowed polynomial fitting is investigated by Huang et al. ([Huang, Zhang et al. 2013](#)). A method is studied by Schmalz et al. ([Schmalz, Forster et al. 2011](#)) to optimize feature location using neighbouring phase. Above-mentioned methods concentrate on the improvement of feature

detection accuracy and target design. How to enhance camera imaging model's accuracy and distortion compensation accuracy using phase target is still out of research.

In applications such as visual measurement ([Zhang 2000](#), [Ren, Gao et al. 2015](#), [Percoco, Guerra et al. 2017](#)), scene surveillance ([Javed, Shafique et al. 2005](#), [Kim, Hwangbo et al. 2008](#)), and mobile robotics ([Lébraly, Deymier et al. 2010](#), [Pagel 2010](#), [Mei, Zhu et al. 2015](#)), single sensor cannot realize system function. System requires a combination of several sensors. The field of view (FOV) of the sensors are occasionally non-overlapped because of cost consideration and function requirement. The fringe-displaying screen is generally used as a phase target to calibrate a stereo deflectometry system. When doing calibration, stereo deflectometry is a non-overlapping cameras system because cameras in stereo deflectometry have common fields on test surface and non-overlapping field on the screen (phase target).

Lately, numerous kinds of methods have been investigated for calibrating a non-overlapping camera system. Calibration equipment are introduced in calibration. A non-overlapping cameras system is calibrated by Lamprecht et al. ([Lamprecht, Rass et al. 2007](#)) based on an online automobile. A calibration method for acquiring non-overlapping camera system's parameters by using HEC is investigated by Guan et al. ([Guan, Shang et al. 2015](#)). A technique based on HEC (hand-eye calibration) ([Zhan and Wang 2012](#)) is studied by Pagel et al. ([Pagel 2010](#)). Nevertheless, the above-mentioned methods rely on calibration equipment's accuracy. Moreover, if cameras in a non-overlapping cameras system cannot be moved, these methods would be invalid. Researchers also investigated calibration method by using a moving target go cover cameras' common FOV. For example, a method is studied by Rahimi et al. ([Rahimi, Dunagan et al. 2004](#)) by recovering routes of a target in cameras. Nevertheless, the accuracy of this method is not enough for optical measurement. Geometric size of calibration target have been tried to be extended to cover FOV of cameras at the same time. A encoded target on a wall is applied by Dong et al. ([Dong, Shao et al. 2016](#)) to calibration a non-overlapping camera system. A calibration method based on 1D target is researched by Liu et al. ([Liu, Zhang et al. 2011](#)). Extension of calibration target size cannot reach infinity. Therefore, for non-overlapping camera system where angle of cameras is 180 degree, these methods are failed. A optical flat is applied in some methods ([Hesch, Mourikis et al. 2008](#), [Kumar, Ilie et al. 2008](#)) to produce an common field of non-overlapping cameras. Since non-

overlapping cameras are required to discover common feature points via reflection of the optical flat, this calibration is not convenient to use in practical application. Furthermore, the extraction accuracy of feature points are seriously affected by DOF of cameras. In a word, the traditional calibration methods for overlapping camera system ([Rahimi, Dunagan et al. 2004](#), [Lamprecht, Rass et al. 2007](#), [Hesch, Mourikis et al. 2008](#), [Kumar, Ilie et al. 2008](#), [Pagel 2010](#), [Liu, Zhang et al. 2011](#), [Zhan and Wang 2012](#), [Guan, Shang et al. 2015](#), [Dong, Shao et al. 2016](#)) are not suitable for stereo deflectometry's calibration.

Systemic calibration is also an important section of stereo deflectometry calibration, which is to obtain the relative geometric positions of the components in the system. There is a challenge in this calibration procedure, as fringes displayed on the fringe-displaying screen do not lie within the measurement cameras' FOV. In order to tackle the problem, a flat mirror with or without markers was applied to complete systemic geometrical calibration. Knauer et al. ([Knauer, Kaminski et al. 2004](#)) used a flat mirror with a set of precise marks to calibrate the systemic geometric parameters of a stereo deflectometry system. Breitbarth et al. ([Breitbarth, Kühmstedt et al. 2009](#)) applied a plane mirror with a pattern of diffusely reflecting segments to complete the calibration procedure. Obviously, the position of the markers of the approaches above must be accurately positioned by photogrammetry in advance. In order to avoid the influence of positioning error, Xiao et al. ([Xiao, Su et al. 2012](#)) introduced a calibration method by applying a markerless optical flat. Conventional deflectometry's calibration ([Knauer, Kaminski et al. 2004](#), [Breitbarth, Kühmstedt et al. 2009](#), [Zhao, Su et al. 2009](#), [Balzer, Hofer et al. 2011](#), [Huang, Ng et al. 2012](#), [Xiao, Su et al. 2012](#), [Huang, Xue et al. 2016](#)) complete camera calibration and systematic calibration separately. Camera calibration is conducted firstly and systemic geometric parameters are calculated based on the camera calibration result. However, objective functions of parameter optimization during the camera calibration and the systemic calibration are different, which results in an inconsistency when combining all systemic optics parameters. In addition, calibration error of camera calibration is propagated to systemic calibration that leads to larger systematic deviations. With the purpose of enhancing calibration accuracy, holistic calibration methods were investigated by using the fringe-displaying screen to calibrate a deflectometry system. All systemic optics parameters can be optimised holistically based on one objective function. Olesch and Faber et al. ([Olesch, Faber et al. 2011](#), [Faber 2012](#), [Ren, Gao et al. 2015](#)) studied an approach to calibrate

parameters of a set of imaging system based on deflectometry. A calibration method is investigated by Ren et al. ([Ren, Gao et al. 2015](#)) for a stereo deflectometry system by applying normal vector of an optical flat as an intermediate variable. The above-mentioned methods compensate deflectometry's distortion based on conventional camera calibration's distortion model ([Zhang 2000, Huang and Asundi 2012](#)). The distortion model cannot match camera's real distortion very accurately. Calibration accuracy is influenced by the accuracy of the distortion model. Distortion error is an important factor causing stereo deflectometry's accuracy to be limited to micron level. In order to achieve higher calibration accuracy, a more effective and accurate distortion elimination method for stereo deflectometry is imperative to be investigated. In addition, the above holistic calibration techniques are based on iterative computation and heavily sensitive to the accuracy of input initial value. Inaccurate initial input causes iterative computation to converge in the wrong position or unable to converge. Image distortion seriously affects the calibration accuracy of the initial value. However, it is lack of research on how to eliminate the calculation error of initial value caused by image distortion for holistic calibration methods.

In addition to deflectometry calibration's inaccuracy, there are plenty of factors affecting a deflectometry system's measurement accuracy. Unsatisfactory performance of the fringe-displaying screen in a deflectometry system seriously influences system's accuracy. Characters of the screen such as colour displaying's inaccuracy, transparent layers' refraction influence, display surface's flatness difference are studied by Petz et al. ([Petz, Fischer et al. 2013](#)). Phase inaccuracy also affects a deflectometry system's measurement accuracy, because deflectometry is a phase-based measurement system. Researchers have investigated techniques to eliminate deflectometry's nonlinear and random phase inaccuracy. By integrating numerous approaches for compensating phase errors in a fringe projection system, a technique is investigated by Wu et al. ([Wu, Yue et al. 2015](#)) to decrease nonlinear error and random error in a deflectometry system. A technique is studied by Yue et al. ([Yue, Wu et al. 2013](#)) for removing nonlinear carrier phase error. During fringe displaying process, continuous sinusoidal fringe patterns are sampled by discrete pixels of fringe-displaying screen. Sampling inaccuracy during this process generates significant phase inaccuracy. Nevertheless, influence of the sampling inaccuracy has not been studied in previous works yet. Investigation of gradient inaccuracy is also important to increase of deflectometry's measurement accuracy, because gradient information is the basic data of the reconstruction result

of deflectometry. Experiments have been done by Zhao et al. (Zhao, Gao et al. 2018) to demonstrate that deflectometry’s measurement accuracy decreases with increasing period of the displayed fringe. Based on diffraction limited, the relation between gradient inaccuracy and phase inaccuracy is studied by Knauer et al. (Knauer, Kaminski et al. 2004). Nevertheless, influence of sampling phase error is not considered in the previous research. In addition to the above error sources, arrangements of components in a deflectometry system also affects system’s measurement accuracy. Impact of systemic parameters of a DPMD system have been studied by Zhao et al. (Zhao, Gao et al. 2018). Nevertheless, there is still a gap in analyses of the effects of systemic parameters of a stereo deflectometry system. Fig. 2.12 summarise the challenges and requirements in order to improve the measurement accuracy of stereo deflectometry.

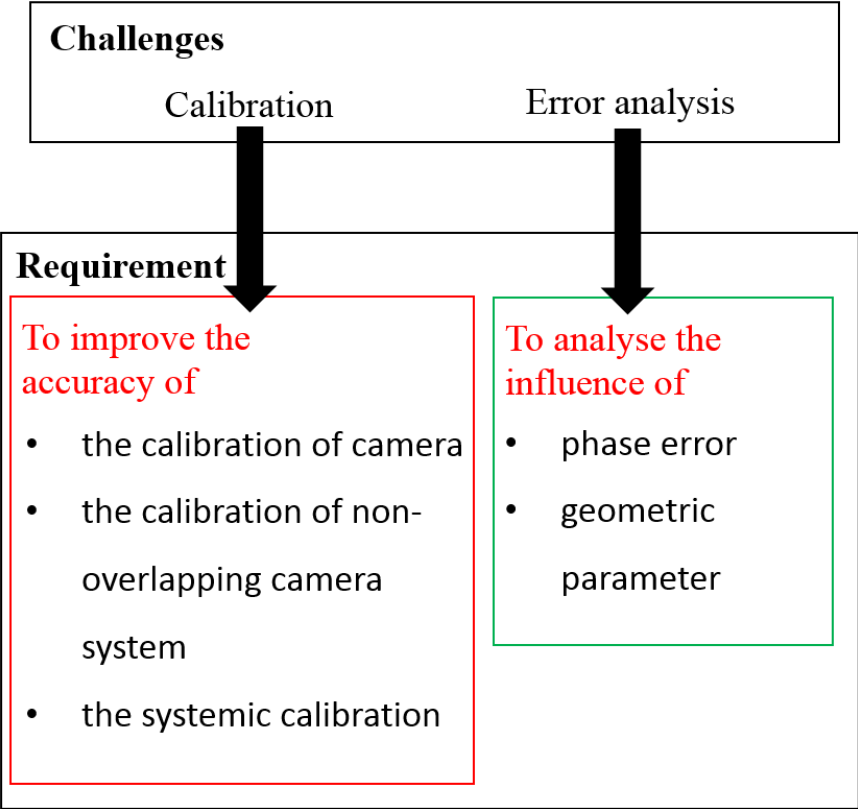


Figure 2.12 An illustrative of the challenges and requirements of stereo deflectometry.

**2.5 Summary**

Basic measurement principle of deflectometry have been reviewed in this chapter. Deflectometry-based technologies, such as active fringe reflection deflectometry, SCOTS, microdeflectometry, DPMD, and stereo deflectometry have been reviewed. Active fringe reflection deflectometry

requires high precise translation stage and its setup is limited by the measurement environment. SCOTS can achieve high accurate measurement results while only specular surface with large size and small height variance is suitable to be measured with this technique. Microdeflectometry has a small depth of focus and requires taking multiple measurements when measuring a large depth sample. DPMD can measurement specular object with discontinuous surface, however measurement accuracy can only reach tens of micrometers. Stereo deflectometry has relative high accurate measurement accuracy compared with other deflectometry-based technique. In addition, the setup of stereo deflectometry is flexible since the screen in the system is not required to be moved. Therefore, stereo deflectometry has an obvious advantage in a realistic measurement of complicated and freeform specular surfaces. Then a detailed literature review of stereo deflectometry is presented. There are many challenges for stereo deflectometry. For example, the accuracy enhancement of calibration which includes camera calibration and systemic calibration and methods to analysis the error source in stereo deflectometry and to reduce the influence of these error sources. This thesis focus on key techniques to solve the challenges to improve deflectometry's measurement accuracy. With the purpose of helping readers to understand the principle and measurement process of stereo deflectometry, the next chapter introduces several important techniques applied in the measurement process of stereo deflectometry, though these techniques are outside of the research scope of this thesis.

### 3. Key techniques in stereo deflectometry

This chapter gives an introduction of some important techniques in stereo deflectometry. Section 3.1 introduces the coding technique of the displayed fringe patterns. Section 3.2 presents phase unwrapping algorithms that obtain absolute phase maps from fringe patterns. The normal calculation algorithm of deflectometry is described in section 3.3. In section 3.4, reconstruction algorithms of stereo deflectometry that obtain the 3D form of the measured surface from the normal vectors is presented. A brief summary of this chapter is given in section 3.5.

#### 3.1 Phase shifting algorithm

Though different coding patterns techniques, such as phase marker ([Cui, Liao et al. 2012](#)), binary pattern ([Butel, Smith et al. 2014](#)) have been developed for deflectometry, these methods have a problem caused by the limitation of depth of field because cameras in the deflectometry system based on these techniques cannot focus on the measured object and the screen at the same time. To overcome this problem, sinusoidal fringe pattern ([Knauer, Kaminski et al. 2004](#), [Häusler, Faber et al. 2013](#), [Ren, Gao et al. 2015](#)) is applied in deflectometry because defocus has little influence on the sinusoidal fringe pattern when the cameras focuses on the measured object. Phase shifting algorithm uses the intensity of the captured patterns through shifting the phase of sinusoidal fringes patterns to obtain the phase value ([Rathjen 1995](#)). This algorithm is popularly used in PSI ([Capanni, Pezzati et al. 1997](#)) and fringe projection technique ([Zhang, Towers et al. 2006](#), [Zuo, Huang et al. 2016](#)). Sinusoidal fringes are also used in deflectometry as the sample patterns and utilizes phase shifting algorithm to obtain the phase value. During the measuring process of stereo deflectometry, series of phase shifting fringe patterns are displayed on the screen and are captured by the cameras simultaneously. The generation of the patterns is the first step of the measurement and has a significant influence on the measurement accuracy. The phase shifting fringe patterns applied in stereo deflectometry are coded according to the following equation:

$$I_n(x, y) = I'(x, y) + I''(x, y) \cos(\phi(x, y) + 2\pi n / m) \quad (3.1)$$

where  $I'(x, y)$  is the average intensity,  $I''(x, y)$  is the intensity modulation,  $\phi(x, y)$  is the phase to be solved.  $n = 0, 1 \dots m$ , and  $m$  is the number of phase shift. In order to effectively restrain the

nonlinear error of the system, eight-step phase-shifting technique is applied and therefore  $m$  equals 8. Figure 3.1 shows a group of eight-step phase-shifting fringe patterns. In order to determine the physical coordinate on the screen of a point based on phase value, another group of vertical fringe patterns are generated, as shown in Fig. 3.2. In addition, the displayed fringe patterns are required to change the frequency to obtain an absolute phase maps, therefore there are 48 fringe patterns in all during a measurement process. The influence of the fringe density on the measurement accuracy is discussed in Chapter 7.

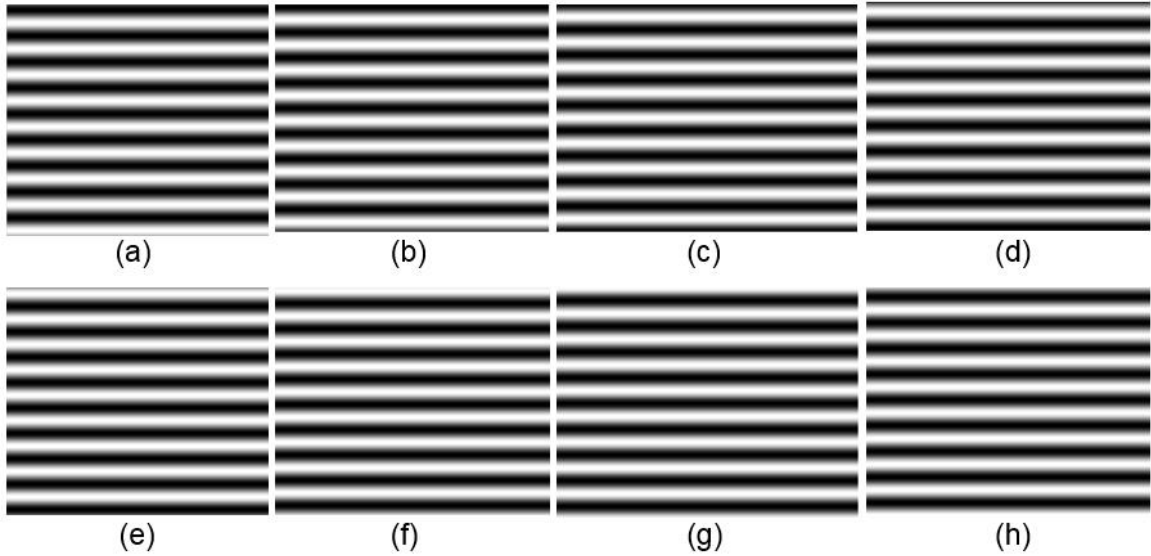


**Figure 3.1 Horizontal fringe patterns.** (a)  $n = 0$ ; (b)  $n = 1$ ; (c)  $n = 2$ ; (d)  $n = 3$ ; (e)  $n = 4$ ; (f)  $n = 5$ ; (g)  $n = 6$ ; (h)  $n = 7$ .

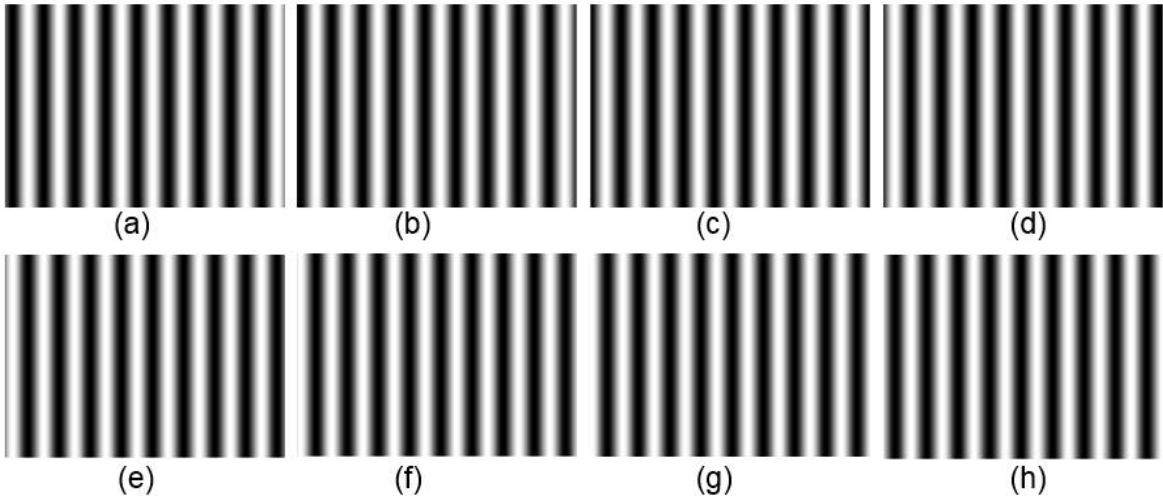


**Figure 3.2 Vertical fringe patterns.** (a)  $n = 0$ ; (b)  $n = 1$ ; (c)  $n = 2$ ; (d)  $n = 3$ ; (e)  $n = 4$ ; (f)  $n = 5$ ; (g)  $n = 6$ ; (h)  $n = 7$ .

The measured phase of  $m$ -step phase shifting algorithm can be retrieved as

$$\varphi(x, y) = \arctan \left( \frac{\sum_{n=0}^{m-1} I_n^* I_n}{\sum_{n=0}^{m-1} I_n' I_n} \right) \quad (3.2)$$

where  $I_n' = \cos(2\pi n / m)$ ,  $I_n^* = -\sin(2\pi n / m)$  and  $\varphi(x, y)$  is the calculated wrapped phase whose range is limited from  $-\pi$  to  $\pi$  because of arctan operation. Fig. 3.3 is the obtained horizontal wrapped phase map from the fringe patterns shown in Fig. 3.1. Fig. 3.4 is the obtained vertical wrapped phase map from the fringe patterns shown in Fig. 3.2.

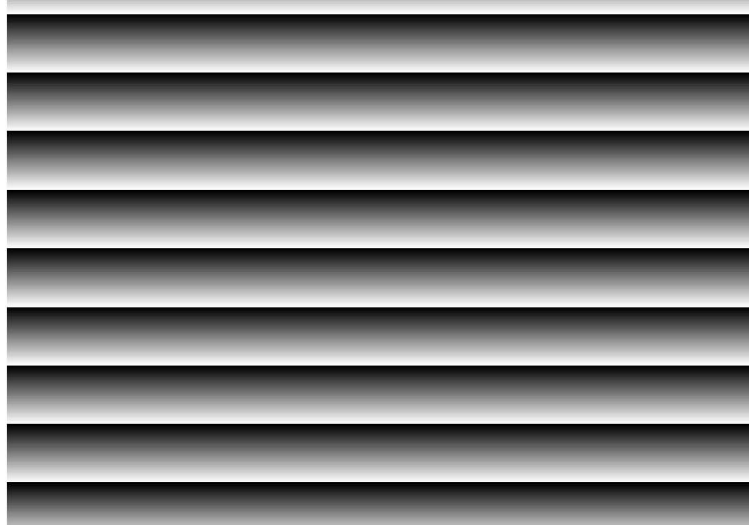


**Figure 3.3** Wrapped phase map of horizontal fringe patterns.



**Figure 3.4 Wrapped phase map of vertical fringe patterns.**

### **3.2 Phase unwrapping algorithm**

In order to get absolute phase, the  $2\pi$  radians phase jumps in wrapped phase must be removed through a process known as phase unwrapping ([Ghiglia and Pritt 1998](#), [Rastogi and Hack 2014](#)). At present, there are mainly two kinds of phase unwrapping algorithms: temporal phase unwrapping algorithm and spatial phase unwrapping algorithm. Spatial phase unwrapping algorithm ([Chan, Bryanston-Cross et al. 1995](#)) adds or subtracts multiples of  $2\pi$  into wrapped phase by comparing neighbouring pixels' wrapped phases. Though spatial phase unwrapping algorithm is easy to implement, it is sensitive to phase errors because if there is a point having obvious error in a wrapped phase map, every point unwrapped based on the point will be incorrect ([Rastogi and Hack 2014](#)).

Stereo deflectometry requires an absolute phase map to determine the physical location of a point on the screen, however spatial phase unwrapping algorithm can only obtain relative phase map for the reason that it lacks of absolute origin point and only establishes the relation between neighbouring points. Therefore, spatial phase unwrapping algorithm is not suitable for stereo deflectometry.

Temporal phase unwrapping algorithm ([Saldner and Huntley 1997](#)) retrieves absolute phase by applying series of patterns with frequency difference. This algorithm unwraps phase of each pixel independently. The phase of each pixel has no relation with its neighbouring pixels. Coding phase unwrapping algorithm ([Wissmann, Schmitt et al. 2011](#), [Zheng and Da 2012](#)) and heterodyne phase unwrapping algorithm ([Reich, Ritter et al. 1997](#)) are the most commonly used phase unwrapping algorithms. Coding phase unwrapping algorithm applies grey fringes with different frequency. The fringe order of each pixel can be obtained based on encoding method. However, coding phase unwrapping algorithm requires a large number of fringe patterns and affects the measurement speed. In addition, it is easy to produce a serious phase error at the fringe boundary. Among these temporal phase unwrapping algorithms, one popularly utilised in a stereo deflectometry system is three-frequency heterodyne temporary phase unwrapping (TFHTPU) ([Petz and Tutsch 2005](#), [Towers, Towers et al. 2005](#)). Because TFHTPU tries to apply fringe patterns as few as possible to obtain accurate absolute phase information.

Heterodyne phase unwrapping algorithm uses series of phase-shifting sinusoidal fringe patterns with frequency difference to obtain absolute unwrapped phase map. The principle of heterodyne phase unwrapping algorithm can be expressed in Fig. 3.5 and Eq. (3.3).

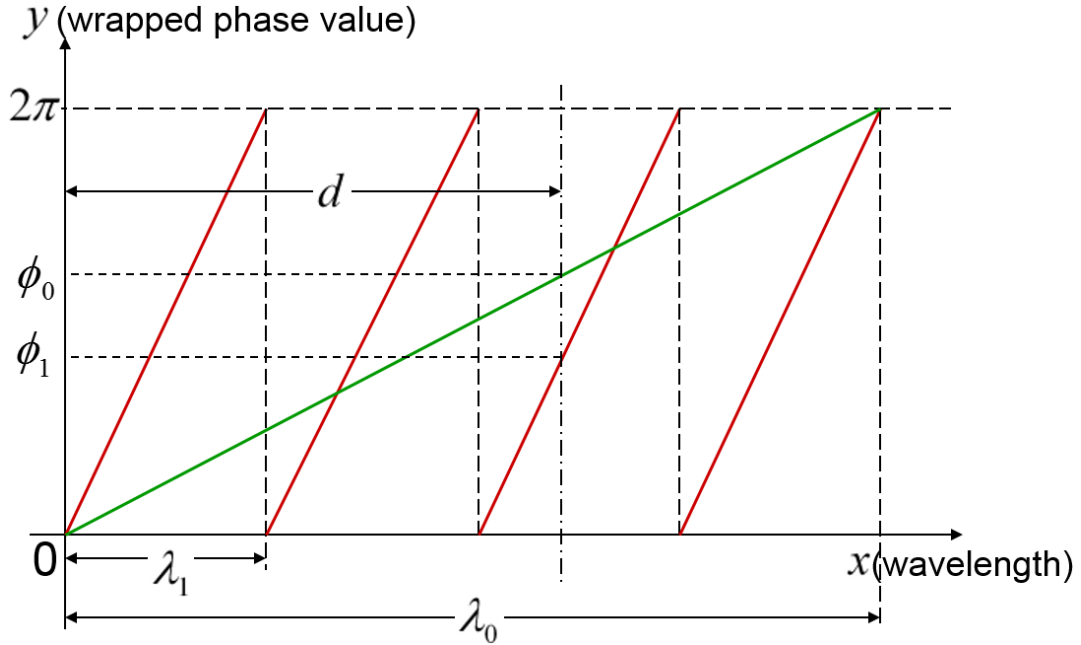


Figure 3.5 The principle of heterodyne phase unwrapping algorithm.

$$d = \left(m + \frac{\phi}{2\pi}\right)\lambda \quad (3.3)$$

where  $d$  is the physical distance between a calculated point and the zero phase point.  $\phi$  is the phase value of the calculated point.  $\lambda$  is the effective wavelength of a wrapped phase map.  $m$  is the fringe order. Assuming there are two sinusoidal fringe patterns. One has a fringe number of  $N_0$ . The other has a fringe number of  $N_1$ . The wrapped phases calculated from the two fringe patterns are illustrated as the red line and the green line in Fig. 3.5. Defining measurement range is  $L$ , the effective wavelengths of the two groups of sinusoidal fringe patterns are defined as  $\lambda_0 = L/N_0$  and  $\lambda_1 = L/N_1$  respectively.  $\phi_0$  and  $\phi_1$  are the wrapped phase value of the two fringe patterns when the physical distance from zero phase point is  $d$ . A new fringe pattern can be acquired by conducting subtraction between the two fringe patterns. The phase wrapped phase

value of the new fringe pattern is  $\phi_{01}$  and its effective wavelength is defined as  $\lambda_{01} = \lambda_0 \lambda_1 / (\lambda_1 - \lambda_0)$ . The following equation can be obtained based on Eq. (3.3):

$$d = (m_0 + \frac{\phi_0}{2\pi})\lambda_0 = (m_1 + \frac{\phi_1}{2\pi})\lambda_1 = (m_{01} + \frac{\phi_{01}}{2\pi})\lambda_{01} \quad (3.4)$$

when  $\lambda_{01} \geq d$ ,  $m_{01}$  equals 0. Then Eq. (3.4) can be simplified to the following equation:

$$(m_0 + \frac{\phi_0}{2\pi})\lambda_0 = \frac{\phi_{01}}{2\pi} \lambda_{01} \quad (3.5)$$

Based on Eq. (3.5), the fringe number can be calculated according to the following equation:

$$m_0 = \text{Int}[\frac{\lambda_{01}}{\lambda_0} \frac{\phi_{01}}{2\pi} - \phi_0] \quad (3.6)$$

An unwrapped phase map can be obtained based on the fringe number. According to Eq. (3.6), during the heterodyne temporary phase unwrapping process, phase noise is amplified by the difference of fringe frequency. Over amplified noise will seriously affect phase accuracy. In order to reasonably control the degree of phase noise magnification, Towers et al. proposed TFHTPU. TFHTPU uses three groups of different fringes frequency. The fringe number of the applied fringe patterns in TFHTPU algorithm ([Towers, Towers et al. 2005](#)) can be expressed as

$$\begin{cases} N_{f0} = N_{f0} \\ N_{f1} = N_{f0} - 1 \\ N_{f2} = N_{f0} - \sqrt{N_{f0}} \end{cases} \quad (3.7)$$

According to the definition of Eq. 3.3, the difference of fringe frequency is kept within the range of allowable changes.

Because stereo deflectometry requires two cross-directional coordinates to locate a point on the screen, a horizontal absolute phase map and a vertical absolute phase map are needed to be obtained. Fig. 3.6 displays the horizontal unwrapped phases calculated from three groups of phase-

shifting fringe patterns with frequency defference.  $N_{f_0}$  is the maximum fringe number of the chosen patterns.  $N_{f_0}$  equals to 9 in Fig. 3.6. Other two fringe numbers  $N_{f_1}$  and  $N_{f_2}$  are 8 and 6 respectively. Fig. 3.7 displays the corresponding vertical unwrapped phases. The horizontal absolute phase map and vertical absolute phase map calculated from the wrapped phase maps in Fig. 3.6 and Fig. 3.7 based on TFHTPU are shown in Fig. 3.8 and Fig. 3.9 respectively.

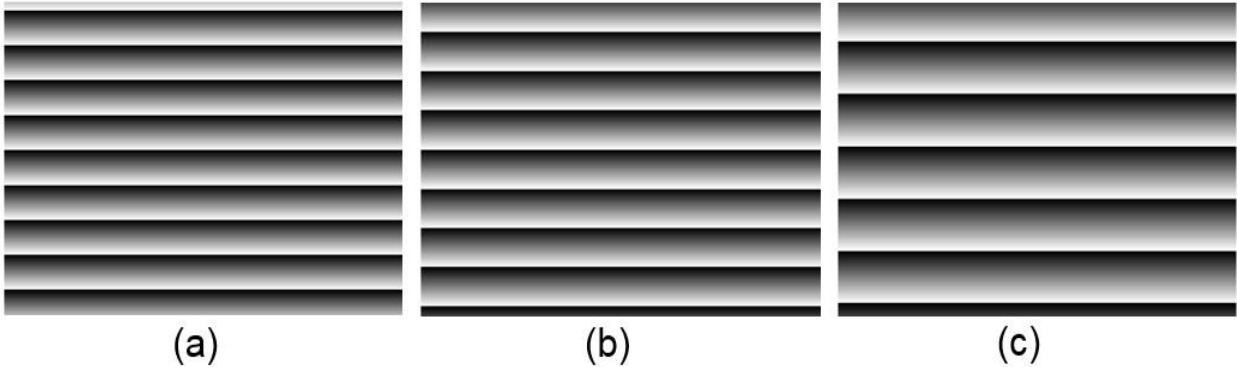


**Figure 3.6 Horizontal wrapped phase maps. (a) Fringe number is 9; (b) fringe number is 8; (c) fringe number is 6.**

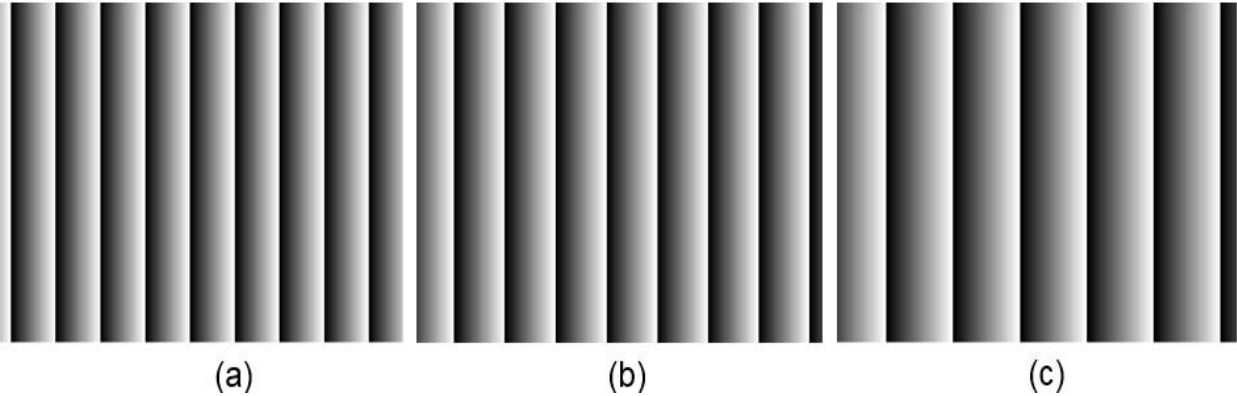


**Figure 3.7 Vertical wrapped phase maps. (a) Fringe number is 9; (b) fringe number is 8; (c) fringe number is 6.**

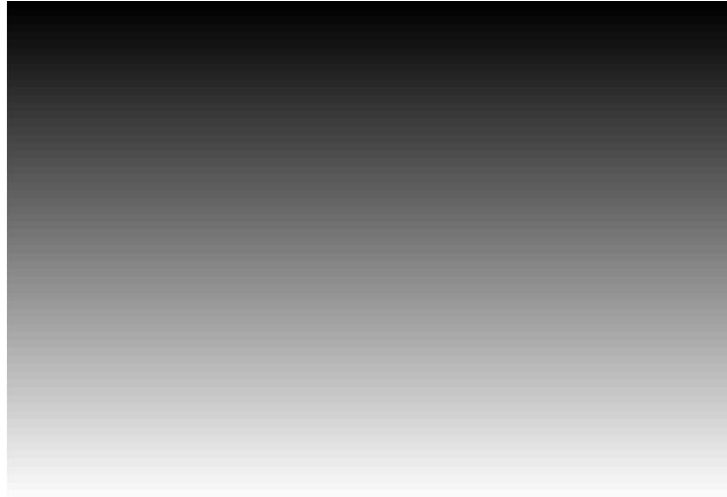


**Figure 3.8 Horizontal absolute unwrapped phase map.**

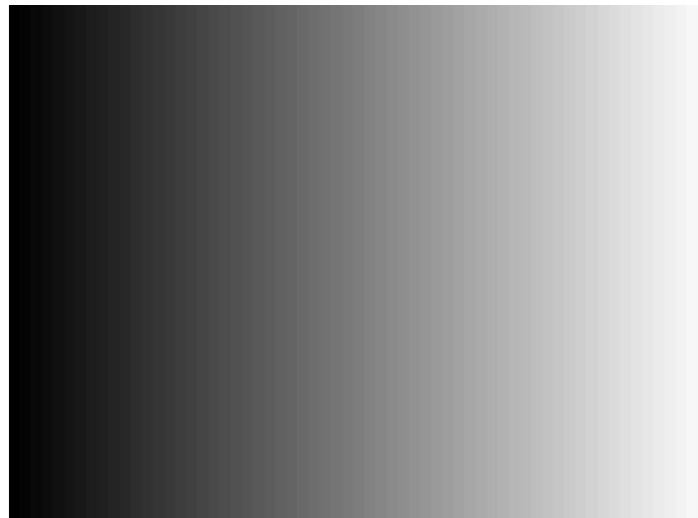


**Figure 3.9 Vertical absolute unwrapped phase map.**

### 3.3 Gradient calculation algorithm

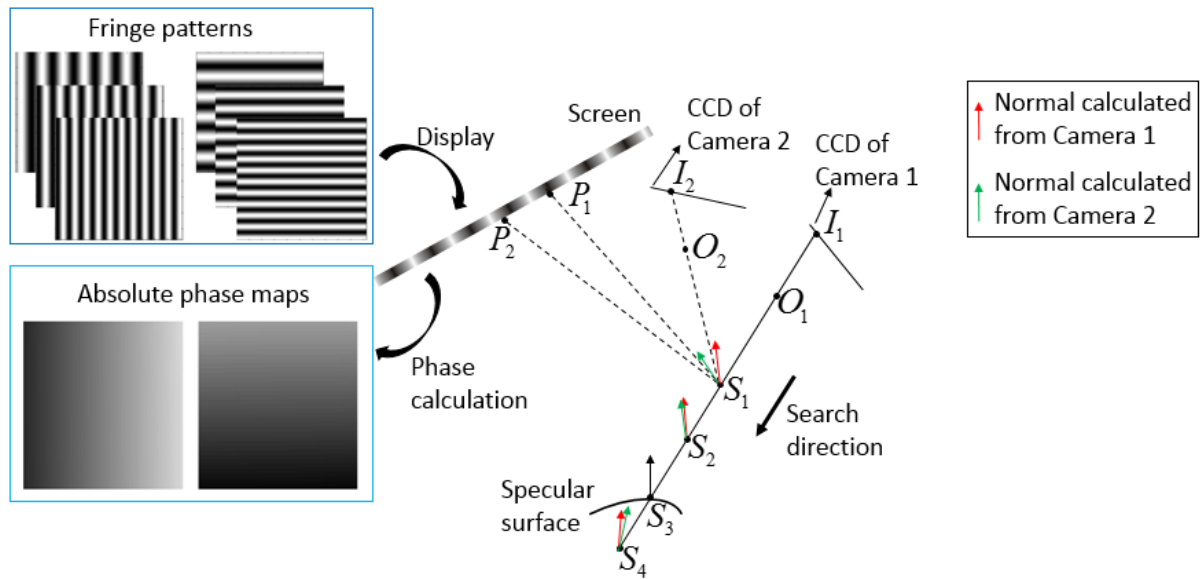
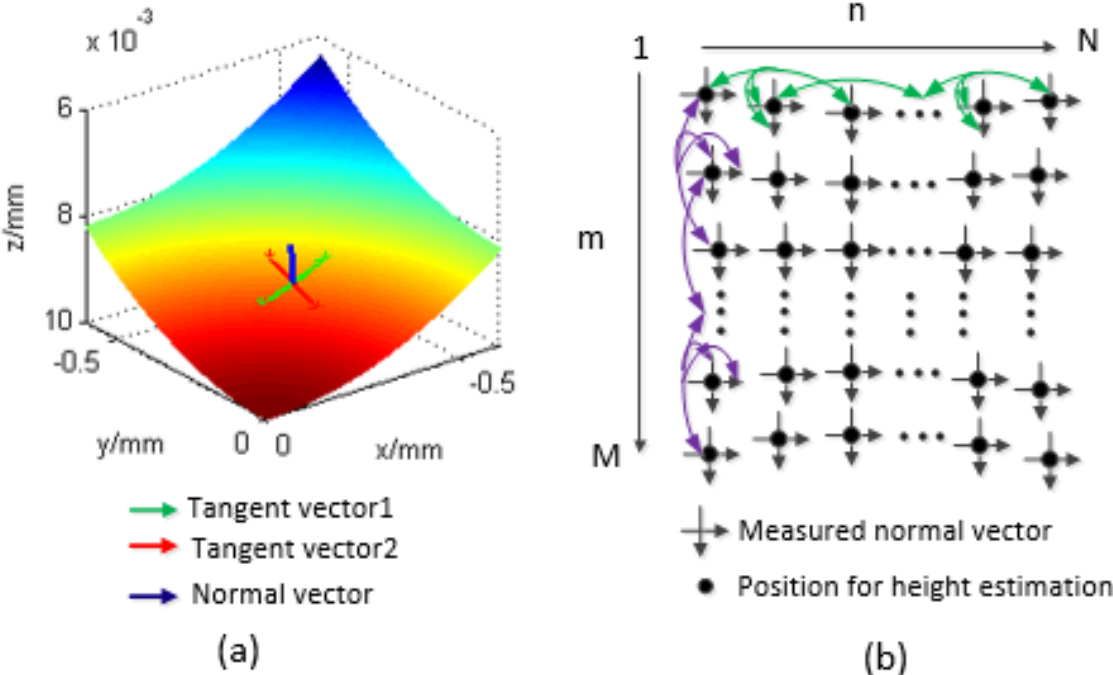


Figure 3.10 The measurement principle of stereo deflectometry.

Fig. 3.10 demonstrates the gradient calculation method of stereo deflectometry. Camera 1 works as main camera.  $O_1$  is the optical centre of main camera. Camera 2 is reference camera. The optical centre of the reference camera is  $O_2$ . A fringe-displaying screen displays two groups phase-shifting fringe patterns (Werling 2011). One group of patterns is horizontal. The other group of patterns is vertical. The patterns are reflected by the surface under test and are captured by the main camera and the reference camera simultaneously. A horizontal absolute phase map and a vertical absolute phase map can be acquired through the calculation of phase-shifting and phase unwrapping (Towers, Towers et al. 2005, Zhang, Towers et al. 2006).  $S_1$  is an arbitrary space point. After camera calibration and system calibration (Xu, Gao et al. 2018), its image's position  $I_1$  in the imaging plane of the main camera can be obtained. Based on the horizontal phase value and vertical phase value of  $I_1$ , its corresponding physical location  $P_1$  on the fringe-displaying screen can be obtained. Space point  $S_1$ , image point  $I_1$ , and point  $P_1$  on the fringe-displaying screen made up an optical triangular. Based on the optical triangular, a normal vector of  $S_1$  is obtained. In an optical triangular consisting of  $S_1$ , image point in the reference camera ( $I_2$ ) and screen point  $P_2$ , another normal vector of  $S_1$  is obtained by using similar method. Only when  $S_1$  is a surface, normal vectors obtained based on the main camera and the reference camera are

matched. By searching space points and comparing normal vectors calculated based on the main camera and the reference camera, initial 3D coordinates and normal information of the surface under test are acquired. Final data are optimised based on the reconstruction algorithms described in the following section.

**3.4 Reconstruction algorithms based on gradient integration**



**Figure 3.11 Principle of gradient integration method.**

The principle of gradient integration method is based on the Taylor’s theorem ([Graves 1927](#)) which describes a regular surface at a point can be approximated by a higher order polynomial. According to the deduction of Taylor’s theorem, for a continuous and smooth surface, normal vector of a point is perpendicular to a vector consisting of the point and the adjacent point, as shown in Fig. 3.11(a).

Since the measured objects of stereo deflectometry are continuous and smooth specular surfaces, an explicit function  $z = f(x, y)$  can be used to express the surface under test. A given point has at least two times differentiable in the explicit function. A measured surface can be approximately described by a polynomial in two variables based on Taylor’s theorem ([Zorich 2002](#)), as shown in the following equations:

$$\begin{aligned}
f(x + \Delta x, y + \Delta y) &= f(x, y) + \frac{\partial f(x, y)}{\partial x} \Delta x + \frac{\partial f(x, y)}{\partial y} \Delta y \\
&+ \frac{1}{2} \left( \frac{\partial^2 f(x, y)}{\partial x^2} \Delta x^2 + 2 \frac{\partial^2 f(x, y)}{\partial x \partial y} \Delta x \Delta y + \frac{\partial^2 f(x, y)}{\partial y^2} \Delta y^2 \right) \\
&+ R_2(\Delta x, \Delta y)
\end{aligned} \tag{3.8}$$

where  $\Delta x$  and  $\Delta y$  are minor increments along  $x$  and  $y$  direction respectively. Approximation error  $R_2(\Delta x, \Delta y)$  goes to zero faster than  $\Delta x^2 + \Delta y^2$ . Eq. (3.8) can be rewritten in Eq. (3.9) by using vector  $\nabla f(x, y)$  and matrix of second derivatives  $D^2 f(x, y)$ :

$$f(x + \Delta x, y + \Delta y) \approx f(x, y) + \nabla f(x, y) \cdot \begin{pmatrix} \Delta x \\ \Delta y \end{pmatrix} + \frac{1}{2} \left( \begin{pmatrix} \Delta x \\ \Delta y \end{pmatrix}^T \cdot D^2 f(x, y) \cdot \begin{pmatrix} \Delta x \\ \Delta y \end{pmatrix} \right) \tag{3.9}$$

Defining world coordinate of a given point on the surface under test is  $(x_{m,n}, y_{m,n}, z_{m,n})$ . First and second differentiable of a tiny surface near the point is expressed as  $\nabla f(x, y)$  and  $D^2 f(x, y)$  respectively. Assuming a point  $(x_m, y_n, z_{m,n})$  on the measured surface. Neighbouring points  $(x_{m,n+1}, y_{m,n+1}, z_{m,n+1})$  and  $(x_{m,n-1}, y_{m,n-1}, z_{m,n-1})$  are positioned at either side of the point. Based on Eq. (3.9), the relation between the neighbouring points can be expressed with Eq. (3.10) and Eq. (3.11).

$$z_{m,n+1} - z_{m,n} \approx \nabla f(x, y) \cdot \begin{pmatrix} \Delta x_1 \\ \Delta y_1 \end{pmatrix} + \frac{1}{2} \left( \begin{pmatrix} \Delta x_1 \\ \Delta y_1 \end{pmatrix}^T \cdot D^2 f(x, y) \cdot \begin{pmatrix} \Delta x_1 \\ \Delta y_1 \end{pmatrix} \right) \tag{3.10}$$

$$z_{m,n-1} - z_{m,n} \approx \nabla f(x, y) \cdot \begin{pmatrix} \Delta x_2 \\ \Delta y_2 \end{pmatrix} + \frac{1}{2} \left( \begin{pmatrix} \Delta x_2 \\ \Delta y_2 \end{pmatrix}^T \cdot D^2 f(x, y) \cdot \begin{pmatrix} \Delta x_2 \\ \Delta y_2 \end{pmatrix} \right) \tag{3.11}$$

where  $\Delta x_1$  and  $\Delta x_2$  are tiny increment of  $x_{m,n}$  along  $x_{m,n+1}$  and  $x_{m,n-1}$  respectively.  $\Delta y_1$  and  $\Delta y_2$  are tiny increment of  $y_{m,n}$  along  $y_{m,n+1}$  and  $y_{m,n-1}$  respectively. Subtracting Eq. (3.11) from Eq. (3.10), the relation between the neighbouring points can be depicted as

$$\begin{aligned}
z_{m,n+1} - z_{m,n-1} &\approx \nabla f(x, y) \cdot \begin{pmatrix} \Delta x_1 - \Delta x_2 \\ \Delta y_1 - \Delta y_2 \end{pmatrix} \\
&+ \frac{1}{2} \left( \begin{pmatrix} \Delta x_1 - \Delta x_2 \\ \Delta y_1 - \Delta y_2 \end{pmatrix}^T \cdot D^2 f(x, y) \cdot \begin{pmatrix} \Delta x_1 + \Delta x_2 \\ \Delta y_1 + \Delta y_2 \end{pmatrix} \right)
\end{aligned} \tag{3.12}$$

It is noticeable that second-order element of Eq. (3.12) is smaller comparing with those of Eq. (3.10) and Eq. (3.11). Eq. (3.12) is more accurate than Eq. (3.10) and Eq. (3.11) when height relation of a surface is roughly expressed only by first differentiable. Moreover, second-order element of Eq. (3.12) goes to zero faster than first element. Therefore, the following equation can be used to replace Eq. (3.12):

$$\begin{aligned}
z_{m,n+1} - z_{m,n-1} &\approx f_x(\Delta x_1 - \Delta x_2) + f_y(\Delta y_1 - \Delta y_2) \\
&= f_x(x_{m,n+1} - x_{m,n-1}) + f_y(y_{m,n+1} - y_{m,n-1})
\end{aligned} \tag{3.13}$$

where  $f_x$  and  $f_y$  are first derivative of the measured surface along x and y direction respectively.

Neighbouring points locating at either side of  $(x_m, y_n, z_{m,n})$  along y direction can be deduced based on the same principle:

$$z_{m+1,n} - z_{m-1,n} \approx f_x(x_{m+1,n} - x_{m-1,n}) + f_y(y_{m+1,n} - y_{m-1,n}) \tag{3.14}$$

Normal vector of a point on a regular surface can be represented as  $(f_x, f_y, -1)$  when the surface can be expressed with an explicit function. Therefore, normal vector of a surface point is perpendicular to the vectors connecting points at either side according to Eq. (3.13) and (3.14), as shown in Fig. 3.11(a). Therefore, relation between two neighbouring separated points in height can be obtained based on the following equation:

$$\begin{cases}
(z_{i,j+2} - z_{i,j}) = (x_{i,j+2} - x_{i,j}) \times f_{x(i,j+1)} + (y_{i,j+2} - y_{i,j}) \times f_{y(i,j+1)}, \\
\quad i = 1 \cdots M, j = 1 \cdots N - 2; \\
(z_{i+2,j} - z_{i,j}) = (x_{i+2,j} - x_{i,j}) \times f_{x(i+1,j)} + (y_{i+2,j} - y_{i,j}) \times f_{y(i+1,j)}, \\
\quad j = 1 \cdots M - 2, j = 1 \cdots N.
\end{cases} \tag{3.15}$$



### **3.5 Summary**

Some key algorithms applied in stereo deflectometry are briefly introduced in this chapter, including phase shifting algorithm, phase unwrapping algorithm, normal calculation algorithm and reconstruction algorithm. Though these techniques are outer of research scope of this thesis, they are significant in measurement process of stereo deflectometry and are helpful for the readers to understand stereo deflectometry. The mains works of this thesis are described in detail in the following chapters.

## 4. Improvement of camera calibration accuracy

Camera calibration is the first step of the calibration of a stereo deflectometry system. Accuracy of camera calibration is seriously affected by camera distortion. Because of imprecise distortion compensation model of traditional calibration method, the calibration accuracy of stereo deflectometry cannot be satisfied. A novel camera calibration technique based on phase target is investigated in this chapter. Massive pixels of camera and the corresponding physical points on the phase target are applied to calculate initial imaging parameters of the camera. Afterwards, a distortion compensation technique based on an iterative algorithm is imposed. With the purpose of improving feature extraction of phase target, fitting and interpolation approach is studied to smooth phase maps. The camera calibration technique described in this chapter does not depend on traditional calibration methods' distortion model. Consequently, it is more effective and accurate than traditional calibration methods especially for camera with big distortion. Experimental results indicate that calibration accuracy is improved over 100% by using the investigated calibration technique. The work in this chapter generated one published journal paper ([Xu, Gao et al. 2017](#)).

### 4.1 Principle of camera calibration method

#### 4.1.1 Phase target

The calibration approach studied in this chapter is based on a phase target shown in Fig. 4.1. The phase target consisted of a group of vertical sinusoidal fringe patterns shown in Fig. 4.1(a) and a group of horizontal sinusoidal fringe patterns shown in Fig. 4.1(b). After applying the phase shifted method and the phase unwrapping method ([Towers, Towers et al. 2005](#), [Zhang, Towers et al. 2006](#)), a vertical absolute phase map shown in Fig. 4.1(c) and a horizontal absolute phase map shown in Fig. 4.1(d) are obtained. The obtained phase maps are continuous. In practical operation, a LCD screen is often used to display the fringe patterns. Denoting the size of LCD pixel pitch is  $p$  and the number of LCD pixels per fringe period is  $n_p$ . Based on the vertical phase value  $\varphi_x$  and horizontal phase value  $\varphi_y$ , the corresponding physical location  $(x_w, y_w)$  on phase target of points on camera imaging plane can be located based on Eqs. (4.1) and (4.2).

$$x_w = (n_p \cdot p / 2\pi) \cdot \varphi_x \quad (4.1)$$

$$y_w = (n_p \cdot p / 2\pi) \cdot \varphi_y \quad (4.2)$$

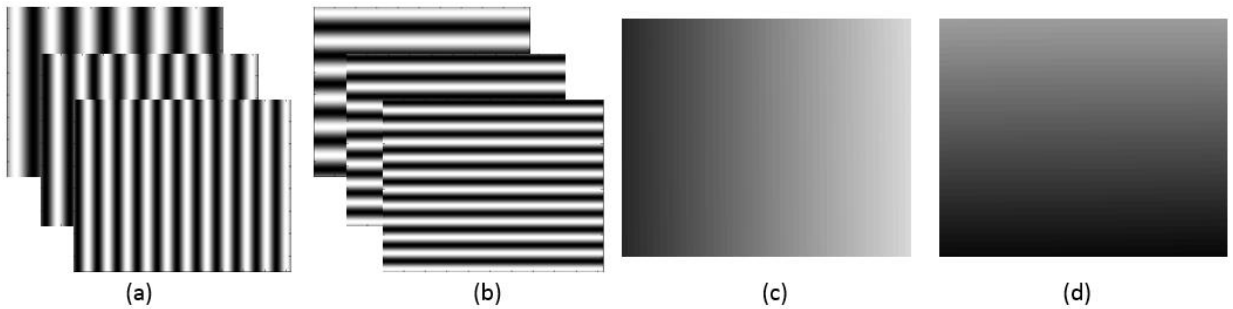


Figure 4.1 The phase target used in camera calibration process. (a) One of vertical sinusoidal fringe patterns; (b) one of horizontal sinusoidal fringe patterns; (c) vertical absolute phase; (d) horizontal absolute phase.

#### 4.1.2 Calibration with iterative distortion compensation algorithm

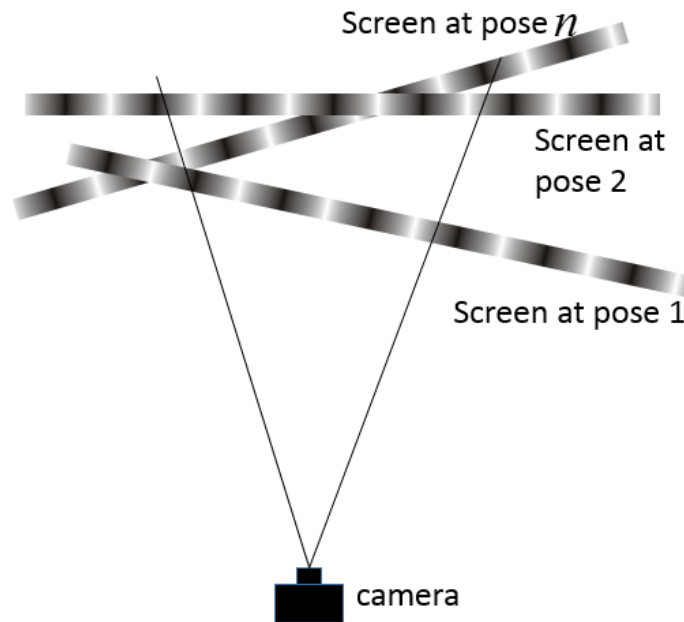


Figure 4.2 Phase target is placed at arbitrary poses.

During calibration process, phase target is placed at several arbitrary positions, as shown in Fig. 4.2. Defining the number of phase target's position as  $n$ . With the purpose of improving calibration speed, sampled points uniformly distributed on camera imaging plane instead of full camera pixels are chose to conduct calibration calculation. Imaging parameters are acquired based on Eq. (4.3).

$$s \begin{bmatrix} u \\ v \\ 1 \end{bmatrix} = A \cdot [R \quad t] \cdot \begin{bmatrix} x_w \\ y_w \\ z_w \\ 1 \end{bmatrix} = H \begin{bmatrix} x_w \\ y_w \\ 1 \end{bmatrix} \text{ with } A = \begin{bmatrix} \alpha & 0 & u_0 \\ 0 & \beta & v_0 \\ 0 & 0 & 1 \end{bmatrix} \quad (4.3)$$

where  $H$  is a linear projection between space point and its image in camera imaging plane. World coordinate of a space point is defined as  $(x_w, y_w)$ . Coordinate of its image point is expressed with  $(u, v)$ . Image process is studied based on pinhole model. Transformation from world coordinate system to camera coordinate system is defined as  $[R \quad t]$ .  $R$  is the rotation matrix of the transformation.  $t$  is the translation matrix of the transformation. Internal parameter of a camera is expressed with  $A$ . Scale factors of the camera along  $u$  and  $v$  direction is expressed with  $\alpha$  and  $\beta$ . Principal point of the camera is defined as  $(u_0, v_0)$ .  $i^{th}$  column of  $R$  and  $H$  is denoted as  $r_i$  and  $h_i$  respectively. With the knowledge that  $r_1$  and  $r_2$  are orthonormal, two constraints on the internal parameter can be obtained:

$$\begin{cases} h_1^T A^{-T} A^{-1} h_2 = 0 \\ h_1^T A^{-T} A^{-1} h_1 = h_2^T A^{-T} A^{-1} h_2 \end{cases} \quad (4.4)$$

$A$  can be calculated based on at least three calibration poses because two constraints can be provided from a calibration pose. External parameter  $\{R_i, t_i \mid i = 1..n\}$  can be acquired based on Eq. (4.5):

$$\begin{cases} r_1 = \lambda A^{-1} h_1 \\ r_2 = \lambda A^{-1} h_2 \\ r_3 = r_1 \times r_2 \\ t = \lambda A^{-1} h_3 \end{cases} \text{ with } \lambda = 1 / \|A^{-1} h_1\| \quad (4.5)$$

Eq. (4.6) reflects calculation error of the applied imaging model.

$$\Delta m = \hat{m}(A, R, t, M) - m \quad (4.6)$$

Physical location of space in terms of world coordinate is denoted as  $M$ .  $\Delta m$  represent the deviation between real coordinate  $m$  and reprojection coordinate  $\hat{m}$  obtained based on  $A, R, t$

and  $M$ .  $\Delta m$  should be a constant for the same camera pixel, since distortion is constant for a fixed focus camera. A corrected coordinate  $m^*$  is calculated based on Eq. (4.7):

$$m^* = m + \overline{\Delta m} \quad (4.7)$$

where  $\overline{\Delta m}$  is the average deviation of different calibration. An iterative loop is applied to optimize initial values of  $A$ ,  $\{R_i, t_i | i = 1..n\}$ , and  $\overline{\Delta m}$  by minimizing the following function with Levenberg-Marquardt Algorithm:

$$\sum_{i=1}^n \sum_{j=1}^k \|m^*(m, \overline{\Delta m}) - \hat{m}(A, R_i, t_i, M_{ij})\|^2 \quad (4.8)$$

Fig. 4.3 summarizes the calibration process of the studied camera calibration.

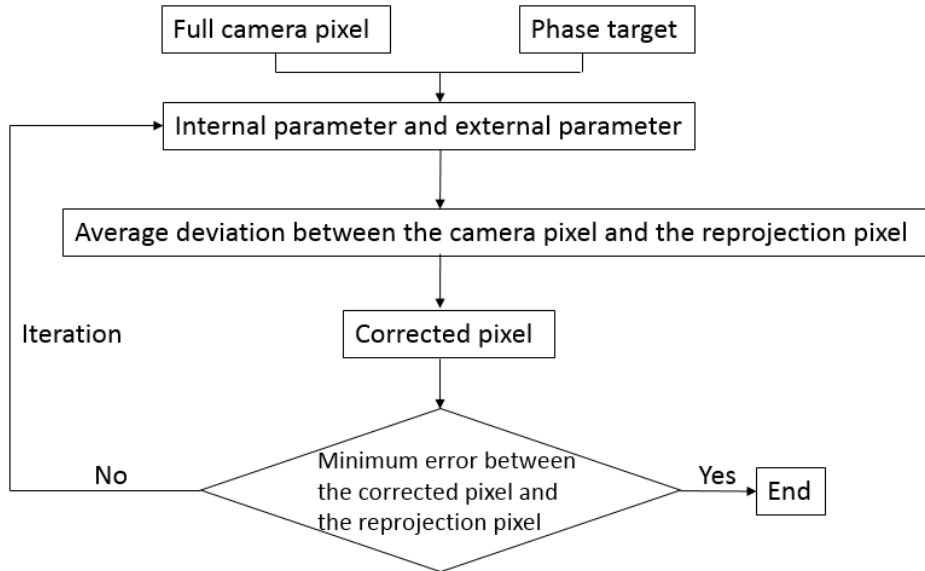
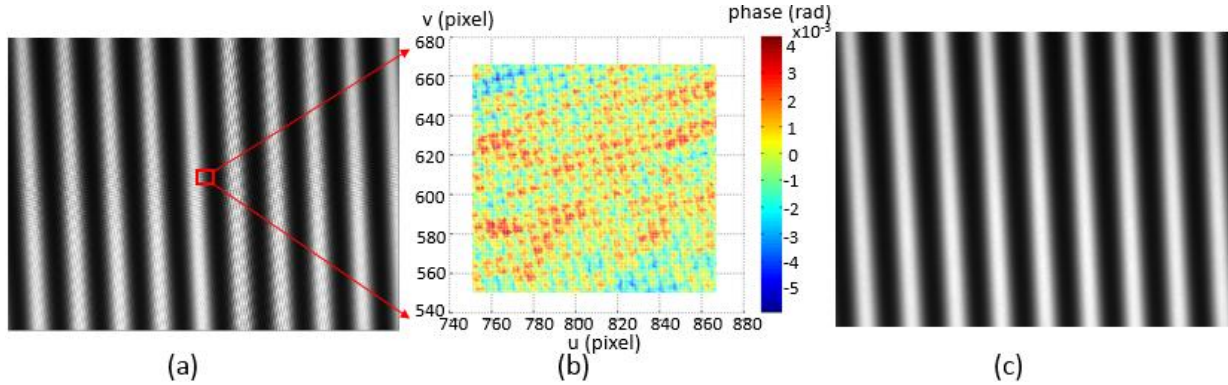


Figure 4.3 Summary the calibration process.

### 4.1.3 Compensation algorithm for phase target error

Interference between LCD pixels (phase target) and CCD camera pixels results in Moiré fringe. In addition, LCD pixels are captured by CCD camera when LCD screen locates at camera's focus. Moiré fringe and the captured LCD pixels lead to a fringe distortion on the fringe pattern captured by CCD camera. Fig. 4.4(a) shows the fringe distortion. Fig. 4.4(b) shows the phase error of the fringe distortion. Gaussian filter (De la Escalera and Armingol 2010) was used to remove the fringe distortion and optimize fringe quality. Nevertheless, one problem of Gaussian filter is how to

choose filter's size. A defocus technique is tested in Fig. 4.4(c). Phase target is placed at camera's defocus position when doing calibration. A pattern captured by CCD camera shown in 4.4(c) indicates that fringe distortion has been removed.



**Figure 4.4 Fringe distortion on a captured fringe pattern. (a) A pattern captured by CCD camera when phase target is placed at camera's focus position; (b) phase error; (c) a pattern captured by CCD camera when phase target is placed at camera's defocus position.**

A technique is investigated to optimize the quality of phase target based on fitting and interpolation method. The principle of the technique is demonstrated in Fig. 4.5. Phase point located at  $(u_p, v_p)$  is expressed with green dot. Because absolute phase map is continuous, a tiny surface of the phase point can be expressed with the tangent plane of the phase point. A plane is fitted based on the phase values of its neighboring  $L/2$  pixel points. Least square algorithm is the basic technique of the fitting process. The fitted plane is shown in Fig. 4.5 with a French grey colour. By applying cubic polynomial interpolation algorithm on the fitted plane, an interpolated phase point as the red dot shown in Fig. 4.5 is obtained. Defining  $L$  as fitting widow of the fitting method. Theoretically, phase error would be more effective to be removed by applying big  $L$ . Nevertheless, because absolute phase map is a curve surface, big  $L$  will bring fitting error. Eqs. (4.9) and (4.10) are used to demonstrate that absolute phase map is a curve surface. Eqs. (4.9) and (4.10) is derived based on Eqs (4.1)–(4.3) and presents the relationship between vertical absolute phase map  $\varphi_x$ , horizontal absolute phase map  $\varphi_y$ , and its location  $(u, v)$ .

$$\varphi_x = \frac{2\pi \cdot (h_{11} \cdot u + h_{12} \cdot v + h_{13})}{n_p \cdot p \cdot (h_{31} \cdot u + h_{32} \cdot v + h_{33})} \quad (4.9)$$

$$\varphi_y = \frac{2\pi \cdot (h_{21} \cdot u + h_{22} \cdot v + h_{23})}{n_p \cdot p \cdot (h_{31} \cdot u + h_{32} \cdot v + h_{33})} \quad (4.10)$$

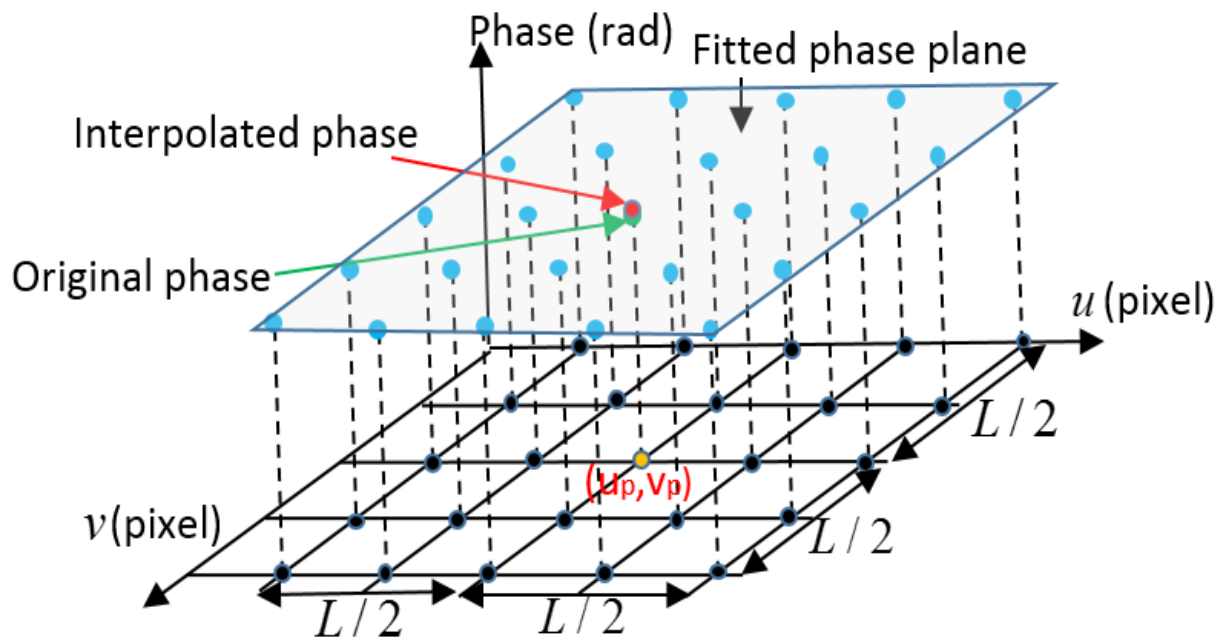


Figure 4.5 Principle of fitting and interpolation method.

A simulation experiment is made to investigate the optimized  $L$ . With the purpose of simulating real measurement noise, phase error are randomly added into the experiment. Fig. 4.6 shows that reprojection error decreases dramatically along with increasing  $L$  from 0 to 5 pixels. At the same time, rotation matrix error and translation matrix error also have the same trend with reprojection error. Reprojection error decreases from 0.0016 pixels to 0.000172 pixels with  $L$  increasing from 5 pixels to 60 pixels. In contrast, this is an opposite for rotation matrix error and translation matrix error. Therefore, in order to decreasing phase error and at the same time not over optimize original phase value,  $L$  should be set to 5 pixels.

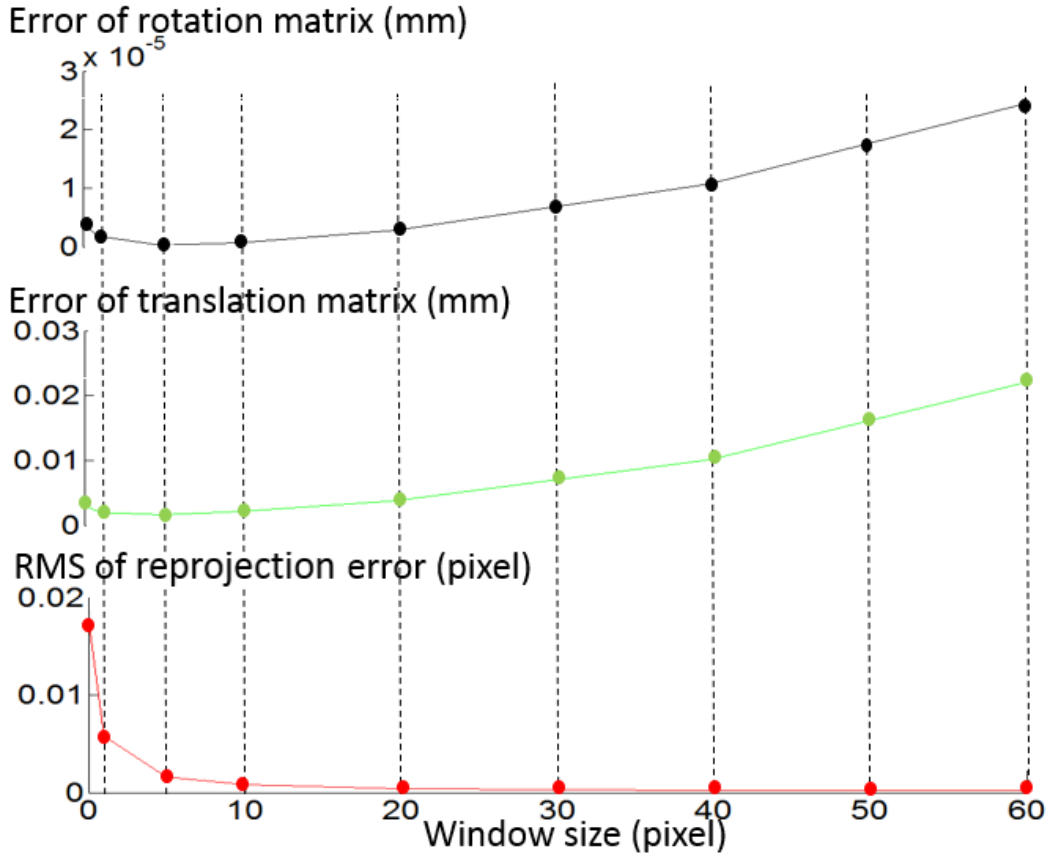


Figure 4.6 The variety of reprojection error, error of rotation matrix and error of translation matrix along with the variety of window size.

## 4.2 Results and discussion

### 4.2.1 Simulation study

In order to verify the studied camera calibration method, a camera is simulate and calibrated. Radial distortion, eccentric distortion and thin prism distortion are denoted as  $(\Delta_{ur}, \Delta_{vr})$ ,  $(\Delta_{ue}, \Delta_{ve})$  and  $(\Delta_{up}, \Delta_{vp})$  respectively. Distortion coefficients are simulated based on Eq. (4.11). Distortion centre is (808,608) pixel.  $k_1 = 3 \times 10^{-8}$  pixel,  $k_2 = 3 \times 10^{-14}$  pixel,  $k_3 = 1 \times 10^{-20}$  pixel,  $k_4 = 1 \times 10^{-26}$  pixel,  $p_1 = 1 \times 10^{-5}$  pixel,  $p_2 = 1 \times 10^{-5}$  pixel,  $s_1 = 5 \times 10^{-5}$  pixel,  $s_2 = 5 \times 10^{-5}$  pixel.

$$\left\{ \begin{array}{l} \Delta_{ur} = u_p(k_1r^2 + k_2r^4 + k_3r^6 + k_4r^8) \\ \Delta_{vr} = v_p(k_1r^2 + k_2r^4 + k_3r^6 + k_4r^8) \\ \Delta_{ue} = 2p_1u_pv_p + p_2(u_p^2 + 3v_p^2) \\ \Delta_{ve} = p_1(3u_p^2 + v_p^2) + 2p_2u_pv_p \\ \Delta_{up} = s_1(u_p^2 + v_p^2) \\ \Delta_{vp} = s_2(u_p^2 + v_p^2) \end{array} \right. \text{ with } r = \sqrt{u_p^2 + v_p^2} \quad (4.11)$$

where  $(u_p, v_p)$  is true camera pixel. True camera pixels and distorted pixels are shown in Fig. 4.7. Eight LCD pose are simulated with  $r_1 = [2.7695^\circ, -2.7856^\circ, -0.1811^\circ]^T$ ,  $t_1 = [0.7916, -0.4575, -2.7113]^T$ ,  $r_2 = [2.8293^\circ, -2.7519^\circ, -0.2241^\circ]^T$ ,  $t_2 = [0.7275, -0.3875, 2.7896]^T$ ,  $r_3 = [3.0690^\circ, -2.6283^\circ, -0.2358^\circ]^T$ ,  $t_3 = [0.5033, -0.4775, 2.8014]^T$ ,  $r_4 = [2.8311^\circ, -2.7483^\circ, -0.3103^\circ]^T$ ,  $t_4 = [0.7353, -0.0266, 3.1896]^T$ ,  $r_5 = [2.8887^\circ, -2.7270^\circ, -0.0773^\circ]^T$ ,  $t_5 = [0.7295, -0.4887, 2.8933]^T$ ,  $r_6 = [3.0078^\circ, -2.6686^\circ, -0.1458^\circ]^T$ ,  $t_6 = [0.5983, -0.4071, 2.9964]^T$ ,  $r_7 = [-3.1212^\circ, -2.5625^\circ, -0.3108^\circ]^T$ ,  $t_7 = [0.3537, -0.2911, 3.1097]^T$ ,  $r_8 = [2.8760^\circ, -2.7257^\circ, -0.2398^\circ]^T$ ,  $t_8 = [0.7231, -0.0588, 3.3075]^T$ . Absolute phase map are randomly added with phase noise ranging from 0 to 0.005 radian. By using reprojection error to evaluate the calibration result, Fig. 4.8 shows the calibration result obtained with the studied camera calibration technique. The experimental result verify camera calibration technique described in this chapter can effectively eliminate camera distortion.

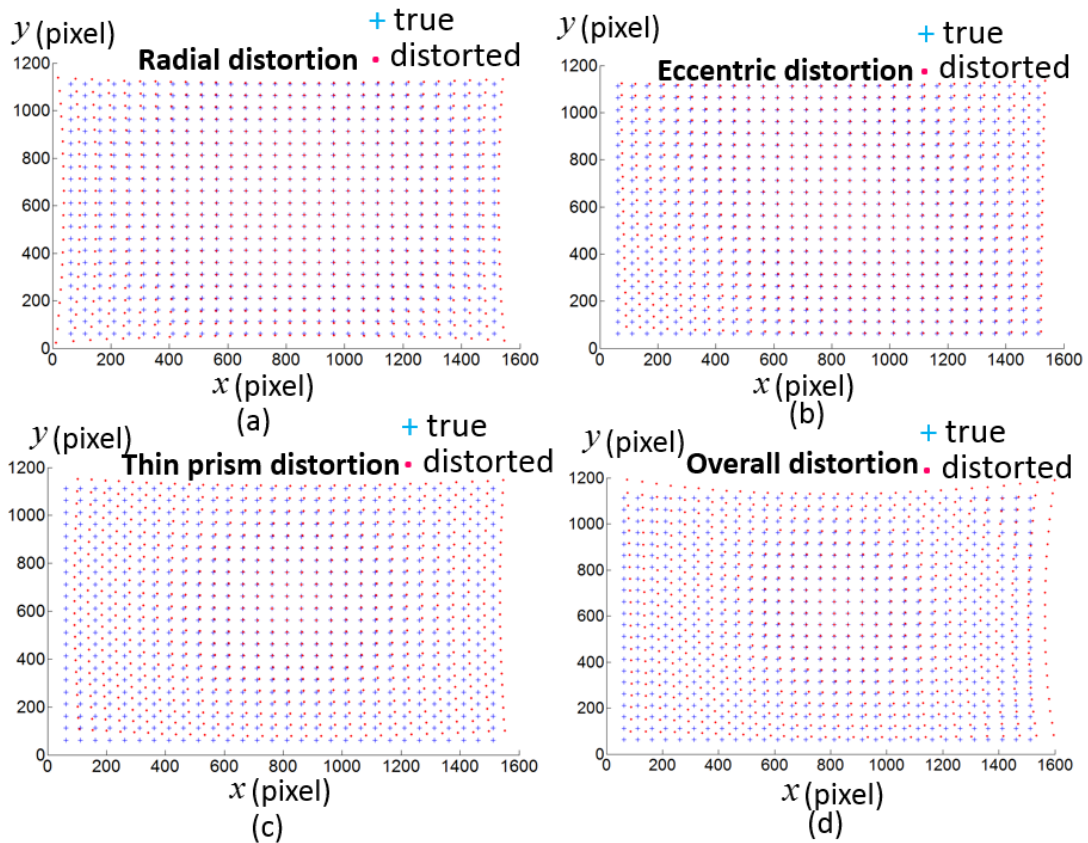


**Figure 4.7 True camera pixel and distorted camera pixel. (a) Influence of radial distortion ; (b) influence of eccentric distortion; (c) influence of thin prism distortion; (d) overall influence of radial distortion, eccentric distortion and thin prism distortion.**

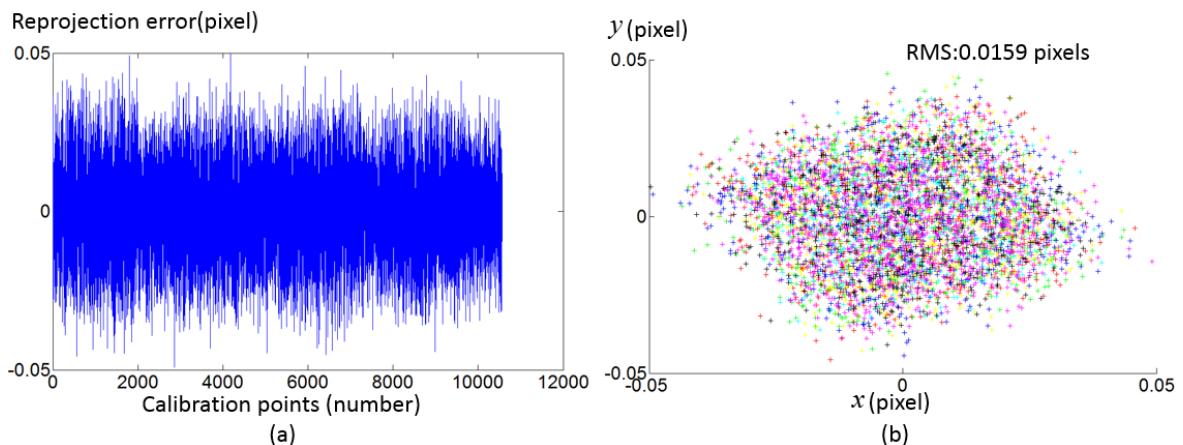


**Figure 4.8 Calibration result obtained with the studied camera calibration technique. (a) Reprojection error of calibration along x and y direction; (b) reprojection error expressed in terms of pixel coordinate. 8 colours are used to distinguish different calibration poses.**

## 4.2.2 Experiment study

A CCD camera with 35 mm fixed focal lens is calibrated to test the studied camera calibration technique, as shown in Fig. 4.9. The camera is from Lumenera (<https://www.lumenera.com/>) with

model of Lw235M. The lens is manufactured by Navitar (<https://navitar.com/>). The resolution of the camera is  $1616 \times 1216$  pixels. Phase target is displayed on a LCD screen. Model of the screen is Dell E151Fpp. The LCD's pixel size of is 0.297 mm. The resolution of the screen is  $1024 \times 768$  pixels. Eleven calibration poses are used during the calibration. Absolute phase maps were optimized by using the studied fitting and interpolating algorithm with a  $5 \times 5$  fitting window. Every 10th camera pixel was selected to form a grid with the size of  $161 \times 121$  as the input to calibrate the cameras with the corresponding points in the world coordinates. The distortions of the selected pixels under the linear projection model are shown in Fig. 4.10. Since Zhang's calibration approach ([Zhang 2000](#)) is very popular in practical applications, a comparative experiment has been made between the proposed method and Zhang's approach as shown in Fig. 4.11. RMS of the calibration error obtained with Zhang's calibration approach is 0.033 pixels. The calibration error decreases to 0.025 pixels when using the studied fitting technique to optimize phase value. In contrast, RMS of the calibration error of the investigated camera calibration method is 0.015 pixels. The experimental result demonstrates the investigated camera calibration method is 1.6 times accurate than Zhang's calibration approach.

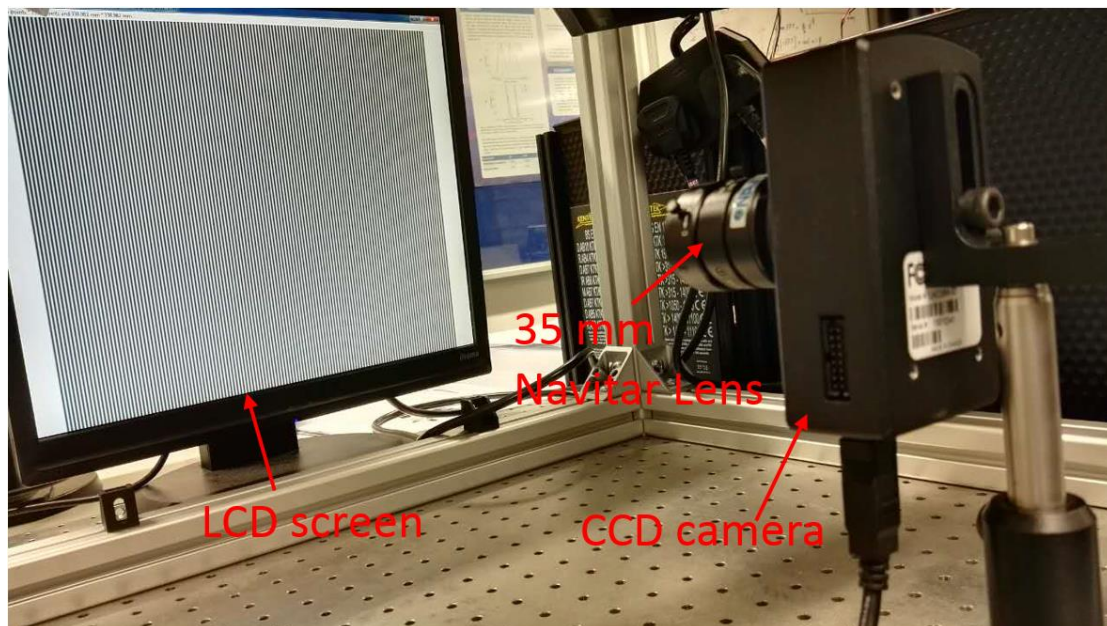
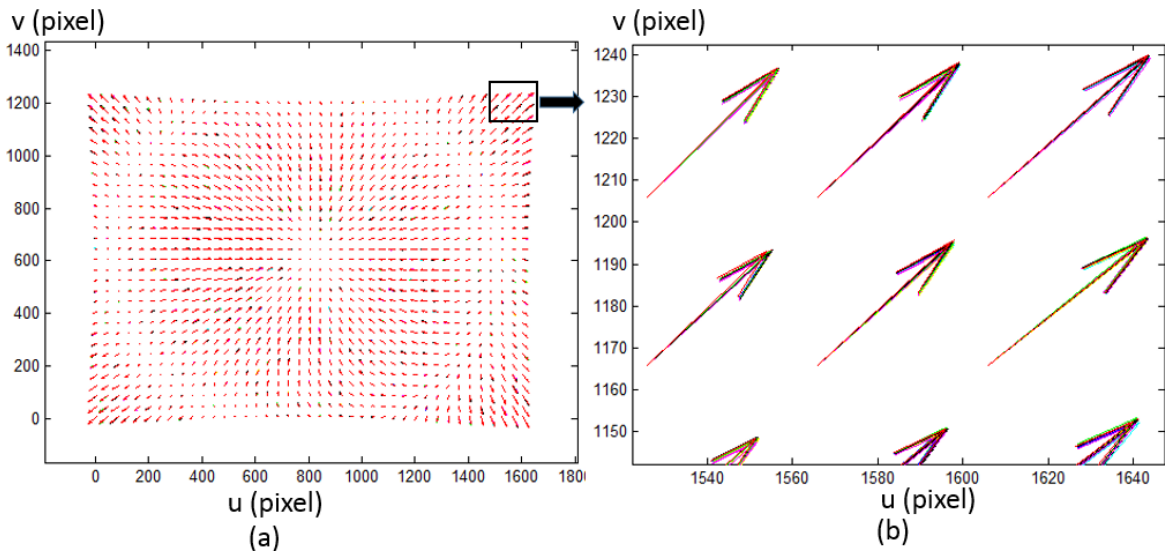
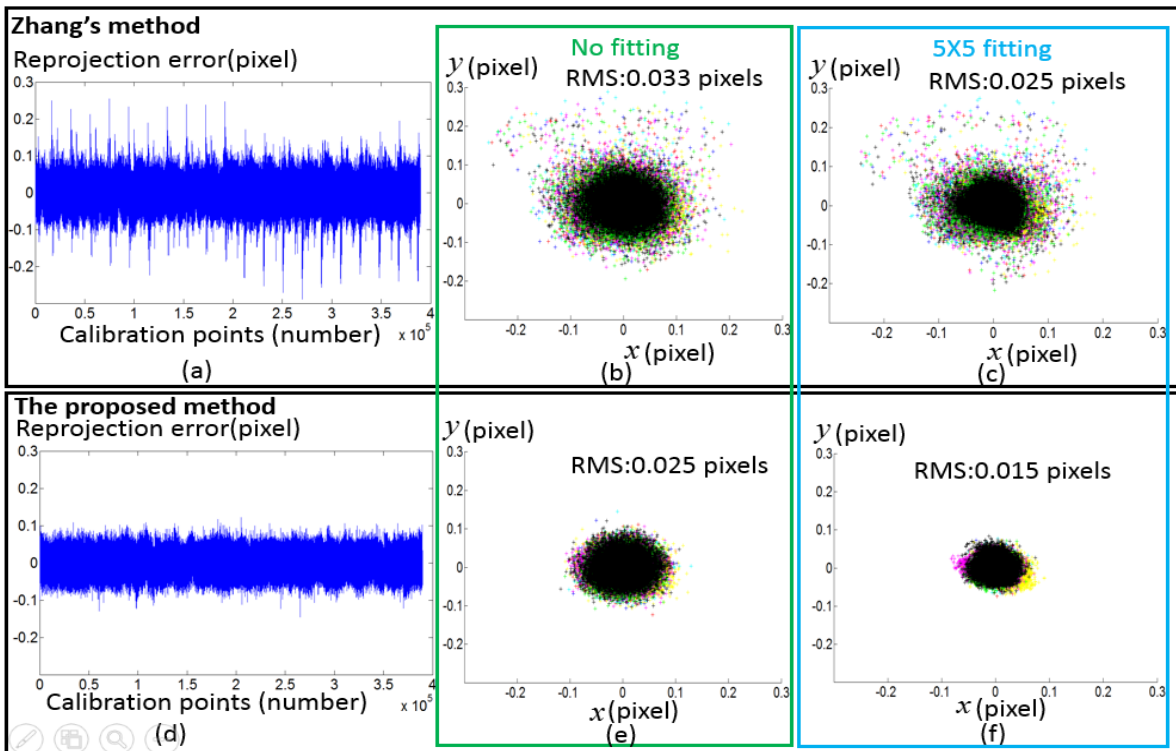


Figure 4.9 Setup for testing the studied camera calibration technique.



**Figure 4.10** The obtained camera distortion. (a) Camera distortion of the chosen camera pixels; (b) enlargement of the right-top corner of (a). Different colours are used to distinguish different calibration poses.



**Figure 4.11** Comparison between the studied camera calibration technique and Zhang's calibration method. (a) Calibration error obtained of Zhang's method without using fitting optimization technique; (b) calibration error expressed in pixel coordinate of Zhang's method without using fitting optimization technique; (c) calibration error expressed in pixel coordinate of Zhang's method by using fitting optimization technique; (d) calibration error of the studied camera calibration technique without using fitting optimization technique; (e) calibration error expressed in pixel coordinate of the studied camera calibration technique without using fitting optimization technique; (f) calibration error expressed in pixel coordinate of the studied camera calibration technique by using fitting optimization technique. Different colours are used to distinguish different calibration poses.

### **4.3 Summary**

This chapter describes a camera calibration technique based on phase target. Camera distortion is eliminated with an iterative distortion compensation technique. Defocus techniques and fitting and interpolation techniques are investigated to improve feature extraction accuracy of phase target. Comparing with traditional camera calibration methods, the studied camera calibration technique can achieve better calibration accuracy.

## 5. Calibration of non-overlapping camera system

In some applications, the field of view of sensors in a system cannot have an overlapped area. In this case, the current available camera calibration methods ([Maoling, Songde et al. 2000](#), [Zhang 2000](#)) cannot be used. The fringe-displaying screen of a stereo deflectometry system is applied as phase target to conduct calibration process. Because cameras in stereo deflectometry have common fields on the surface under measurement, their fields on phase target are non-overlapping. When carrying out calibration, stereo deflectometry is a non-overlapping camera system, as shown in Fig. 5.1. Therefore, designing a new calibration method for non-overlapping camera systems is of necessity. In this chapter, the fringe-displaying screen in stereo deflectometry is used as a phase target to calibration the cameras in the system. An optical flat is applied to enable the cameras can capture phase target during the calibration. The relation between the cameras and imaging parameters of each camera are obtained based on a studied algorithm. The work in this chapter generated one journal paper ([Xu, Gao et al. 2018](#)).

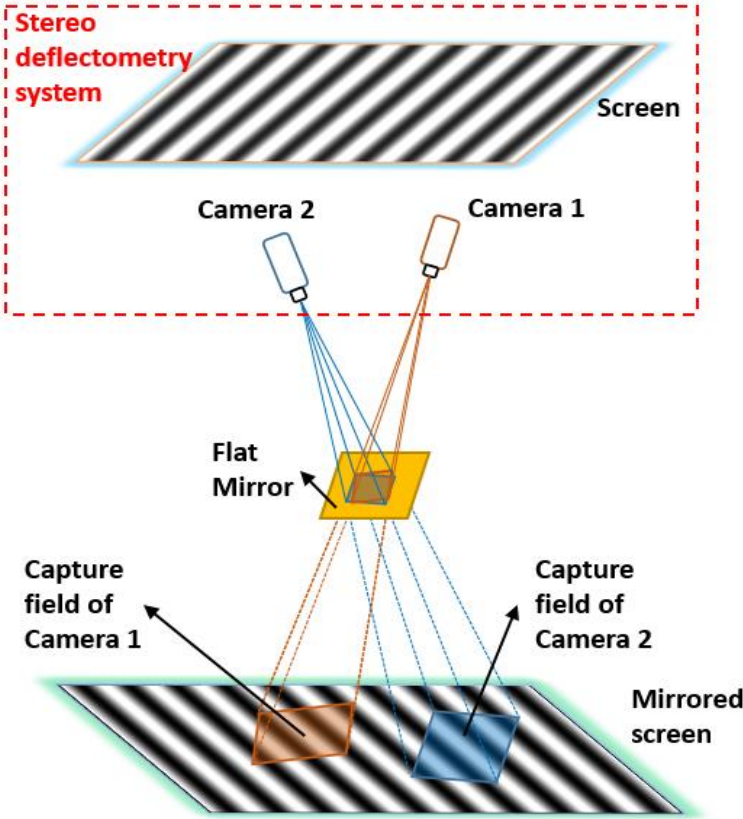


Figure 5.1 Stereo deflectometry can be treated as a non-overlapping camera systems when doing calibration.

## 5.1 Principle of the proposed calibration method for non-overlapping cameras system

Fig. 5.2 illustrates principle of the studied calibration technique in this chapter. A LCD screen is used as phase target during calibration. A group of horizontal sinusoidal fringe patterns and a group of vertical sinusoidal fringe patterns are displayed on a LCD screen in turn. Non-overlapping cameras capture these fringe patterns through an optical flat's reflection. Two orthogonal absolute phase maps are acquired by applying phase-shifting and phase unwrapped algorithm (Towers, Towers et al. 2005).

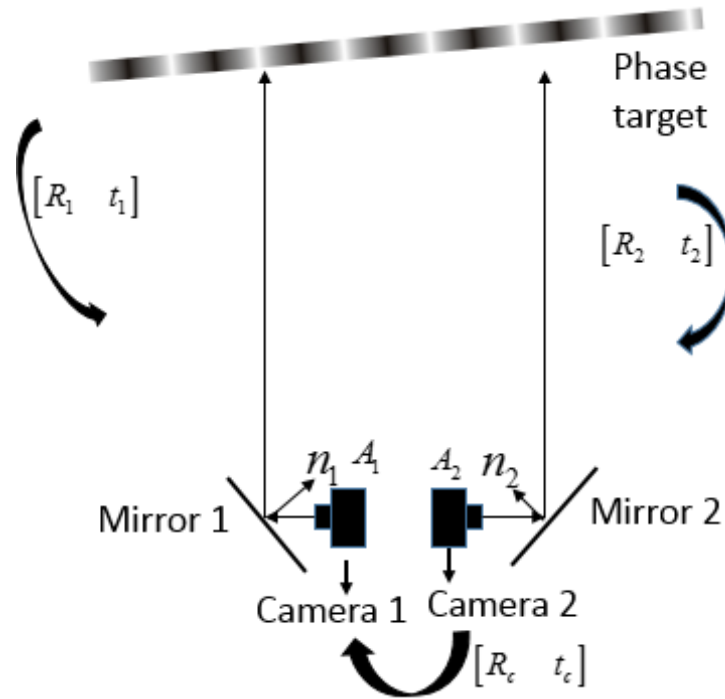


Figure 5.2 The principle of the studied calibration technique.

Knowing two orthogonal absolute phase values, physical location of control point on phase target can be acquired based on Eq. (5.1).

$$\begin{cases} x_w = (n_p \cdot p / 2\pi) \cdot \varphi_x \\ y_w = (n_p \cdot p / 2\pi) \cdot \varphi_y \end{cases} \quad (5.1)$$

where  $(x_w, y_w)$  represents physical location of control point. LCD pixel size is denoted as  $p$ .  $\varphi_x$  and  $\varphi_y$  are horizontal phase value and vertical phase value respectively. The number of LCD pixels per fringe period is expressed with  $n_p$ . Based on Eq. (5.2), camera's imaging parameter and

the relation between control point in terms of phase target coordinate and its image point in terms of camera imaging plane coordinate can be calculated. Camera parameter  $A_1$  and the relation  $[R' \ t']$  between mirrored screen and the camera coordinate system can be obtained based on the pinhole model by moving mirror 1 to at least 3 arbitrary positions:

$$sm = A_1 \cdot [R' \ t'] \cdot M' \quad (5.2)$$

where  $A_1$  represents camera's imaging parameter. The relation between two coordinates consists with a rotation matrix  $R'$  and a translation matrix  $t'$ . Based on Eq. (5.3),  $R'$  and  $t'$  can be obtained by placing the optical flat at more than three positions.

$$\begin{cases} R' = (I - 2nn^T)R_1 \\ t' = (I - 2nn^T)t_1 + 2dn \end{cases} \quad (5.3)$$

where  $d$  represents the physical distance between optical centre of the calibrated camera and optical flat. The normal vector of optical flat is denoted as  $n$  which can be acquired according to Eq. (5.4).

$$\begin{cases} n_i = (m_{ik} \times m_{ij}) / \|m_{ik} \times m_{ij}\| \\ n_j = (m_{ji} \times m_{jk}) / \|m_{ji} \times m_{jk}\| \\ n_k = (m_{ik} \times m_{jk}) / \|m_{ik} \times m_{jk}\| \end{cases} \quad (5.4)$$

where  $m$  represents a unit vector that is perpendicular to two optical flat's normal vectors at the same time. Three arbitrary locations of optical flat are denoted as  $i, j, k$ . Eq. (5.5) is used to obtain the value of  $m$ .

$$\begin{cases} (R'_i - R'_j)^T \cdot m_{ij} = 0 \\ (R'_j - R'_k)^T \cdot m_{jk} = 0 \\ (R'_i - R'_k)^T \cdot m_{ik} = 0 \end{cases} \quad (5.5)$$

A linear equation shown in Eq. (5.6) is used to calculate  $d$ .

$$\begin{bmatrix} (I - n_1 n_1^T) 2n_1 & 0 & 0 \\ (I - n_2 n_2^T) 0 & 2n_2 & 0 \\ (I - n_3 n_3^T) 0 & 0 & 2n_3 \end{bmatrix} \begin{bmatrix} t_1 \\ d_i \\ d_j \\ d_k \end{bmatrix} = \begin{bmatrix} t'_1 \\ t'_j \\ t'_k \end{bmatrix} \quad (5.6)$$

where  $I$  is a 3x3 identity matrix. By making Eq. (5.7) reach minimization using Levenberg-Marquardt Algorithm, the above calculated imaging parameters can be optimized.

$$\sum_{i=1}^g \sum_{j=1}^k \|m_{ij} - \hat{m}(A_i, R_{1i}, t_{1i}, n_i, d_i, M_{ij})\| \quad (5.7)$$

where  $M$  represents control points on phase target. Its image point on camera imaging plane is expressed with  $m$ . The number of  $m$  is denoted as  $k$ . Optical flat's position number is  $g$ . Imaging parameters of the other camera can be obtained by using the same calibration technique. By treating phase target as an intermediate value, the relation between cameras can be acquired based on Eq. (5.8).

$$\begin{cases} R_c = R_2 \cdot R_1^{-1} \\ t_c = t_2^{-1} - R_2 \cdot R_1^{-1} \cdot t_1^{-1} \end{cases} \quad (5.8)$$

where  $R_1$  and  $t_1$  represent rotation matrix and translation matrix between Camera 1 and phase target respectively.  $R_2$  and  $t_2$  represent rotation matrix and translation matrix between Camera 2 and phase target respectively.  $R_c$  and  $t_c$  represent rotation matrix and translation matrix between cameras respectively. Fig. 5.3 shows workflow of the studied calibration technique.

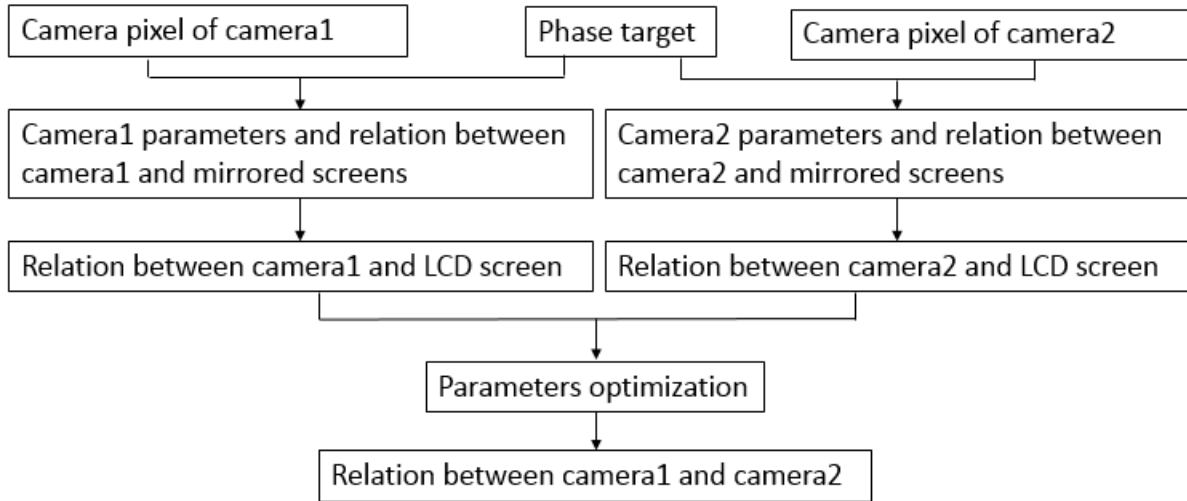


Figure 5.3 Summary of the studied calibration technique's workflow.

## 5.2 Experiment and results

### 5.2.1 Simulation study

Fig. 5.4 shows a simulated non-overlapping camera system which is used to verify the studied calibration technique. Two camera are simulated in the system. The Euler angles of rotation matrix between the two camera's coordinate systems are  $\alpha$  of  $0^0$ ,  $\beta$  of  $0^0$ , and  $\gamma$  of  $180^0$ . Translation vector between the two camera's coordinate system is 0 mm along x direction, 0 mm along y direction, 35 mm along z direction. Phase target displayed on a screen is applied to calculate the relation between the two cameras. Physical location noise randomly varying within 0.005 mm are added into control points' location on the phase target. Based on the calibration technique described in this chapter, calibration results are obtained as shown in Tab. 5.1. The calibration results are compared with the true relation between the two cameras. Tab. 5.1 shows the difference between the true value and the result based on the studied calibration technique is 0.2 mm in translation and 0.007 degree in rotation.

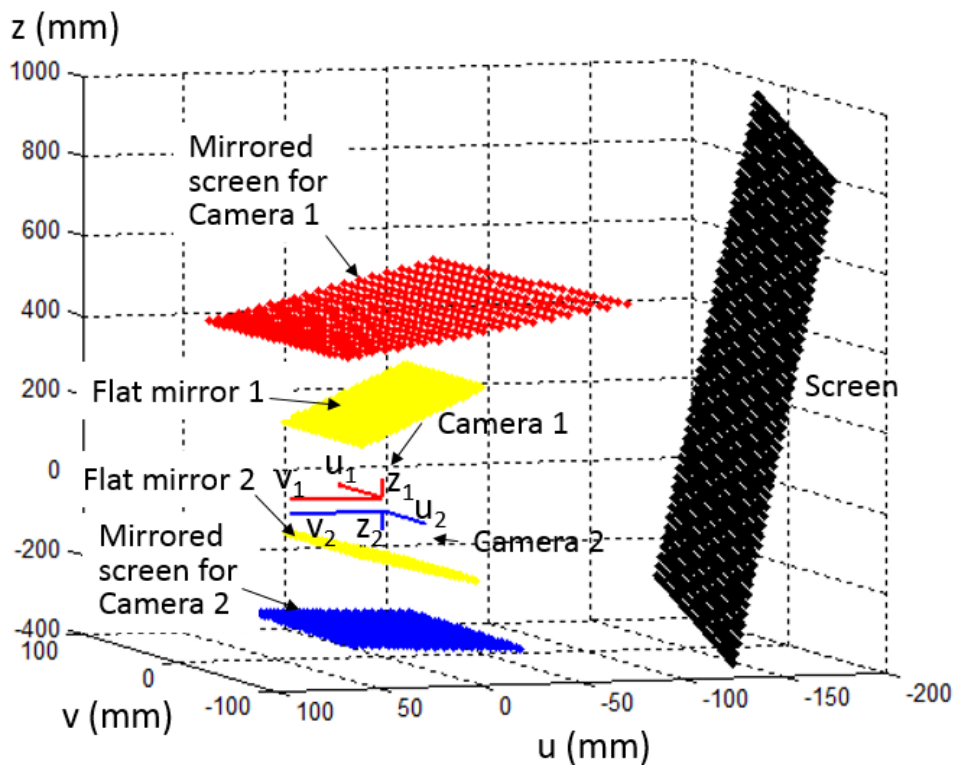


Figure 5.4 A simulated non-overlapping camera system.

**Table 5.1 Comparison between the calibration results and the true value.**

Relative poses	Euler angles			Relative translation		
	$\alpha[^\circ]$	$\beta[^\circ]$	$\gamma[^\circ]$	$t_x[mm]$	$t_y[mm]$	$t_z[mm]$
True value	0	0	180	0	0	35
Calibration result	-0.0069	0.0024	179.9987	-0.00	-0.19	35.11
Residual	0.0069	0.0024	0.0013	0.00	0.19	0.11

### 5.2.2 Experimental study and discussion

With the purpose of testing the studied calibration technique, a non-overlapping cameras system shown in Fig. 5.2 was calibrated. Two CCD cameras with model Lw235M from Lumenera (<https://www.lumenera.com/>) were set up for the non-overlapping cameras system. Because the relation between the two cameras' coordinate system is hard to be known accurately, the value of this relation is estimated based on the two cameras' geometric position. Euler angles of the rotation matrix between the two cameras' coordinate system are  $\alpha$  of  $0^0$ ,  $\beta$  of  $0^0$ , and  $\gamma$  of  $180^0$ . Translations vector between the two cameras' coordinate systems is 0 mm along u direction and 0 mm along v direction. A LCD screen with model Dell E151Fpp is acted as phase target. Tab. 5.2 shows the calibration result obtained with the studied calibration technique.

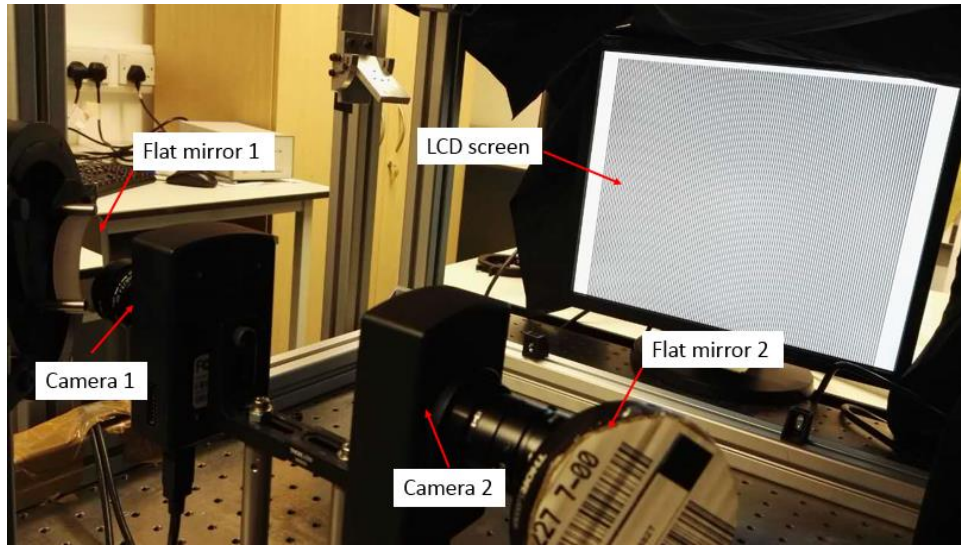


**Figure 5.5** A tested non-overlapping cameras system.

**Table 5.2** Calibration result with experimental data.

Relative poses	Euler angles			Relative translation	
	$\alpha[^\circ]$	$\beta[^\circ]$	$\gamma[^\circ]$	$t_x[mm]$	$t_y[mm]$
Estimated value	0	0	180	0	0
Calibration result	-0.9851	-0.8834	-179.5616	-4.94	6.22

### 5.3 Summary

In order to investigate the systemic calibration of stereo deflectometry, a particular calibration technique is discussed in this chapter. Because the cameras of a stereo deflectometry system cannot have an overlapped field of view on calibration target, a calibration technique for non-overlapping camera system is studied. The studied calibration technique is more suitable for stereo deflectometry than other calibration method for non-overlapping camera system. Experimental results verified the flexibility and accuracy of the studied calibration technique. The studied calibration technique not only can be used in calibration of a stereo deflectometry system, but also can be applied in the calibration of other non-overlapping cameras systems. A test will be

conducted in the future by using the studied calibration method to calibrate other non-overlapping cameras systems.

In the next chapter, a systemic calibration technique for a stereo deflectometry system based on the calibration technique described in this chapter will be represented.

## **6. Holistic system calibration method for stereo deflectometry**

Aiming to improve measurement accuracy of stereo deflectometry, a systemic calibration method for a stereo deflectometry system is investigated in this chapter. The method is based on the work described in chapter 4 and chapter 5. The gradient information of the measured surface is the primary data of the reconstruction results of stereo deflectometry. Calibration correctness of stereo deflectometry significantly affects the accuracy of surface gradient. Therefore, the accuracy of stereo deflectometry's systemic calibration plays an important role in measurement accuracy of the system. The studied systemic calibration approach enhances calibration accuracy of a stereo deflectometry system by improving the compensation accuracy of systemic distortion. The studied calibration technique applies an iterative distortion compensation algorithm rather than the distortion model used in traditional stereo deflectometry's calibration method. Works in this part generated one journal paper ([Xu, Gao et al. 2018](#)).

An algorithm is also presented in this chapter to increase the accuracy and robustness of the calibration of stereo deflectometry system. Holistic calibration algorithms are generally based on iterative computation and therefore heavily sensitive to the accuracy of input initial values. This chapter investigates a search algorithm with an evaluation function to solve the low-accuracy initial value problem caused by image distortion for holistic calibration technique. Accurate initial values are searched with a window moving within camera image, and determined by making the proposed evaluation function reach the minimum. Experiments affirm the studied algorithm can noticeable increase stereo deflectometry's calibration accuracy. The RMS of calibration error can be reduced to 0.05 pixels from 0.31 pixels by using the proposed algorithm. One journal paper (A search algorithm for accuracy improvement of holistic calibration of stereo deflectometry, submitted) has been generated based on the work.

### **6.1 Holistic calibration method with iterative distortion compensation**

#### **6.1.1 Principle of the proposed holistic calibration method**

Fig. 6.1 shows the structure of a stereo deflectometry system. A main camera (Camera 1) and a reference camera (Camera 2) makes up a stereo sensor system. A LCD screen is used to display fringe patterns. In order to achieve accurate measurement result, the relations between the main

camera, the reference camera and the fringe-display screen are required to be obtained very accurately.  $A_1$  and  $A_2$  represent imaging parameters of the main camera and the reference camera respectively.  $A_1$  is the transformation from the camera coordinate system  $\{C_1\}$  to the pixel coordinate system  $\{P_1\}$  of the main camera.  $A_2$  is the transformation from the camera coordinate system  $\{C_2\}$  to the pixel coordinate system  $\{P_2\}$  of the reference camera. The relation between different components consists with a rotation matrix and a translation vector. The rotation matrix and the translation vector form  $\{C_1\}$  to  $\{C_2\}$  are represented with  $R_c$  and  $t_c$  respectively.  $R_1$  and  $t_1$  represent the rotation matrix and the translation vector from the screen's system  $\{L\}$  to  $\{C_1\}$ .  $R_2$  and  $t_2$  represent the rotation matrix and the translation vector form  $\{L\}$  to  $\{C_2\}$ .

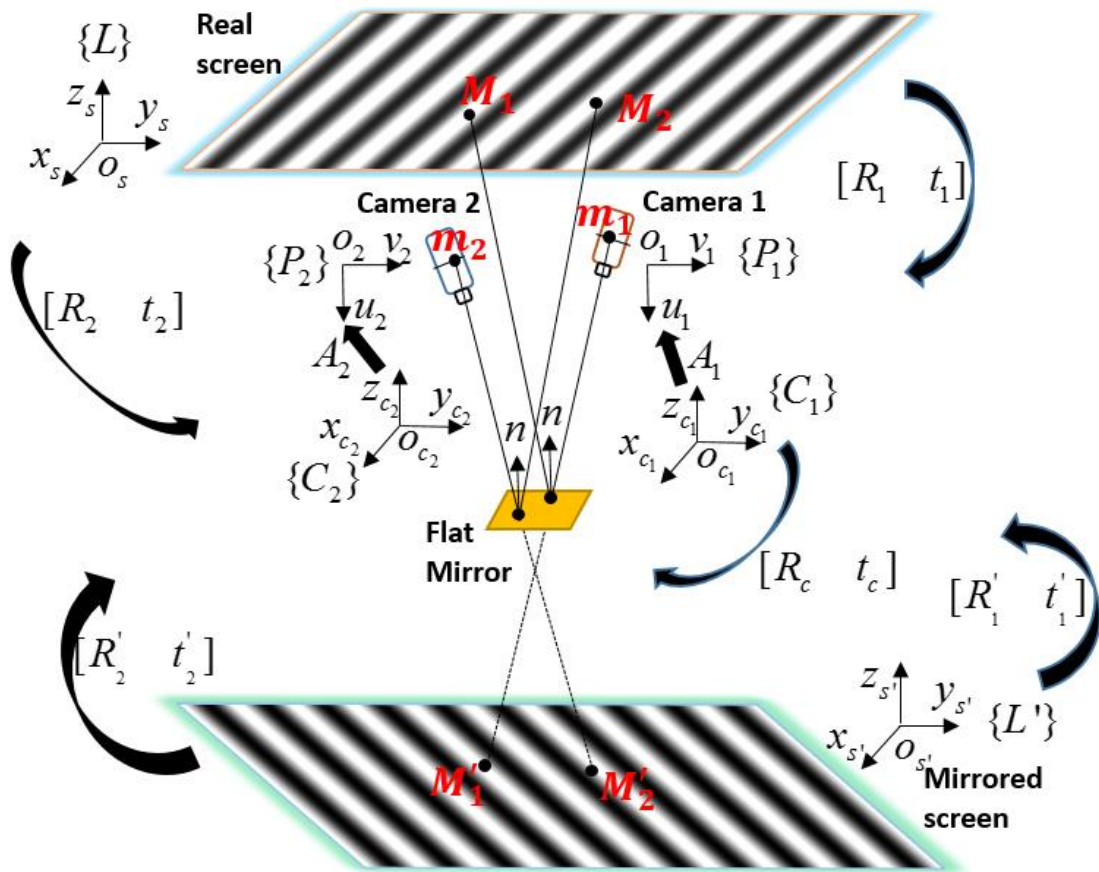


Figure 6.1 The structure of a stereo deflectometry system.

An optical flat mirror is applied to enable the main camera and the reference can capture the displayed fringe patterns on the screen. A group of horizontal sinusoidal fringe patterns and a group of vertical sinusoidal fringe patterns are displayed on the screen in turn. The fringe patterns

have frequency difference ([Werling 2011](#)) because of the requirement of phase unwrapping algorithm. The main camera and the reference capture the reflected fringe patterns simultaneously. A horizontal phase map and a vertical phase map are acquired by applying phase-shifting and phase unwrapped algorithm ([Towers, Towers et al. 2005](#), [Zhang, Towers et al. 2006](#)).

Defining  $x_w$  and  $y_w$  as the physical location of control point on phase target along x and y direction respectively. Based on Eq. (5.1),  $x_w$  and  $y_w$  can be acquired by knowing two orthogonal absolute phase values.

$$\begin{cases} x_w = (n_p \cdot p / 2\pi) \cdot \varphi_x \\ y_w = (n_p \cdot p / 2\pi) \cdot \varphi_y \end{cases} \quad (6.1)$$

where  $\varphi_x$  and  $\varphi_y$  are horizontal phase value and vertical phase value respectively. The number of LCD pixels per fringe period is expressed with  $n_p$ . Defining  $A$  as imaging parameter of a camera. The rotation matrix and the translation vector between mirrored screen's coordinate system  $\{L'\}$  and the camera coordinate system are denoted as  $R'$  and  $t'$  respectively. Based on the pinhole model,  $A$ ,  $R'$  and  $t'$  can be calculated according to Eq. (6.2).

$$sm = A \cdot [R' \quad t'] \cdot M' \quad (6.2)$$

Defining  $R$  and  $t$  as the rotation matrix and the translation vector between  $\{L\}$  and the camera's coordinate system.  $R$  and  $t$  can be obtained based on Eq. (6.3).

$$\begin{cases} R' = (I - 2nn^T)R \\ t' = (I - 2nn^T)t + 2dn \end{cases} \quad (6.3)$$

where  $d$  represents the physical distance between the optical centre of the calibrated camera and the used optical flat. The normal vector of the optical flat is denoted as  $n$ . Eq. (6.4) is used to calculate  $n$ .

$$\begin{cases} n_i = (e_{ik} \times e_{ij}) / \|e_{ik} \times e_{ij}\| \\ n_j = (e_{ji} \times e_{jk}) / \|e_{ji} \times e_{jk}\| \\ n_k = (e_{ik} \times e_{jk}) / \|e_{ik} \times e_{jk}\| \end{cases} \quad (6.4)$$

where  $e$  represents a unit vector that is perpendicular to two optical flat's normal vectors at the same time. Three arbitrary locations of optical flat are denoted as  $i, j, k$ . Eq. (6.5) is used to obtain the value of  $e$ .

$$\begin{cases} (R_i' - R_j')^T \cdot e_{ij} = 0 \\ (R_j' - R_k')^T \cdot e_{jk} = 0 \\ (R_i' - R_k')^T \cdot e_{ik} = 0 \end{cases} \quad (6.5)$$

$d$  in Eq. (6.3) is obtained according to Eq. (6.6).

$$\begin{bmatrix} (I - n_i n_i^T) 2n_i & 0 & 0 \\ (I - n_j n_j^T) 0 & 2n_j & 0 \\ (I - n_k n_k^T) 0 & 0 & 2n_k \end{bmatrix} \begin{bmatrix} t \\ d_i \\ d_j \\ d_k \end{bmatrix} = \begin{bmatrix} t_i' \\ t_j' \\ t_k' \end{bmatrix} \quad (6.6)$$

where  $I$  is a 3x3 identity matrix.

$m$  represents a camera pixel. The distortion of  $m$  is denoted as  $\Delta m$ .  $\Delta m$  can be obtained based on Eq. (6.7).

$$\Delta m = \hat{m}(A, R, t, n, d, M) - m \quad (6.7)$$

where  $M$  is the physical position of a control point on the fringe-displaying screen.  $\hat{m}$  is reprojection pixel calculated based on  $M$  and imaging parameters. The distortion for a certain camera pixel is a constant. The average value of  $\Delta m$  is expressed as  $\overline{\Delta m}$ . The corrected pixel  $m^*$  is acquired according to Eq. (6.8).

$$m^* = m + \overline{\Delta m} \quad (6.8)$$

$A_1, A_2, R_1, t_1, R_2$  and  $t_2$  are iteratively optimized by minimizing Eq. (6.9).

$$[A_1^*, A_2^*, R_1^*, t_1^*, R_2^*, t_2^*] = \min(\|e_1\| + \|e_2\|) \quad (6.9)$$

where  $A_1^*, A_2^*, R_1^*, t_1^*, R_2^*$  and  $t_2^*$  represent the optimized value of  $A_1, A_2, R_1, t_1, R_2$  and  $t_2$ . The difference between  $m^*$  and  $\hat{m}$  of the main camera and the reference camera are expressed with  $e_1$  and  $e_2$  respectively, as shown in Eq. (6.10) and Eq. (6.11).

$$e_1 = \sum_{i=1}^g \sum_{j=1}^k \left\| m_1^*(A_1, R_1, t_1, n_{L_i}, d_{L_i}, M_{1_{ij}}) - \hat{m}_1(A_1, R_1, t_1, n_{L_i}, d_{L_i}, M_{1_{ij}}) \right\| \quad (6.10)$$

$$e_2 = \sum_{i=1}^g \sum_{j=1}^k \left\| m_2^*(A_2, R_2, t_2, n_{L_i}, d_{L_i}, M_{2_{ij}}) - \hat{m}_2(A_2, R_2, t_2, n_{L_i}, d_{L_i}, M_{2_{ij}}) \right\| \quad (6.11)$$

where  $m_1$  and  $m_2$  represent camera pixel of the main camera and the reference camera respectively.  $\hat{m}_1$  and  $m_1^*$  represent the reprojection pixel and the corrected pixel of  $m_1$ .  $M_1$  is the corresponding physical point on fringe-displaying screen of  $m_1$ .  $\hat{m}_2$  and  $m_2^*$  represent the reprojection pixel and the corrected pixel of  $m_2$ .  $M_2$  is the corresponding physical point on the fringe-displaying screen of  $m_2$ . The number of camera pixels and the number of calibration poses are denoted as  $g$  and  $k$  respectively.

Fig. 6.2 summarizes the calibration process of the studied calibration technique.

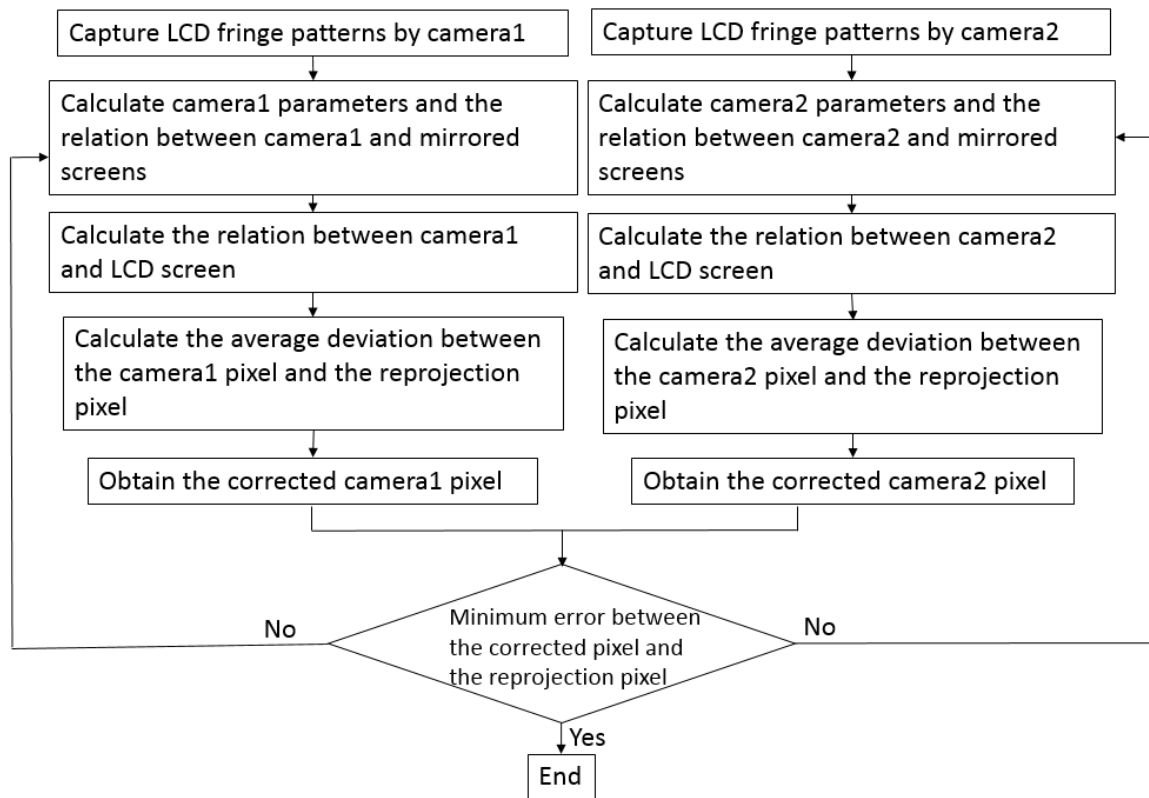


Figure 6.2 Summary of the calibration process of the studied calibration technique.

**6.1.2 Experiment and results**

**6.1.2.1 Simulation**

Fig. 6.3 shows a simulated stereo deflectometry system which is used to verify the studied calibration technique. The simulated system includes two sensors acting as the main camera and the reference camera and a fringe-displaying screen. An optical flat was simulated to enable the two sensors can capture fringe patterns displaying on the screen during calibration process. With the purpose of simulating real measurement noise, physical position noise varying within 0.005 mm was randomly added into the physical position of control points on the fringe-displaying screen.

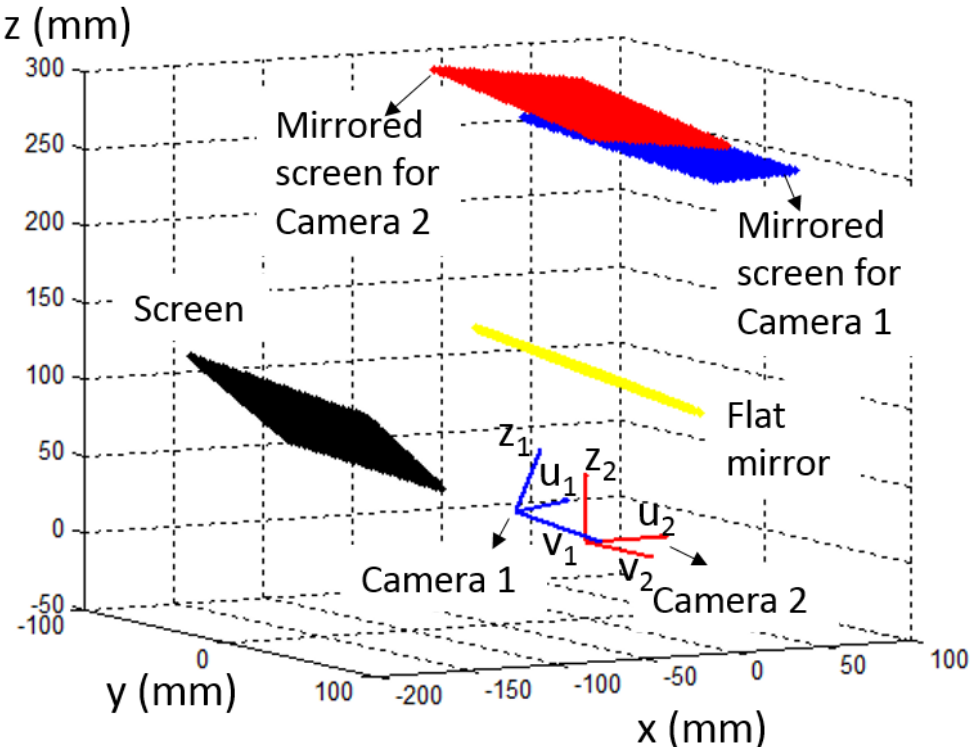
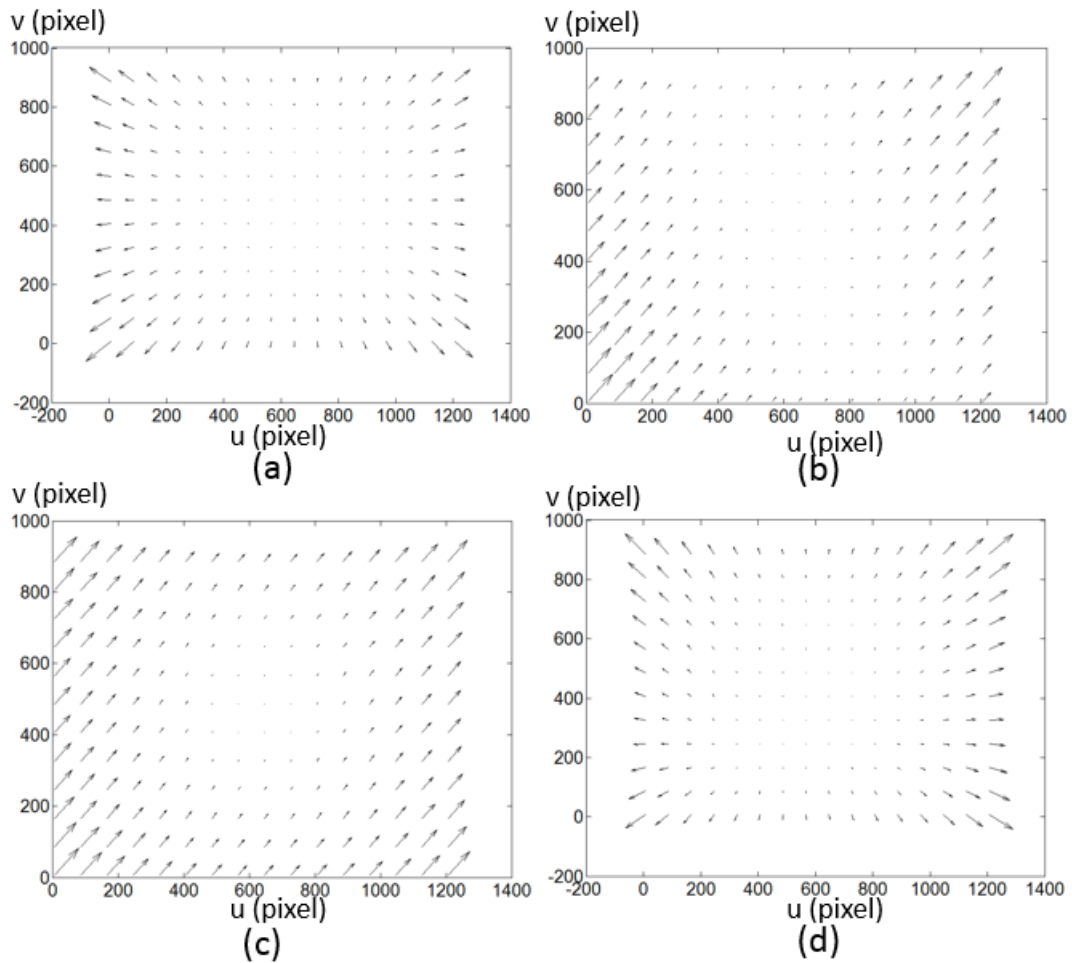


Figure 6.3 The setup of a simulated stereo deflectometry system.



**Figure 6.4** Effect of the simulated camera distortion. (a) Effect of radial distortion ; (b) effect of eccentric distortion; (c) effect of thin prism distortion; (d) an overall effect of three kinds of camera distortion.

Camera distortion was simulated as shown in Fig. 6.4. Fig. 6.4(a), Fig. 6.4(b), Fig. 6.4(c) show the effect of radial distortion, eccentric distortion and thin prism distortion respectively. Fig. 6.4(d) shows an overall influence of radial distortion, eccentric distortion and thin prism distortion. A comparison experiment between a traditional calibration approach ([Ren, Gao et al. 2015](#)) and the studied calibration technique was conducted. Reprojection error is applied to represent calibration accuracy. Reprojection error was converted into a 1D vector from 2D matrix for a better demonstration. Fig. 6.5 shows three calibration results. Fig. 6.5(a) is calculated when no distortion exists in the system. The calibration result acts as a standard. Fig. 6.5(b) is calculated based on the traditional calibration approach. Fig. 6.5(c) is obtained using the studied calibration technique. The calibration result of the studied calibration technique is very close to the standard calibration result. In contrast, calibration result obtained based on traditional calibration approach is far from the result obtained based on the studied calibration technique. Based on the calibration results, an

optical flat was measured. Measurement results of traditional calibration approach and the studied calibration technique are compared in Fig. 6.6. Fig. 6.6(a) indicates the measurement result acquired based on standard calibration result. The PV of the measurement error of Fig. 6.6(a) is 28.2 nm. This measurement result is used as a standard. Fig. 6.6(b) shows the measurement result acquired based on the calibration result of the traditional calibration approach. The PV of the measurement error of the traditional calibration approach is 513 nm. Fig. 6.6(c) shows the measurement result obtained based on the studied calibration technique. The PV of the measurement error is 28.3 nm which is similar to that of the standard calibration result.

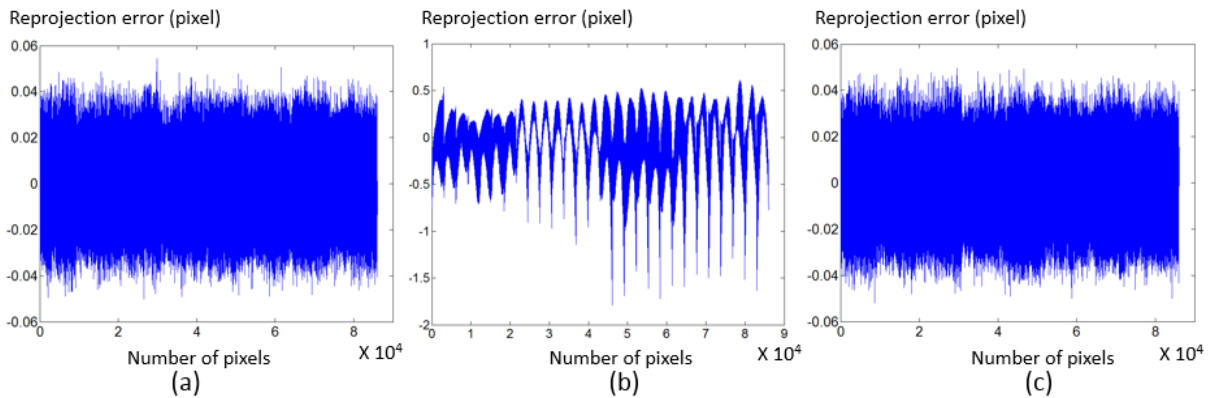


**Figure 6.5 Comparison of calibration results. (a) Calibration results calculated when no distortion exists in the system; (b) calibration result calculated based on traditional calibration approach; (c) calibration result obtained with the studied calibration technique.**

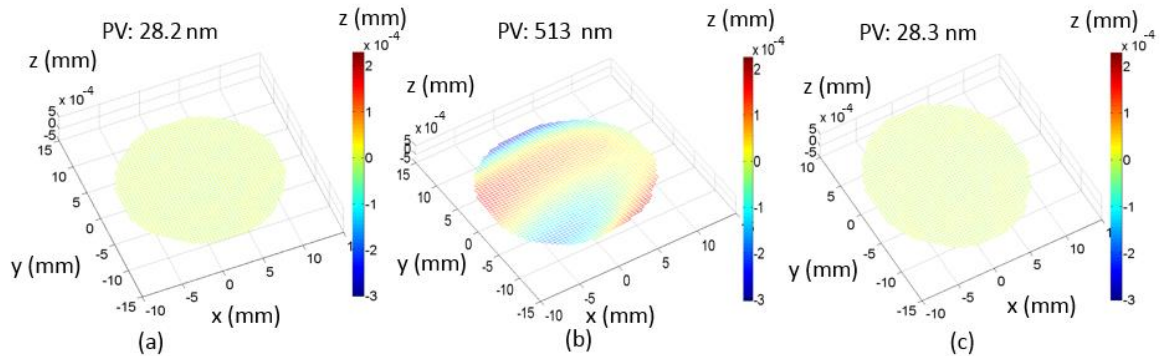


**Figure 6.6 Comparison of measurement results. (a) Measurement result acquired based on the standard calibration result; (b) measurement result acquired based on traditional calibration approach; (c) measurement result acquired based on the studied calibration approach.**

### 6.1.2.2 Experiments and discussion

Experiments have been performed to test the studied calibration technique. Fig. 6.7 shows the applied stereo deflectometry system. An iPad Pro (<https://www.apple.com/ipad-pro/>) with a size of 12.9 inch is used to act as a fringe-displaying screen. iPad Pro can display fringe patterns produced by a computer under the control of Display Duet (<https://www.duetdisplay.com/>). Two

CCD sensors with model Lw235M from Lumenera (<https://www.lumenera.com/>) are used as the main camera and the reference camera. The resolution of the CCD sensors is  $1616 \times 1216$  pixels. The applied camera lens is 35 mm fixed focal lens from Navitar (<https://navitar.com/>). The model of the lens is MVL35M23.

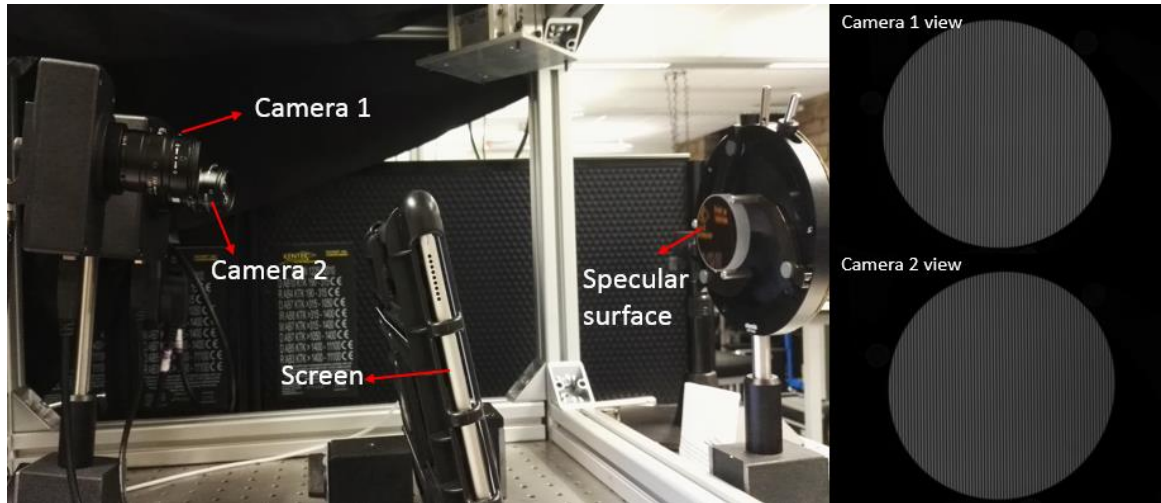


Figure 6.7 The experiment setup.

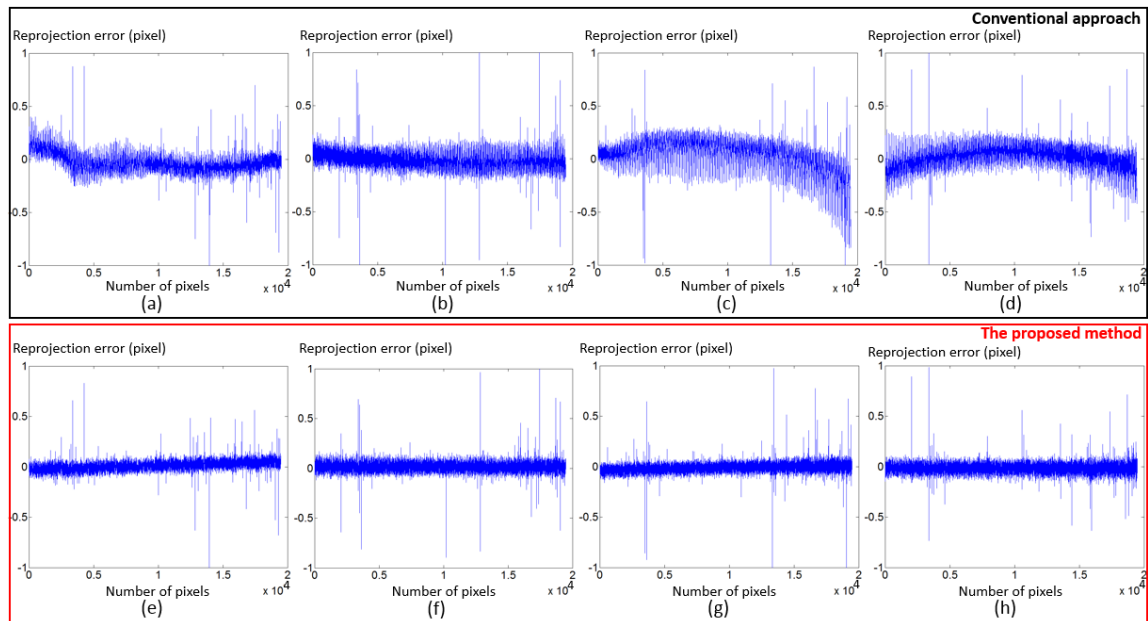
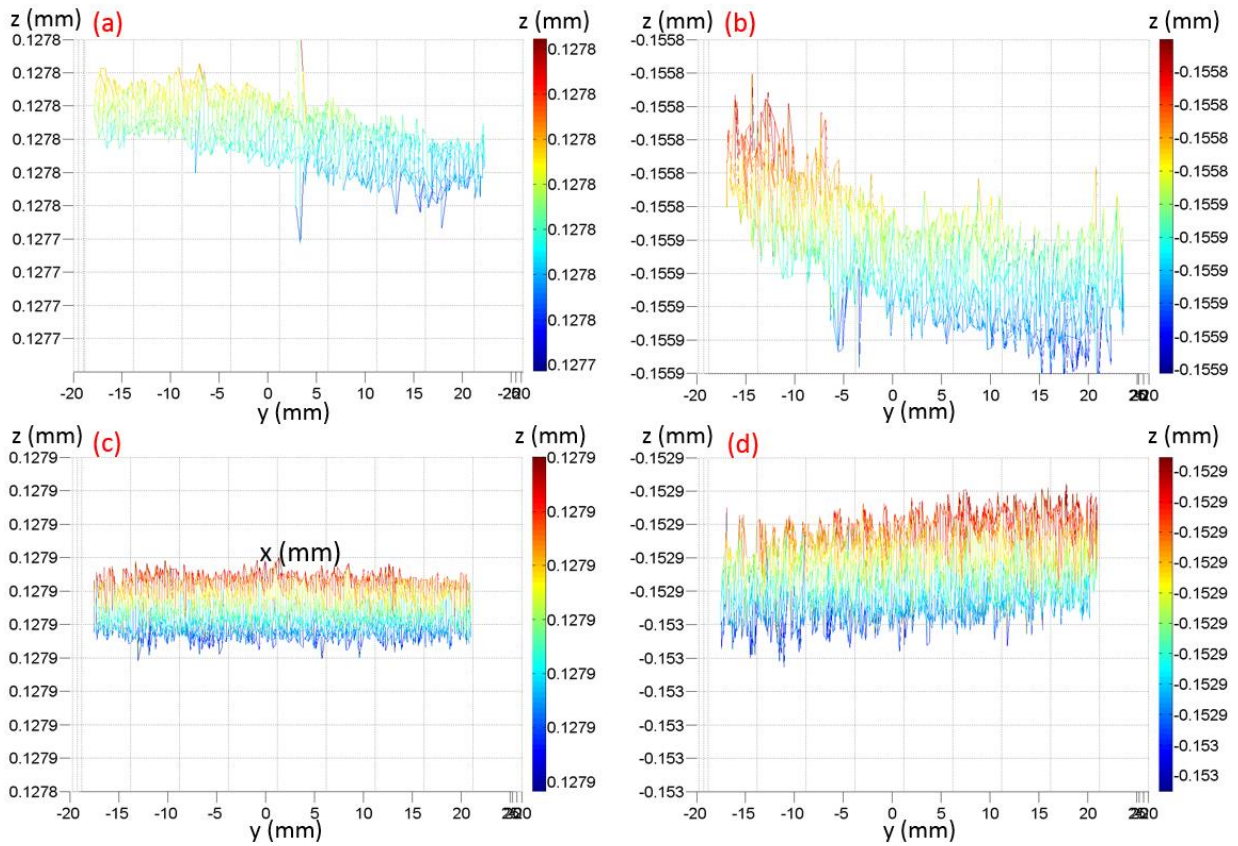


Figure 6.8 Calibration result of main camera and reference camera. (a) Calibration error along x direction of main camera obtained based on traditional calibration method; (b) calibration error along y direction of main camera obtained based on traditional calibration method; (c) calibration error along x direction of reference camera obtained based on traditional calibration method; (d) calibration error along y direction of reference camera obtained based on traditional calibration method; (e) calibration error along x direction of main camera obtained based on the studied calibration technique; (f) calibration error along y direction of main camera obtained based on the studied calibration technique; (g) calibration error along x direction of reference camera obtained based on the studied calibration technique; (h) calibration error along y direction of reference camera obtained based on the studied calibration technique.

An optical flat with  $\lambda/20$  flatness was applied and placed at nine calibration poses during calibration. The size of the optical flat is 4 inch, which is big enough to cover the whole camera field. For each calibration pose of optical flat, based on phase-shifting technique and optimum frequency selection technique ([Towers, Towers et al. 2005](#), [Zhang, Towers et al. 2006](#)), a horizontal absolute phase map and a vertical absolute phase map can be acquired. The physical location of control point on the fringe-displaying screen can be positioned based on its horizontal and vertical phase values. Camera pixels and the corresponding space points on fringe-displaying screen are extracted to conduct the calibration. Fig. 6.8 shows a comparison between the traditional calibration method ([Ren, Gao et al. 2016](#)) and the studied calibration technique. The calibration result obtained with traditional calibration method are shown in Fig. 6.8(a)-(d). Fig. 6.8(a) and Fig. 6.8(b) show calibration error of main camera obtained with traditional calibration method along x and y directions. Fig. 6.8(c) and Fig. 6.8(d) show calibration error of reference camera obtained with traditional calibration method along x and y directions. A noticeable calibration error exists in the calibration result of traditional calibration method. Fig. 6.8(e)-(h) show the calibration result obtained with the studied calibration technique. Calibration error of main camera obtained with the studied calibration technique along x and y directions are shown in 6.8(e) and Fig. 6.8(f). Calibration error of reference camera obtained with the studied calibration technique along x and y directions are shown in 6.8(g) and Fig. 6.8(h). Calibration accuracy of the studied calibration technique is to a greater degree than traditional calibration method.

Based on the calibration results, an optical flat with size of 2 inch was then measured. The flatness of the optical flat is  $\lambda/20$ . Fig. 6.9 shows the calculated gradient data with traditional calibration method and the studied calibration technique. Gradient data obtained with traditional calibration method along x and y directions are shown in Fig. 6.9(a)-(b). Gradient data obtained with the studied calibration technique along x direction and along y direction are shown in Fig. 6.9(c)-(d). Ideally, gradient data of an optical flat is a plane with no slope. Traditional calibration method lead to serious gradient error as shown in Fig. 6.9(a)-(b). Fig. 6.9(c)-(d) reflect that the studied calibration technique can significantly improve gradient calculation accuracy.



**Figure 6.9** The calculated gradient data with traditional calibration method and the studied calibration technique. (a) Gradient data along x direction obtained with traditional calibration method; (b) gradient data along y direction obtained with traditional calibration method; (c) gradient data along x direction obtained with the studied calibration technique; (d) gradient data along y direction obtained with the studied calibration technique.

Two measurement results were reconstructed based on the gradient data calculated with two calibration approaches respectively. In order to avoid the influence of reconstruction algorithm, the measurement results were reconstructed using the same integration technique (Ren, Gao et al. 2016). A comparison between the measurement results are shown in Fig. 6.10. Fig. 6.10(a) shows the measurement error of traditional calibration method. The PV of the measurement error using the traditional calibration method is 282 nm. Fig. 6.10(b) shows the measurement error of the studied calibration technique. The PV of the measurement error using the studied calibration technique is 69.7 nm. Experimental results indicate that the studied calibration technique can acquire much better measurement accuracy than traditional calibration method.

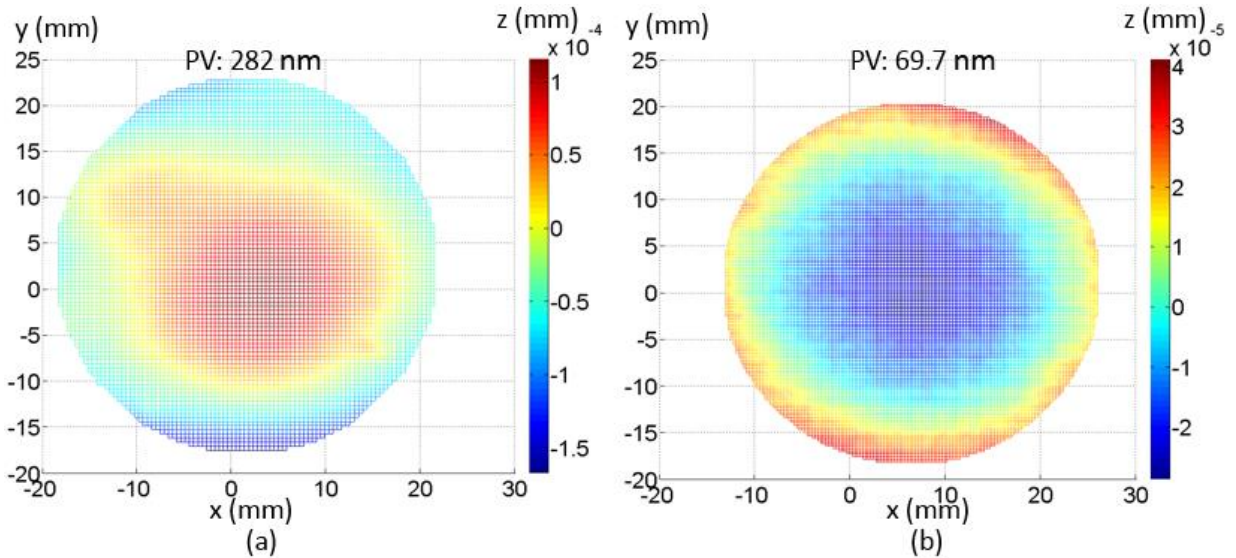


Figure 6.10 A comparison between the measurement results. (a) The measurement error of traditional calibration method; (b) the measurement error of the studied calibration technique.

## 6.2 Robustness improvement of holistic calibration

### 6.2.1 Principle of the proposed search algorithm with an evaluation function

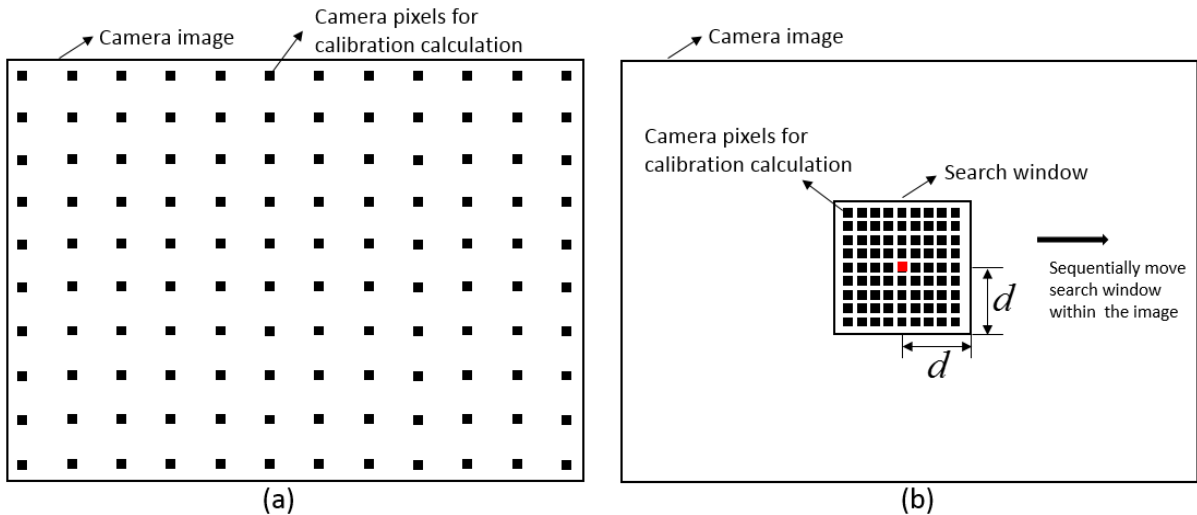


Figure 6.11 The chosen camera pixels for calibration calculation. (a) Previous holistic calibration technique; (b) the proposed calibration method.

Since the measured result is calculated based on the optical geometrical relation of the components in stereo deflectometry, the calibration accuracy plays an important role in the measurement accuracy. Holistic calibration technique (Ren, Gao et al. 2015, Xu, Gao et al. 2018) applies the screen in the system instead of an extra calibration board to calibrate the systemic parameters. Fringe-displaying screen displays a group of horizontal fringe patterns and a group of horizontal

fringe patterns. These patterns are phase-shifting pattern and have fringe frequency difference. Cameras in stereo deflectometry system capture these patterns through the reflection of a flat mirror. Both camera imaging parameters and systemic geometrical parameters are calculated based on camera pixels and their corresponding physical positions on fringe-displaying screen. In order to increase calculation speed, parts of camera pixels instead of full pixels are chosen to conduct the calculation. The chosen pixels of previous holistic calibration technique ([Ren, Gao et al. 2015](#), [Xu, Gao et al. 2018](#)) are evenly distributed on the camera image plane as shown in Fig. 6.11(a). However, due to image distortion, the pixels especially those near image edge deviate from their theoretical positions, which results in obvious calibration error. Though distortion compensation approaches ([Zhang 2000](#), [Xu, Gao et al. 2017](#)) have been proposed to solve the problem through iterative optimization algorithm, the compensation methods greatly depends on the input initial values. When the initial values have large calculation error caused by image distortion, the approaches will fail due to the wrong convergence.

Based on the knowledge that distortion of the pixels near distortion centre can be ignored ([Zhang 2000](#)), a calibration method is proposed to improve the accuracy of initial value, as shown in Fig. 6.11(b). Firstly, a search window with a border length of  $2d$  is defined. The centre of the window coincides with image centre, as the red dot shown. Since the window size is small, the camera pixels within the window are not affected by distortion. Therefore, the calibration result calculated based on the pixels within the window should be accurate. Secondly, considering distortion centre and image centre no not normally coincide, the search window is moved within the image sequentially and an evaluation function is used to confirm the position having the minimum distortion effect. In order to achieve the proposed method successfully, two essential factors of the method are required to be researched: the size of the research window and the evaluation function.

In order to determine the size of the search window, distortion centre is assumed to coincide with image centre.  $d$  decreases from  $d_0$  to 0 in increments of  $a$  as expressed in the following equation:

$$d_i = d_0 - i \cdot a \quad (6.12)$$

where  $d_0$  equals half size of the image border length and  $i$  increases from 0 to the integer part of  $d_0 / a$  in increments of 1. A linear mapping  $H$  can be obtained based on the following equation:

$$m = H \cdot M \quad (6.13)$$

where  $m$  are camera pixels within a search window and  $M$  are control points' physical positions on the mirrored fringe-displaying screen. The deviation  $p$  between  $m$  and the calculated reprojected pixels  $\hat{m}$  under  $H$  can be obtained based on the following equation:

$$p = \hat{m}(H, M) - m \quad (6.14)$$

Because distortion is the main reason affecting the size of  $p$ ,  $p$  reaches the maximum when  $d$  equals  $d_0$  and decreases with decreasing of  $d$ . When the deviations of two adjacent  $d_i$  have little difference, the corresponding  $d$  can be treated as the proper border size of the search window used in the proposed calibration method. An equation is proposed to determine the proper border size by comparing the size of  $p_i$ :

$$RMS(p_i) = \lambda RMS(p_{i+1}) \quad (6.15)$$

where  $RMS$  means the root mean square.  $\lambda$  is used to judge the proper border size of the search window according to the variation trend of  $p_i$ . According to the experience,  $\lambda$  can be set to 1.05.

After determining the size of the search window, the next step is to move the window within camera image to find the true distortion centre. The camera imaging parameter  $A$  is obtained according to Eq. (6.16).

$$s \cdot m = A \cdot [R' \ t'] \cdot M' \quad (6.16)$$

where  $m$  are camera pixels within a search window and  $M'$  are control points' physical locations on fringe-displaying screen.  $R'$  and  $t'$  are rotation matrix and translation vector of the relation between mirrored screen coordinate system and camera coordinate system. With known  $R'$  and  $t'$

, the rotation matrix  $R$  and translation vector  $t$  of from real screen coordinate system to camera coordinate system are obtained according to the following equation:

$$\begin{cases} R = (1/(I - 2nn^T)) \cdot R' \\ t = (1/(I - 2nn^T)) \cdot (t' - 2dn) \end{cases} \quad (6.17)$$

where  $n$  represents the normal vector of the applied mirror. The distance from camera centre to the flat mirror is denoted as  $d$ .  $n$  is obtained based on Eq. (6.18):

$$\begin{cases} n_i = (e_{ik} \times e_{ij}) / \|e_{ik} \times e_{ij}\| \\ n_j = (e_{ji} \times e_{jk}) / \|e_{ji} \times e_{jk}\| \\ n_k = (e_{ik} \times e_{jk}) / \|e_{ik} \times e_{jk}\| \end{cases} \quad (6.18)$$

where  $e$  represents a unit vector and is perpendicular to two mirrors' normal vector. Three arbitrary calibration poses of the applied mirror are denoted as  $i, j, k$ .  $e$  is obtained based on Eq. (6.19).

$$\begin{cases} (R'_i - R'_j)^T \cdot e_{ij} = 0 \\ (R'_j - R'_k)^T \cdot e_{jk} = 0 \\ (R'_i - R'_k)^T \cdot e_{ik} = 0 \end{cases} \quad (6.19)$$

$d$  and  $t$  can be solved by the following equation:

$$\begin{bmatrix} (I - n_i n_i^T) 2n_i & 0 & 0 \\ (I - n_j n_j^T) & 0 & 2n_j \\ (I - n_k n_k^T) & 0 & 0 & 2n_k \end{bmatrix} \begin{bmatrix} t \\ d_i \\ d_j \\ d_k \end{bmatrix} = \begin{bmatrix} t'_i \\ t'_j \\ t'_k \end{bmatrix} \quad (6.20)$$

where  $I$  is a 3x3 identity matrix. With the purpose of evaluating the calculated camera imaging parameter and systemic geometrical parameters, an equation is applied as following:

$$\Delta m = \hat{m}(A, R, t, n, d, M) - m \quad (6.21)$$

where  $\hat{m}$  is the recalculated camera pixel based on the obtained  $M, n, d, A, R, t$ . Deviation between  $m$  and  $\hat{m}$  is denoted as  $\Delta m$ . During the movement of the search window, a series of  $\Delta m$  can be obtained and the calibration results which achieves the minimum  $\Delta m$  are used as the input initial value to conduct the following iterative optimization calculation. Fig. 6.13 summarizes the process of the studied calibration technique.

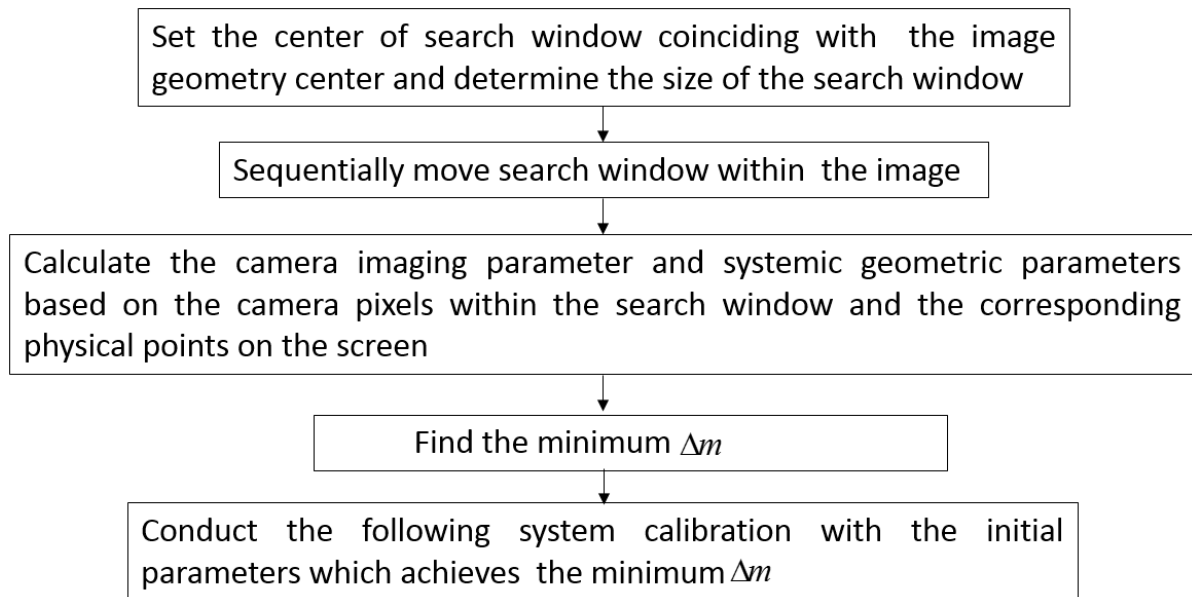


**Figure 6.12** The flowchart of the studied calibration technique.

### 6.2.2 Experiment and results

A stereo deflectometry system is used to test the studied calibration technique, as shown in Fig. 6.13. Two CCD sensors with model Lw235M from Lumenera (<https://www.lumenera.com/>) are used as the cameras in the stereo deflectometry system. The resolution of the sensor is 1616×1216 pixels. Camera lens with 35 mm fixed focal length from Navitar (<https://navitar.com/>) is installed on the sensors. The model of the camera lens is MVL35M23. Under the control of Display Duet (<https://www.duetdisplay.com/>), an iPad Pro (<https://www.apple.com/ipad-pro/>) with size of 12.9 inch is used to display fringe patterns.

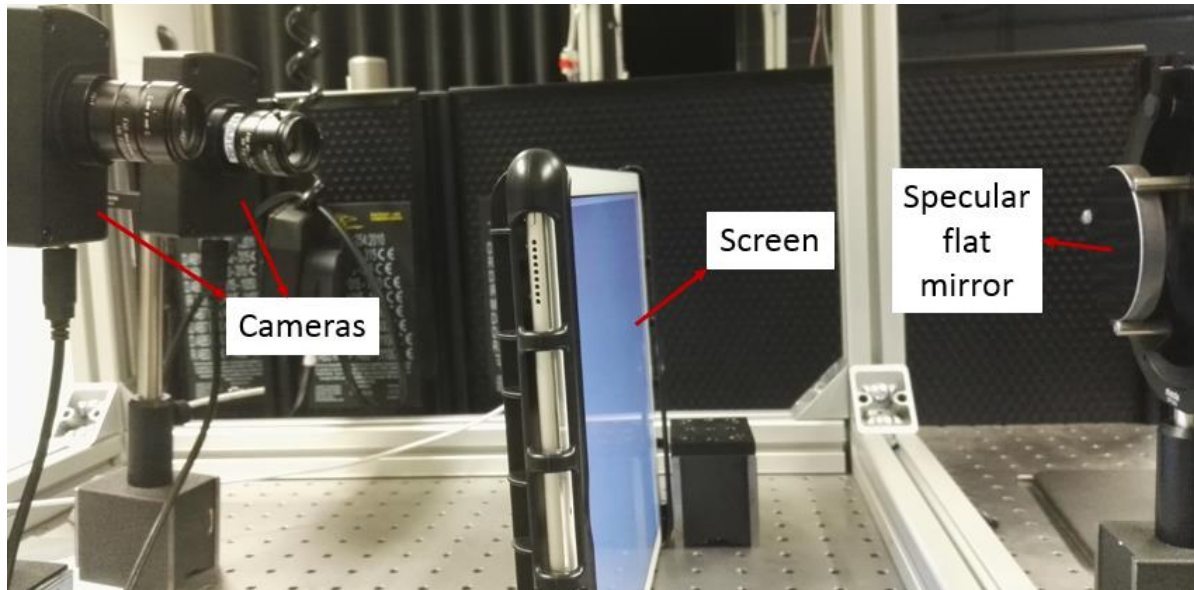


**Figure 6.13** The tested stereo deflectometry system.

Firstly, an experiment was conducted to determine the size of search window. A window is located at the camera image centre. The pixels within the window are used to calculate the reprojection deviation  $p$  based on Eqs. (6.13)-(6.14). A series of  $p$  can be obtained with half of the window size varying from 550 pixels to 50 pixels in increments of 50 pixels. Fig. 6.14 demonstrates the RMS of  $p$  and the results demonstrate that  $p$  decreases dramatically with decreasing  $d$  because of the influence of image distortion.  $\lambda$  calculated based on Eq. (6.15) is demonstrated in Fig. 6.15. It is obvious that  $\lambda$  decrease to less than 1.05 when  $2d$  is 400 pixels. Therefore,  $d$  of the search window is decided to be 200 pixels.

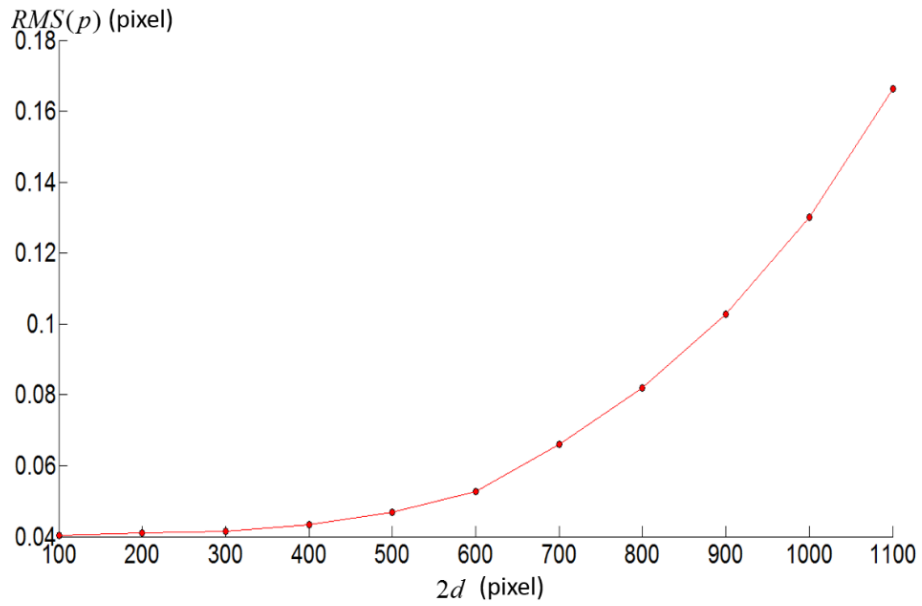


**Figure 6.14** Relation between  $RMS(p)$  and  $2d$  .

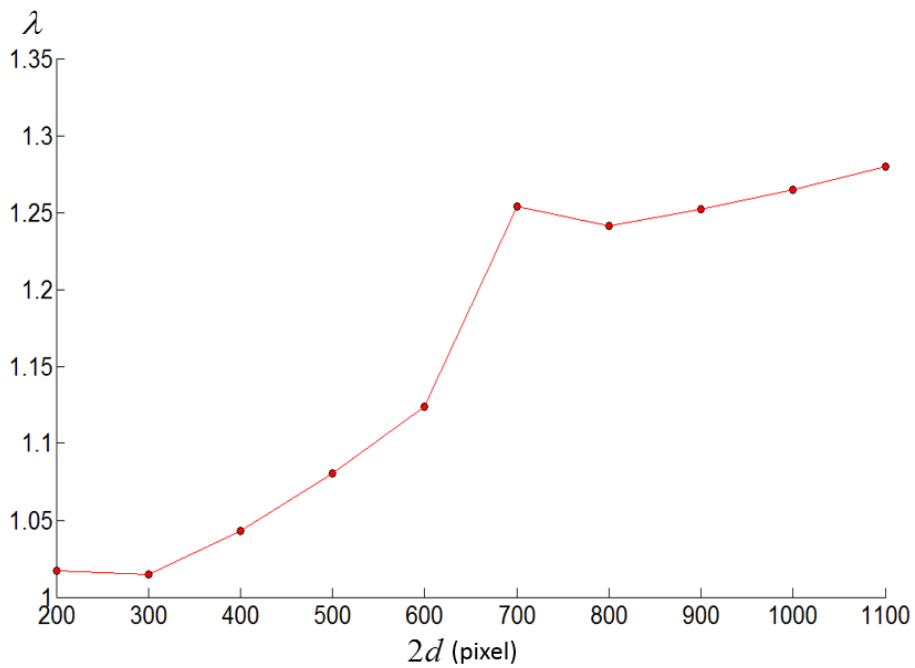


**Figure 6.15** Relation between  $\lambda$  and  $2d$  .

In order to verify the proposed algorithm, a comparison is conducted by using a calibration method with the proposed algorithm and a calibration method without the proposed algorithm. The initial values obtained based on the two calibration methods are compared first as shown in Fig. 6.16. Fig. 6.16 (a) shows the  $\Delta m$  obtained without the proposed calibration method. Because the

influence of image distortion, there are serious calibration errors. By using the proposed algorithm, the minimum  $\Delta m$  shown in Fig. 6.16(b) can be obtained with the search window moving within the camera image. The RMS of  $\Delta m$  of the two calibration results are compared in Fig. 6.17. It is obvious that the proposed method improves the accuracy of initial value significantly. Based on the calculated initial values, the final calibration results can be obtained through iterative optimization algorithm. Fig. 6.18 (a) shows the final calibration result calculated based on the initial value obtained without the studied calibration technique. In contrast, Fig. 6.18 (b) shows the final calibration result calculated based on the initial value obtained with the studied calibration technique. The RMS of the final calibration error are compared in Fig. 6.19. It is obvious that the final calibration result obtained based on the proposed method is more accurate than the calibration result without the proposed method. The comparative experiment demonstrates the proposed algorithm can effectively enhance the robustness of the systemic calibration of stereo deflectometry.

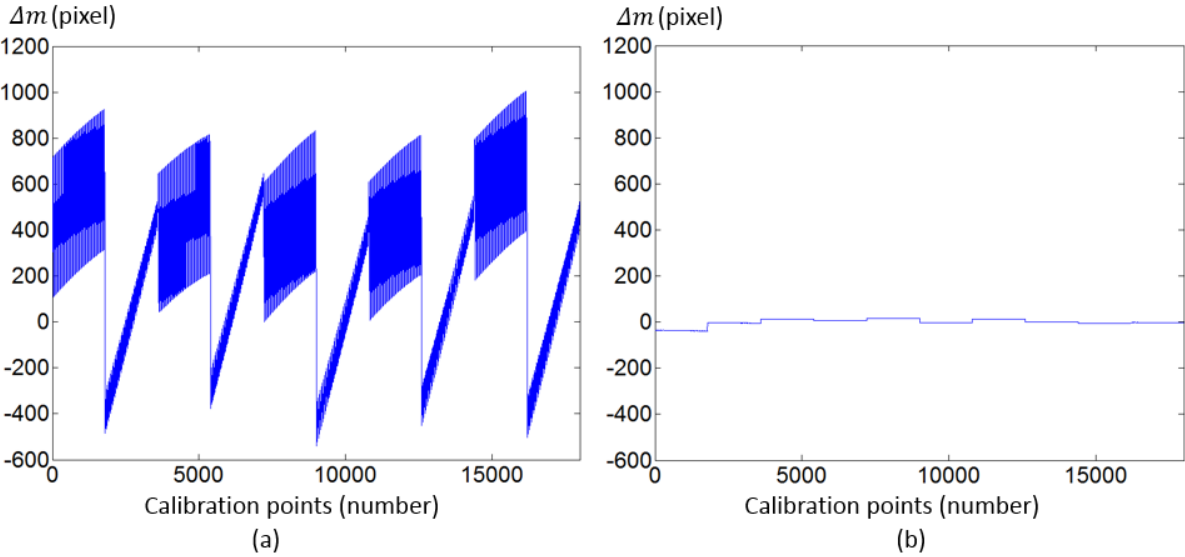


**Figure 6.16 Comparison of accuracy of initial value calculation. (a) Without the proposed calibration method; (b) with the proposed calibration method.**

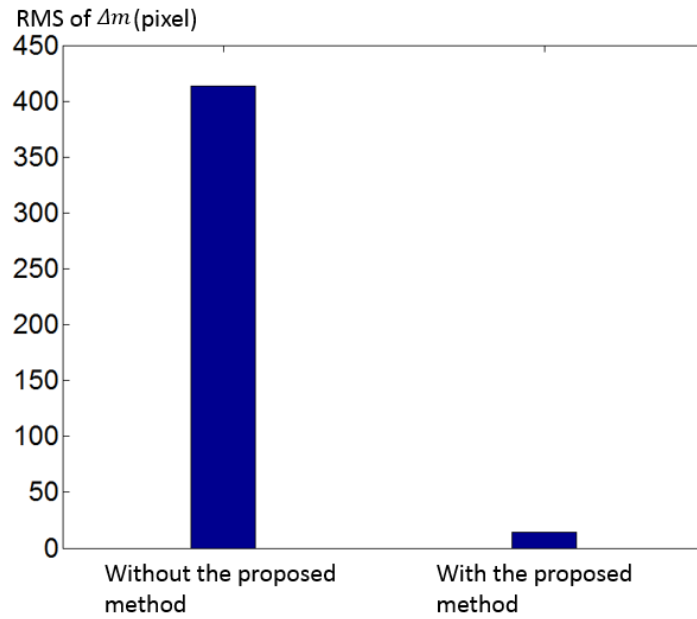


**Figure 6.17** RMS of  $\Delta m$ .

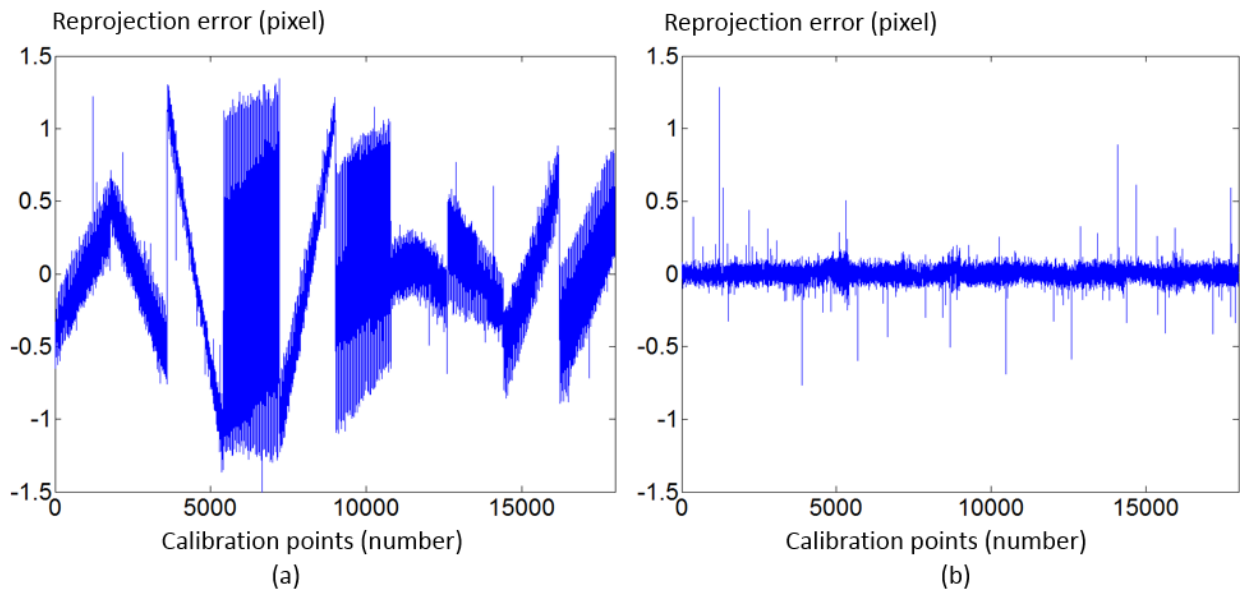


**Figure 6.18** Calibration error. (a) Based on the initial value obtained without the studied calibration technique; (b) based on the initial value obtained with the studied calibration technique.

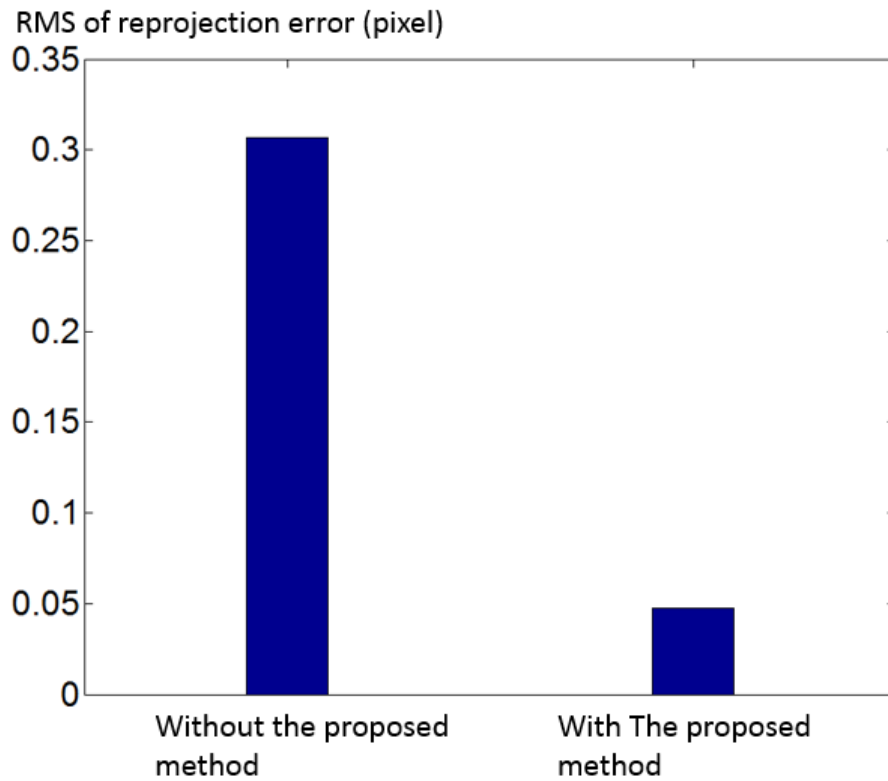


**Figure 6.19 RMS of calibration error.**

A comparison by measuring a concave mirror with  $\lambda/8$  surface accuracy was conducted based on the above calibration results. The concave mirror is from Edmund (<https://www.edmundoptics.com/>) with a stock number of 40-913. Measurement results of the test mirror is shown in Fig. 6.20. Fig. 6.20(a) shows measurement result obtained without the proposed calibration method. PV of the measurement error is 1.2  $\mu\text{m}$ . In contrast, the PV of the measurement error calculated with the studied calibration technique is 0.096  $\mu\text{m}$ , as shown in Fig. 6.20(b). It is obvious that the measurement result calculated with the studied calibration technique is more accurate than the measurement result calculated without the proposed method.

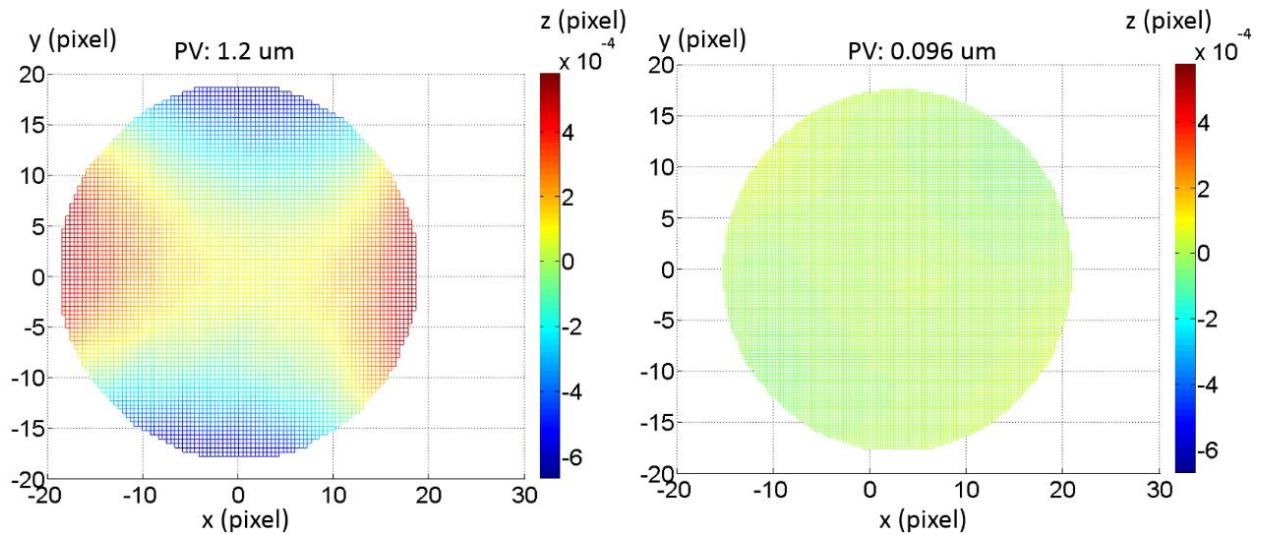


**Figure 6.20 Comparison of measurement results. (a) Measurement result without the studied calibration technique; (b) measurement result with the studied calibration technique.**

### 6.3 Summary

Systemic calibration plays an important role in the improvement of measurement accuracy of stereo deflectometry. This chapter studied a holistic systemic calibration technique for stereo deflectometry to increase the measurement accuracy of the system. By applying an iterative distortion compensation algorithm, the studied calibration method can significantly enhance the calibration accuracy. The flexibility and accuracy of the studied calibration technique have been tested by simulation and experimental results. In comparison of the measurement results of an optical flat, the PV of measurement error of the studied calibration technique is 69.7 nm, which is about four times better than traditional calibration method.

With the purpose of improving the accuracy and robustness of stereo deflectometry's calibration, a calibration method based on a search algorithm with an evaluation function is also researched in this chapter. Experimental results proved that the studied calibration technique could effectively enhance stereo deflectometry's calibration accuracy and measurement accuracy.

## 7. Analysis of phase error influence

A novel analysis method for stereo deflectometry is represented in this chapter to increase measurement accuracy of the system. With the purpose of studying the relation between gradient ambiguity and phase ambiguity in stereo deflectometry, an imaging mathematical model is investigated. Based on this model, the optimized pixel size of fringe-displaying screen and fringe's period on the screen are researched. Works in this chapter generated one journal paper ([Xu, Gao et al. 2018](#)).

### 7.1 Principle of the analysis method

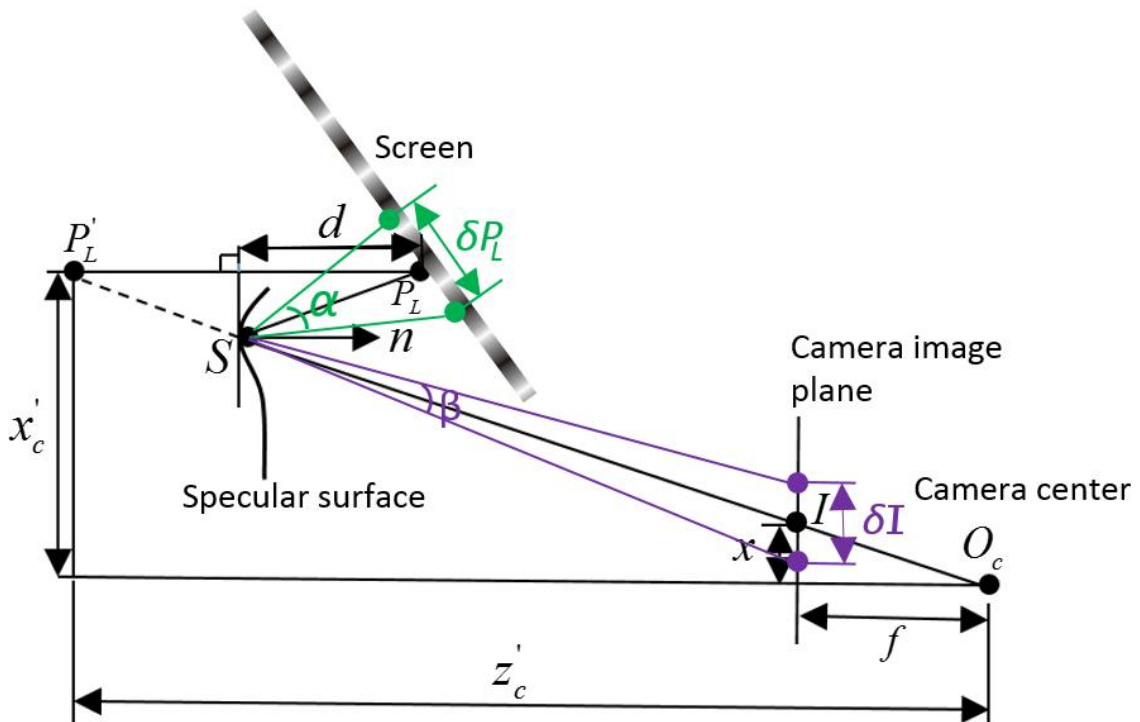


Figure 7.1 The studied mathematical model for stereo deflectometry.

Because stereo deflectometry reconstructs the measured surface based on gradient data and phase data, the accuracy of gradient and phase play an important role in measurement accuracy of the system. With the purpose of analysing influence of gradient and phase, an imaging model is investigated as shown in Fig. 7.1.  $P_L$  represents a point on fringe-displaying screen. The image of  $P_L$  via specular surface's reflection is denoted as  $P'_L$ . A camera with an optical centre of  $O_c$  captures  $P'_L$ . The intersection of the measured surface and  $O_c P'_L$  is expressed with  $S$ .  $d$  represents

the distance between the tangent plane of  $S$  and  $P_L$ . The intersection of image plane and  $O_c P_L'$  is  $I$ . Defining  $n$  as the normal of  $S$ . Based on a triangle composed of  $I$ ,  $S$  and  $P_L$ ,  $n$  can be obtained. Using  $\delta I$  and  $\delta P_L$  represent the ambiguity of  $I$  and  $P_L$ . It is obvious that gradient calculation is influenced by  $\delta I$  and  $\delta P_L$ .  $\delta P_L$  leads to a gradient ambiguity  $\alpha$  as the green colour shown in Fig. 7.1.  $\delta I$  results in a gradient ambiguity  $\beta$  as the purple colour shown in Fig. 7.1. Defining  $\varphi_x$  represents the horizontal phase value of  $P_L$  and  $\varphi_y$  represents the vertical phase value of  $P_L$ . The physical location of  $P_L$  on fringe-displaying screen is denoted as  $(x_w, y_w)$ . Eq. (8.1) is used to calculate the relationship between  $(x_w, y_w)$  and  $(\varphi_x, \varphi_y)$ .

$$\begin{cases} x_w = (n_p \cdot p / 2\pi) \cdot \varphi_x \\ y_w = (n_p \cdot p / 2\pi) \cdot \varphi_y \end{cases} \quad (7.1)$$

where  $n_p$  represents pixel number of the displayed fringe per period. Screen pixel size is denoted as  $p$ . Defining  $(x_c, y_c, z_c)$  as the coordinate of  $P_L$  in terms of camera coordinate system. Eq. (7.2) is applied to calculate  $(x_c, y_c, z_c)$ .

$$\begin{cases} x_c = f_x(x_w, y_w) \\ y_c = f_y(x_w, y_w) \\ z_c = f_z(x_w, y_w) \end{cases} \quad (7.2)$$

where  $f_x$ ,  $f_y$  and  $f_z$  are the transformation from screen coordinate system to camera coordinate system along  $x$ ,  $y$  and  $z$  direction.  $f_x$ ,  $f_y$  and  $f_z$  are only influenced by the definition of camera coordinate system and system coordinate system. Defining  $(x'_c, y'_c, z'_c)$  as the coordinate of  $P_L'$  in terms of camera coordinate system.  $(x'_c, y'_c, z'_c)$  are calculated based on Eq. (7.3).

$$\begin{cases} x'_c = g_x(x_c, y_c, z_c) \\ y'_c = g_y(x_c, y_c, z_c) \\ z'_c = g_z(x_c, y_c, z_c) \end{cases} \quad (7.3)$$

where  $g_x$ ,  $g_y$  and  $g_z$  are the transformation from camera coordinate system to mirrored screen coordinate system along  $x$ ,  $y$  and  $z$  direction. Only  $d$  and  $n$  can affect  $g_x$ ,  $g_y$  and  $g_z$ .

Defining  $(x, y)$  as the location of  $l$  in terms of camera coordinate system. Eq. (7.4) is used to calculate  $(x, y)$ .

$$\begin{cases} x = \frac{f}{z_c} x'_c \\ y = \frac{f}{z_c} y'_c \end{cases} \quad (7.4)$$

where  $f$  is focal length of the camera. Defining  $(u, v)$  as the location of  $l$  in terms of camera pixel coordinate system.  $(u, v)$  is calculated according to Eq. (7.5).

$$\begin{cases} u = \frac{x}{d_x} + u_0 \\ v = \frac{y}{d_y} + v_0 \end{cases} \quad (7.5)$$

where  $u_0$  and  $v_0$  represent the location of original point in terms of camera pixel coordinate along  $u$  and  $v$  direction respectively. The coefficient between physical length and camera pixel are expressed as  $d_x$  along  $u$  and  $d_y$  along  $v$  direction. Defining  $\delta x_w$  as the location ambiguity of  $P_L$  along  $x$  direction and  $\delta y_w$  as the location ambiguity of  $P_L$  along  $y$  direction. Phase ambiguity of  $P_L$  along  $x$  direction and  $y$  direction are denoted as  $\delta\phi_x$  and  $\delta\phi_y$ . Eq. (7.6) is used to express the relation between  $(\delta\phi_x, \delta\phi_y)$  and  $(\delta x_w, \delta y_w)$ .

$$\begin{cases} \delta x_w = \frac{n_p P}{2\pi} \cdot \delta\phi_x \\ \delta y_w = \frac{n_p P}{2\pi} \cdot \delta\phi_y \end{cases} \quad (7.6)$$

Because  $\delta\phi_x$  equals  $\delta\phi_y$ , Eq. (7.7) can be obtained by replace  $\delta\phi_x$  and  $\delta\phi_y$  in Eq. (8.6) with  $\delta\phi$ .

$$\begin{cases} \delta x_w = \frac{n_p P}{2\pi} \cdot \delta\phi \\ \delta y_w = \frac{n_p P}{2\pi} \cdot \delta\phi \end{cases} \quad (7.7)$$

Positioning ambiguity of  $l$  are denoted as  $\delta u$  along  $u$  direction and  $\delta v$  along  $v$  direction. Based on Eq. (7.1) - Eq. (7.5), the relationship between  $(\delta u, \delta v)$  and  $(\delta\phi_x, \delta\phi_y)$  can be deduced as shown in Eq. (7.8).

$$\begin{cases} \delta u = n_p p \cdot |C_1 + C_2| \cdot \delta\phi \\ \delta v = n_p p \cdot |C_3 + C_4| \cdot \delta\phi \end{cases} \quad (7.8)$$

where  $C_1$ ,  $C_2$ ,  $C_3$  and  $C_4$  are obtained from Eq. (7.9).  $C_1$ ,  $C_2$ ,  $C_3$  and  $C_4$  are not affected by the parameters of fringe-displaying screen.

$$\begin{cases} C_1 = \frac{f}{2\pi d_x z_c^2} (C_{11} + C_{12}) \\ C_2 = \frac{f}{2\pi d_x z_c^2} (C_{21} + C_{22}) \\ C_3 = \frac{f}{2\pi d_y z_c^2} (C_{31} + C_{32}) \\ C_4 = \frac{f}{2\pi d_y z_c^2} (C_{41} + C_{42}) \\ C_{11} = z_c \left[ \frac{\partial g_x(x_c, y_c, z_c)}{\partial x_c} \cdot \frac{\partial f_x(x_w, y_w)}{\partial x_w} + \frac{\partial g_x(x_c, y_c, z_c)}{\partial y_c} \cdot \frac{\partial f_y(x_w, y_w)}{\partial x_w} + \frac{\partial g_x(x_c, y_c, z_c)}{\partial z_c} \cdot \frac{\partial f_z(x_w, y_w)}{\partial x_w} \right] \\ C_{12} = -x_c \left[ \frac{\partial g_z(x_c, y_c, z_c)}{\partial x_c} \cdot \frac{\partial f_x(x_w, y_w)}{\partial x_w} + \frac{\partial g_z(x_c, y_c, z_c)}{\partial y_c} \cdot \frac{\partial f_y(x_w, y_w)}{\partial x_w} + \frac{\partial g_z(x_c, y_c, z_c)}{\partial z_c} \cdot \frac{\partial f_z(x_w, y_w)}{\partial x_w} \right] \\ C_{21} = z_c \left[ \frac{\partial g_x(x_c, y_c, z_c)}{\partial x_c} \cdot \frac{\partial f_x(x_w, y_w)}{\partial y_w} + \frac{\partial g_x(x_c, y_c, z_c)}{\partial y_c} \cdot \frac{\partial f_y(x_w, y_w)}{\partial y_w} + \frac{\partial g_x(x_c, y_c, z_c)}{\partial z_c} \cdot \frac{\partial f_z(x_w, y_w)}{\partial y_w} \right] \\ C_{22} = -x_c \left[ \frac{\partial g_z(x_c, y_c, z_c)}{\partial x_c} \cdot \frac{\partial f_x(x_w, y_w)}{\partial y_w} + \frac{\partial g_z(x_c, y_c, z_c)}{\partial y_c} \cdot \frac{\partial f_y(x_w, y_w)}{\partial y_w} + \frac{\partial g_z(x_c, y_c, z_c)}{\partial z_c} \cdot \frac{\partial f_z(x_w, y_w)}{\partial y_w} \right] \\ C_{31} = z_c \left[ \frac{\partial g_y(x_c, y_c, z_c)}{\partial x_c} \cdot \frac{\partial f_x(x_w, y_w)}{\partial x_w} + \frac{\partial g_y(x_c, y_c, z_c)}{\partial y_c} \cdot \frac{\partial f_y(x_w, y_w)}{\partial x_w} + \frac{\partial g_y(x_c, y_c, z_c)}{\partial z_c} \cdot \frac{\partial f_z(x_w, y_w)}{\partial x_w} \right] \\ C_{32} = -y_c \left[ \frac{\partial g_z(x_c, y_c, z_c)}{\partial x_c} \cdot \frac{\partial f_x(x_w, y_w)}{\partial x_w} + \frac{\partial g_z(x_c, y_c, z_c)}{\partial y_c} \cdot \frac{\partial f_y(x_w, y_w)}{\partial x_w} + \frac{\partial g_z(x_c, y_c, z_c)}{\partial z_c} \cdot \frac{\partial f_z(x_w, y_w)}{\partial x_w} \right] \\ C_{41} = z_c \left[ \frac{\partial g_y(x_c, y_c, z_c)}{\partial x_c} \cdot \frac{\partial f_x(x_w, y_w)}{\partial y_w} + \frac{\partial g_y(x_c, y_c, z_c)}{\partial y_c} \cdot \frac{\partial f_y(x_w, y_w)}{\partial y_w} + \frac{\partial g_y(x_c, y_c, z_c)}{\partial z_c} \cdot \frac{\partial f_z(x_w, y_w)}{\partial y_w} \right] \\ C_{42} = -y_c \left[ \frac{\partial g_z(x_c, y_c, z_c)}{\partial x_c} \cdot \frac{\partial f_x(x_w, y_w)}{\partial y_w} + \frac{\partial g_z(x_c, y_c, z_c)}{\partial y_c} \cdot \frac{\partial f_y(x_w, y_w)}{\partial y_w} + \frac{\partial g_z(x_c, y_c, z_c)}{\partial z_c} \cdot \frac{\partial f_z(x_w, y_w)}{\partial y_w} \right] \end{cases} \quad (7.9)$$

Eq. (7.10) can be deduced from Eq. (7.7) and Eq. (7.8) to calculate  $\delta P_L$  and  $\delta I$ .

$$\begin{cases} \delta P_L = \frac{n_p p}{\sqrt{2\pi}} \cdot \delta\phi \\ \delta I = n_p p \cdot \sqrt{|C_1 + C_2|^2 + |C_3 + C_4|^2} \cdot \delta\phi \end{cases} \quad (7.10)$$

Defining  $d_c$  represents the length of  $IS$ . The length of  $P_L S$  is denoted as  $d_L$ .  $\alpha$  and  $\beta$  can be obtained based on Eq. (7.11) under the fact that  $\delta I$  is much smaller than  $\delta I$  and  $\delta P_L$  is much smaller than  $d_L$ .

$$\begin{cases} \alpha = \frac{\delta P_L}{d_L} \\ \beta = \frac{\delta I}{d_c} \end{cases} \quad (7.11)$$

Defining  $\delta\theta$  represents the overall gradient ambiguity of  $S$ . the normal of  $S$  equals  $(\alpha + \beta) / 2$ . Eq. (7.11) is deduced to reflect the relation between  $\delta\theta$  and  $\delta\varphi$  based on Eq. (7.10) - Eq. (7.11).

$$\delta\theta = \frac{n_p p}{2} \cdot \left( \frac{1}{\sqrt{2\pi}d_L} + \frac{\sqrt{|C_1 + C_2|^2 + |C_3 + C_4|^2}}{d_c} \right) \cdot \delta\varphi \quad (7.12)$$

With the purpose of increasing gradient calculation accuracy, two methods can be investigated based on Eq. (7.12). Decreasing phase ambiguity is one of the methods. Reducing the coefficient between gradient ambiguity and phase ambiguity is another method. Because  $C_1, C_2, C_3, C_4, d_L$  and  $d_c$  are influenced by both camera's characteristic and the curvature of the surface under test, the influence of  $C_1, C_2, C_3, C_4, d_L$  and  $d_c$  is hard to be analysed. Consequently, this chapter only investigates the influence of  $p$  and  $n_p$  on measurement accuracy.

When the screen is displaying fringe patterns, pixels of the screen samples continuous sinusoidal fringe patterns. The screen's sampling error introduces a large portion of phase ambiguity. Based on the knowledge that increasing sampling frequency can increase the reducibility of original signal, phase ambiguity introduced by screen's sampling error can be reduced by increasing  $n_p$ . On the other hand, increasing  $n_p$  will enlarge the coefficient between gradient ambiguity and phase ambiguity. The enlargement of the coefficient decrease measurement accuracy of the measurement system.

Now we discuss the influence of  $p$ . Decreasing  $p$  can decrease the coefficient between gradient ambiguity and phase ambiguity, which is helpful to enhance the system's measurement accuracy. Common LCD screen with pixel size of around 0.3 mm is used in conventional stereo deflectometry system ([Petz and Tutsch 2005](#), [Ren, Gao et al. 2015](#), [Huang, Xue et al. 2016](#)). Apple (<https://www.apple.com/>) investigates Retina Display technique that having much smaller pixel size (around 0.096 mm) comparing with conventional LCD screen. Consequently, comparison

between Retina Display screen and conventional LCD screen were conducted to test the above investigation.

## 7.2 Experiments and results

With the purpose of verifying the impact of  $n_p$  on gradient ambiguity and phase ambiguity, an experiment is conducted with a common LCD screen. The model of the LCD is Dell E151Fpp. The LCD consists of 1024×768 pixels. The size of each LCD pixel is 0.297 mm. A CCD sensor is used to capture the fringe patterns displayed on the LCD. The sensor is a Lumenera (<https://www.lumenera.com/>) camera with model number Lw235M. The resolution of the camera is 1616×1216 pixels. In order to investigate the influence of  $n_p$  on phase error, 6 absolute phase maps were acquired by increasing  $n_p$  from 6 pixels to 16 pixels in increments of 2 pixels. The relation between  $n_p$  and phase error was calculated based on the phase maps as shown in Fig. 7.2. When  $n_p$  increase from 6 pixels to 8 pixels, phase error decreases significantly. The descent trend of phase error become less obvious after  $n_p$  exceeds 8 pixels.

In order to study the influence of  $n_p$  on gradient calculation error, the relation between gradient calculation error and  $n_p$  is obtained, as shown in Fig. 7.3. The gradient error can be calculated by using the known phase error and  $n_p$  according to Eq. (7.12). Gradient error touches the bottom when  $n_p$  is 8 pixels. After  $n_p$  exceeds 8 pixels, gradient error increases. The reason for this trend is because  $n_p$  impacts gradient ambiguity by influencing gradient ambiguity coefficient on one hand. On the other hand,  $n_p$  affects gradient ambiguity by influencing screen's sampling error. In a word, with the purpose of decreasing stereo deflectometry's gradient ambiguity,  $n_p$  should equals 8 pixels.

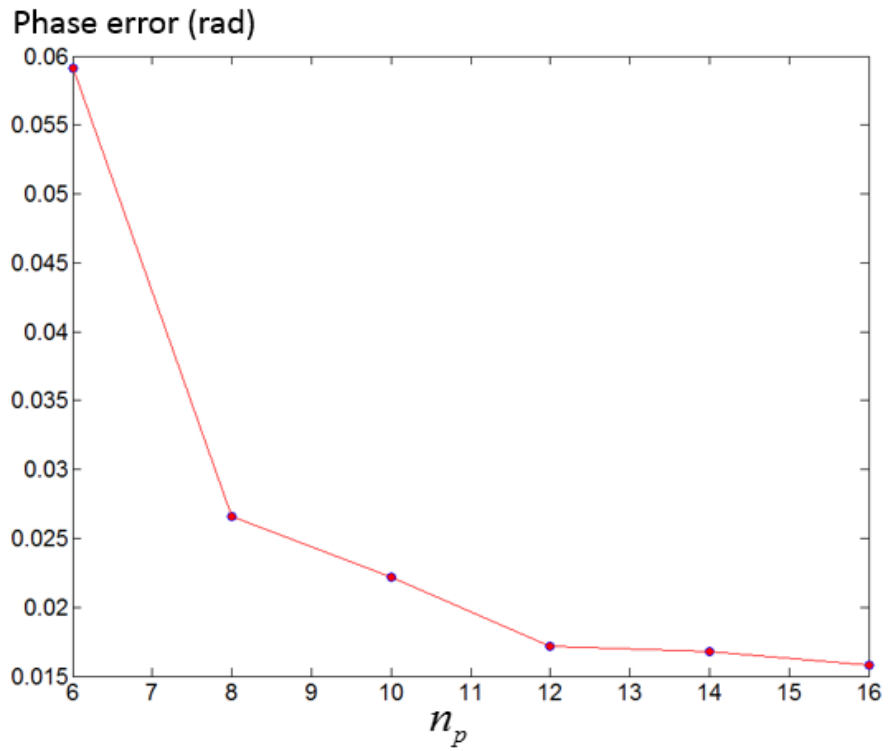


**Figure 7.2** The relation between  $n_p$  and phase error.

The ratio of normal error under different  $n_p$  to the normal error when  $n_p$  is 8

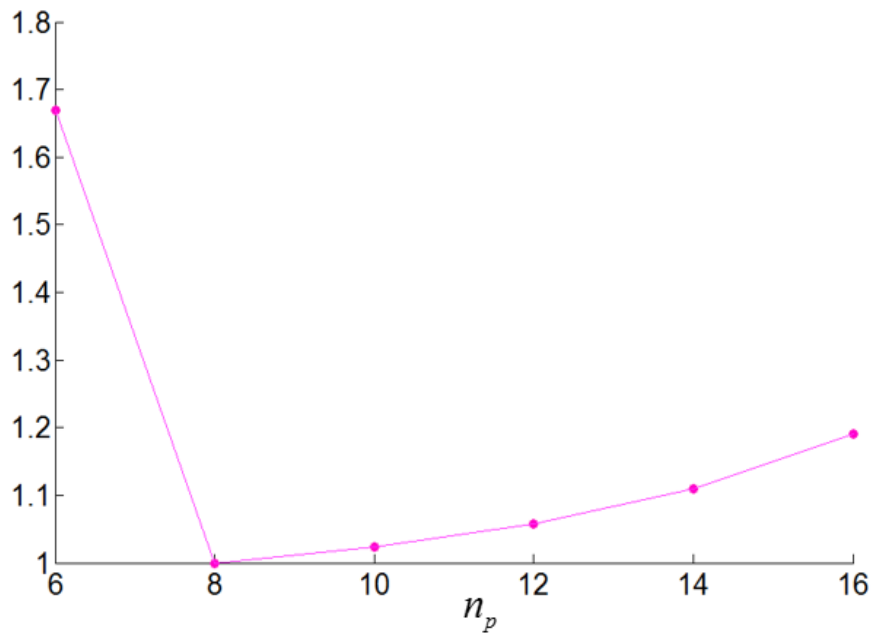


**Figure 7.3** The variation of gradient error.

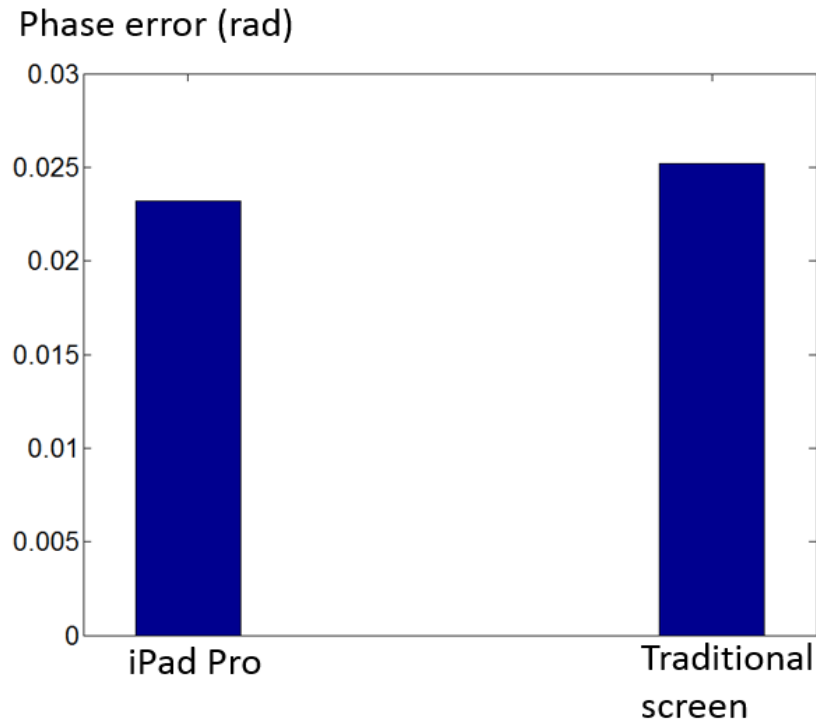


**Figure 7.4 Phase error of iPad Pro and traditional screen.**

iPad Pro (<https://www.apple.com/uk/ipad-pro/>) is a screen based on Retina Display technique, which has smaller pixel size than traditional screen. In order to test the phase error difference of iPad Pro and the traditional screen. An experiment was conducted to compare phase error of the two types of screen. The phase error was calculated under  $n_p$  equalling 8 pixels. The experimental results is shown in Figure 7.4. iPad Pro's phase error is 0.023 rad while tradition screen's phase error is 0.025 rad. The experimental results demonstrate the influence of the two screen on phase error are very close.

A stereo deflectometry system was simulated to test the impact of  $p$ . Fig. 7.5 shows the simulated system which contains two sensors and a fringe-displaying screen. Based on the experimental result of Fig. 7.4, phase noise randomly varying within 0.025 rad was added into the simulated phase maps. In an actual measurement process, iPad Pro need to work under the control of Duet Display (<https://www.duetdisplay.com/>) to display fringe patterns generated by a computer. In this case, the equivalent pixel size of iPad Pro is 0.128 mm rather than its original pixel size 0.096 mm. Consequently, two measurement result were obtained based on the simulated stereo deflectometry system. To simulate the iPad Pro's pixel size and traditional screen's pixel size. One measurement

result is obtained when  $p$  equals 0.297 mm. The other measurement result is calculated when  $p$  equals 0.128 mm. Fig. 7.6 shows the measurement results. When  $p$  equals 0.297 mm, PV of the obtained measurement error is 53.7 nm as shown in Fig. 7.6(a). In contrast, PV of the obtained measurement error is 22.6 nm when  $p$  equals 0.128 mm as shown in Fig. 7.6(b). The reason for the experimental results is because decreasing of  $p$  can decrease the coefficient between the gradient ambiguity and phase ambiguity.

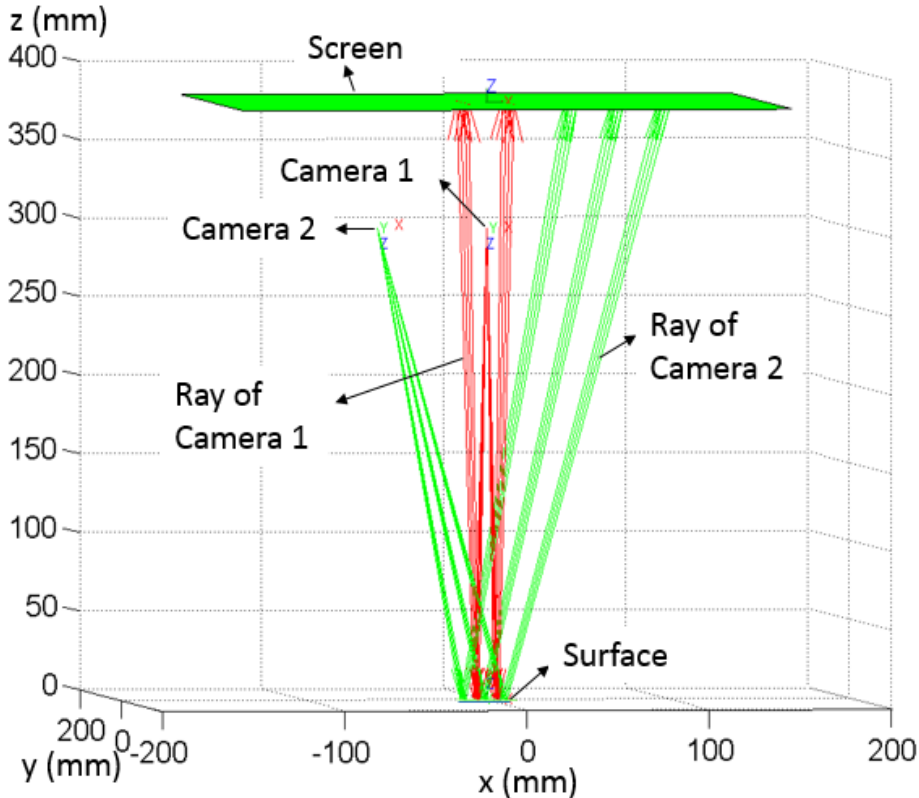
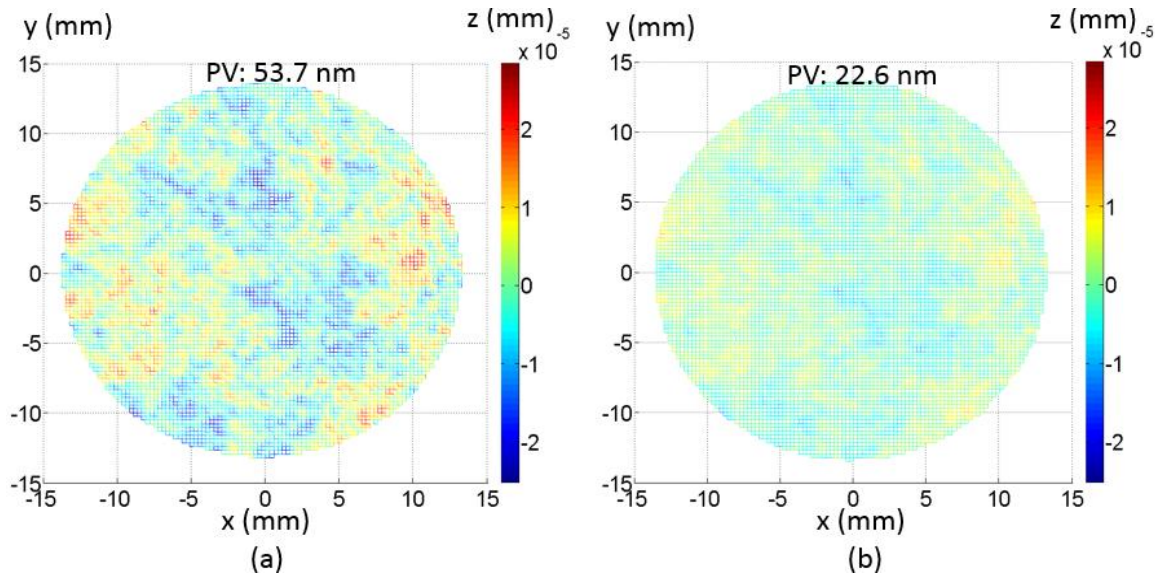


Figure 7.5 The simulation setup.



**Figure 7.6 Measurement result. (a) Measurement result obtained when  $P$  equals 0.297 mm; (b) measurement result obtained when  $p$  equals 0.128 mm.**

### 7.3 Summary

With the purpose of improving stereo deflectometry's measurement accuracy, this chapter investigate a mathematical model to studied the influence of phase ambiguity and gradient ambiguity in stereo deflectometry. Pixel size of fringe-displaying screen and the occupied LCD pixels per fringe period are researched through systematically analysing their influence on phase ambiguity and gradient ambiguity. Experimental results confirm the analysis described in this chapter could considerably increase stereo deflectometry's measurement accuracy.

## 8. Analysis of geometric parameters influence

This chapter presents a novel analysis of the geometric parameters of stereo deflectometry system to improve the system measurement accuracy. Reconstruction result of stereo deflectometry is integrated with the calculated normal data of the measured surface. Geometric parameters of the stereo deflectometry system affect the measurement accuracy by affecting the calculation accuracy of the normal data. In this chapter, four geometric parameters of stereo deflectometry system are analyzed, including the distance between main camera and the measured object surface, the angle between main camera ray and surface normal, the distance between the fringe displaying screen and object and the angle between main camera and reference camera. The influence of the geometric parameters to the measurement accuracy are researched. Experiments are performed using simulated and actual data and the results confirm the effects of these four parameters on the measurement results. Works in this chapter generated one journal paper (Performance analysis and evaluation of geometric parameters in stereo deflectometry, accepted).

### 8.1 Principle of the analysis method of the geometric parameters

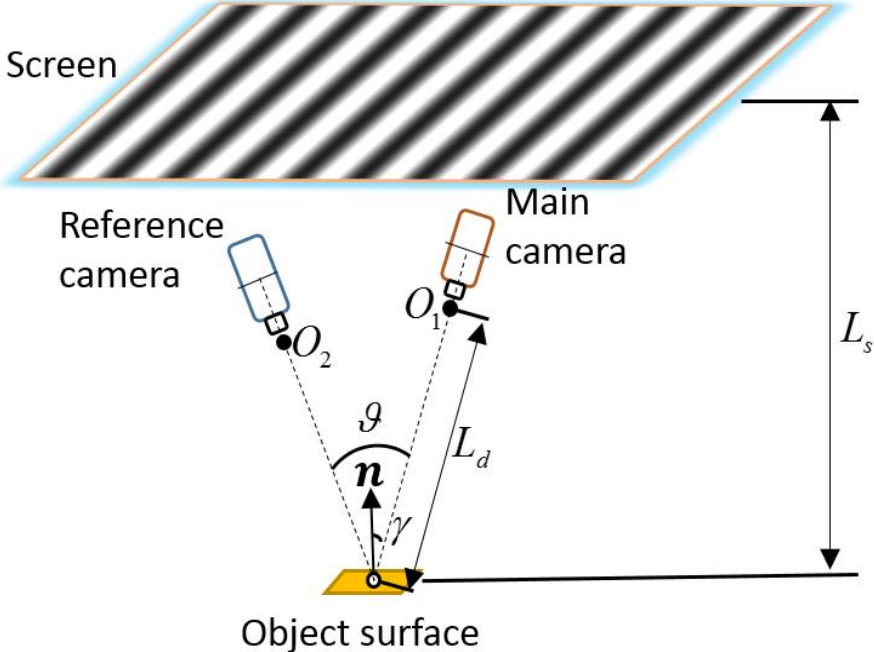
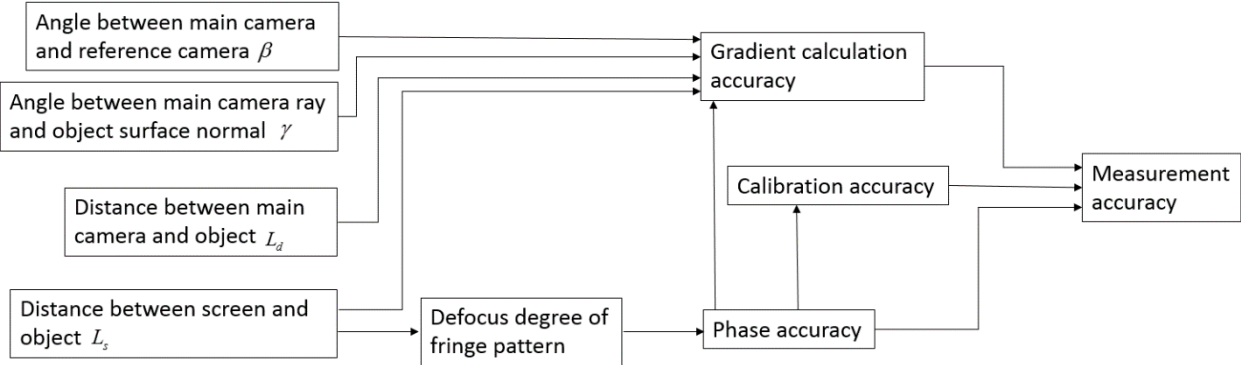


Figure 8.1 The arrangement of stereo deflectometry.

There are three principle error sources that directly affect measurement accuracy of a stereo deflectometry system: calibration error, phase error and gradient calculation error. Other error

sources impact on measurement accuracy by acting on the three error sources. Fig. 8.1 shows the arrangement of the relevant components in a stereo deflectometry system.  $L_d$  is the distance between main camera and the measured object surface.  $\gamma$  denotes the angle between main camera ray and surface normal.  $L_s$  represents the distance between fringe displaying screen and object. The angle between main camera and reference camera is denoted as  $\beta$ . The geometric parameters  $\gamma$ ,  $L_s$ ,  $L_d$ , and  $\beta$  are analysed for their influence on the three error sources and overall measurement accuracy. The four parameters are independent of each other in geometry. Fig. 8.2 shows the relationship between the geometric parameters and error sources. The arrows in this figure indicates that the factor of the arrow tail affects the error source of the arrow head. The geometric parameters affect gradient calculation accuracy independently. Though the distance between screen and object also impacts the phase accuracy through its influence on defocus degree of fringe patterns, the impact from phase accuracy is independent with the influence caused by other geometric parameters. Therefore, the influence of the geometric parameters on the measurement accuracy are not coupled. An overall flowchart to clarify the error analysis procedure is shown in Fig. 8.3. Four error models are investigated to analyse the influence of the geometric parameters. The analysis conclusions are verified through simulation and actual experiment by modifying measuring conditions. Finally, appropriate combination of geometric parameters is obtained.



**Figure 8.2 The relationship between the geometric parameters and error sources.**

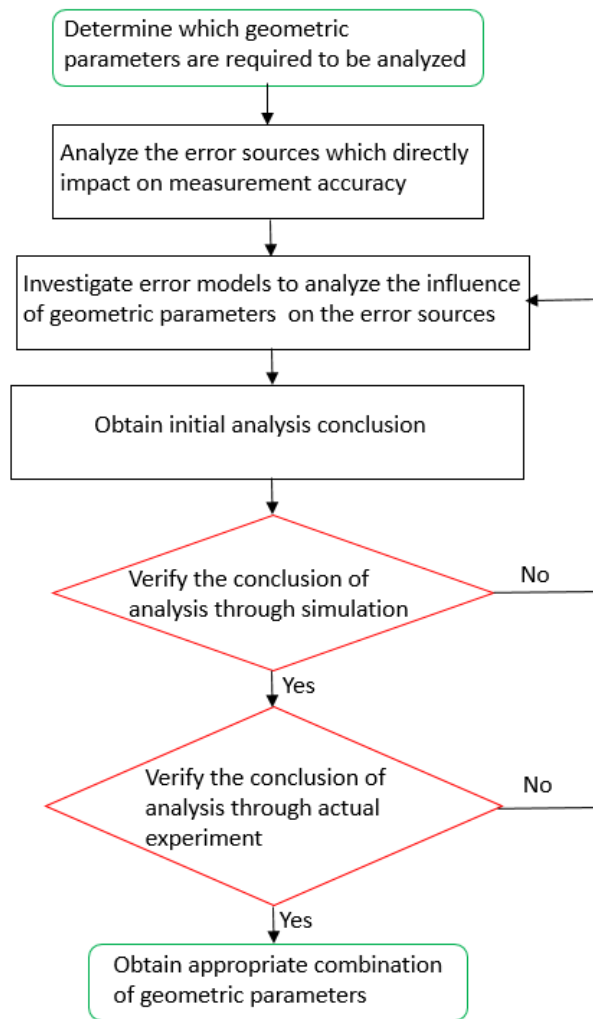


Figure 8.3 The procedures of error analysis.

### 8.1.1 Influence of $\gamma$

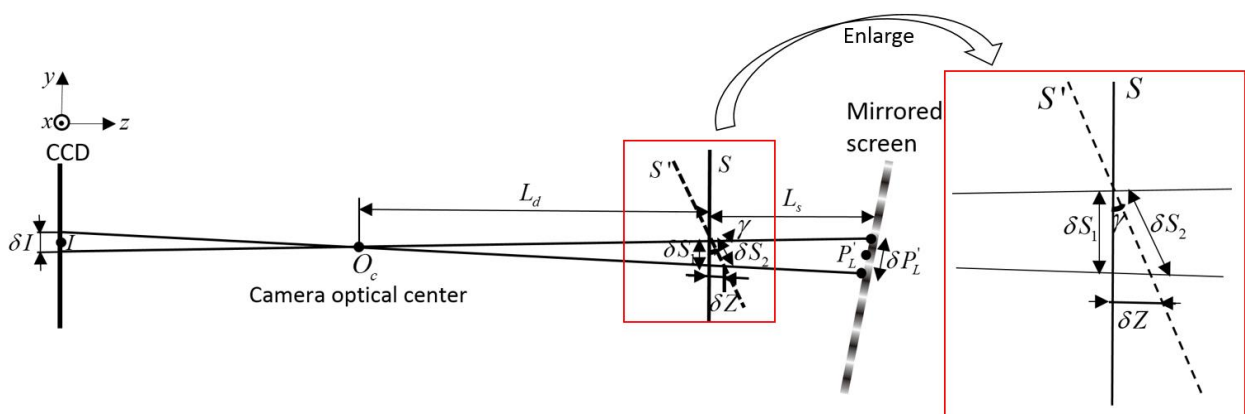


Figure 8.4 Relative positions of the imaging plane of a camera, the measured surface, and the mirrored screen.

Through the reflection of the measured surface, the image of the displaying screen can be captured directly by the camera in a deflectometry system. The relative positions of the imaging plane of the camera, the measured surface, and the mirrored screen are depicted in Fig. 8.4. Based on a pinhole model, a point  $P'_L$  on the mirror screen is captured by the camera.  $I$  is the image of  $P'_L$  on the imaging plane.  $\delta P'_L$  and  $\delta I$  denote the location uncertainty caused by phase error on the mirrored screen and imaging plane respectively. When the measured surface is located at  $S$ , the surface is perpendicular to the camera ray.  $\delta P'_L$  results in an uncertainty  $\delta S_1$  on the measured surface. In contrast, when the measured surface moves to  $S'$  where  $\gamma$  is not equal to 0, the uncertainty  $\delta S_2$  caused by  $\delta P'_L$  on the measured surface can be described as:

$$\delta S_2 = \frac{1}{\cos \gamma} \delta S_1 = \frac{1}{(1 + L_s / L_d) \cos \gamma} \delta P'_L \quad (8.1)$$

The uncertainty depth  $\delta Z$  along  $Z$  direction can be calculated as:

$$\delta Z = \frac{\tan \gamma}{(1 + L_s / L_d)} \delta P'_L \quad (8.2)$$

It is obvious that  $\delta S_2$  and  $\delta Z$  increase with increasing  $\gamma$  according to Eqs. (8.1)-(8.2).

### 8.1.2 Influence of $L_s$

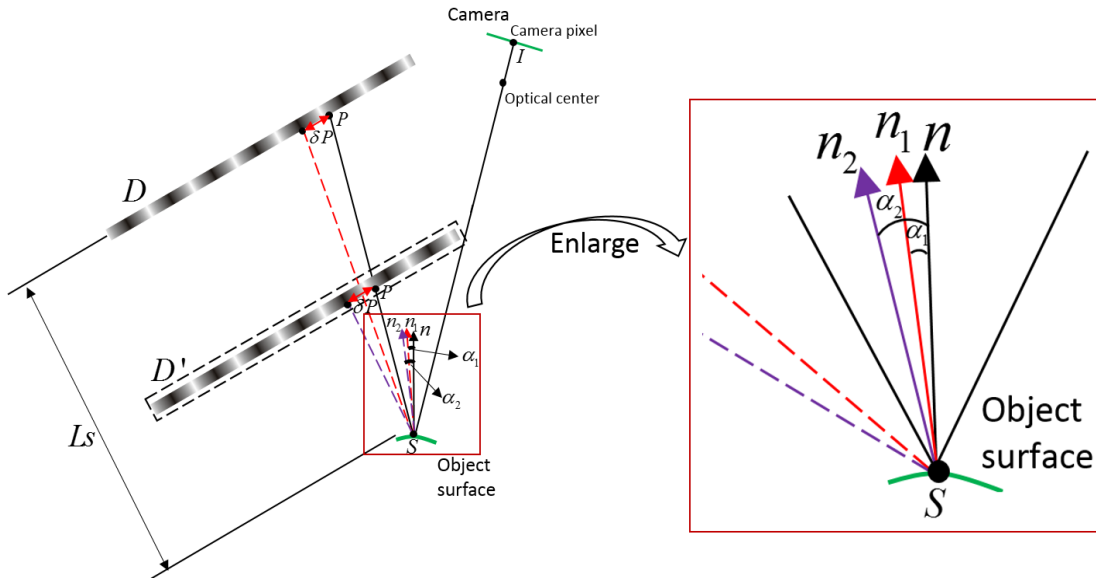


Figure 8.5 Illustration of the influence of  $L_s$ .

In order to illustrate the influence of  $L_s$ , the screen of a stereo deflectometry system is placed at  $D$  firstly and then moved to  $D'$ , as shown in Fig. 8.5.  $I$  is the image of a point  $P$  on the screen through the reflection of the measured surface. The normal  $n$  of the surface can be calculated based on incident ray  $PS$  and reflection ray  $SI$  according to the reflection law. Because of the influence of phase error, there is a location uncertainty  $\delta P$  for  $P$ .  $n_1$  and  $n_2$  are the calculated normal values affected by  $\delta P$  when the screen is located at Screen 1 and Screen 2 respectively.  $\alpha_1$  denotes the angle difference between  $n_1$  and  $n$ .  $\alpha_2$  represents the angle difference between  $n_2$  and  $n$ . Since  $L_s$  are much larger than  $\delta P$ , the value of  $\alpha_1$  and  $\alpha_2$  can be calculated according to Eq. (8.3):

$$\alpha = \frac{\delta P}{2 \cdot L_s} \quad (8.3)$$

where  $\alpha$  is the normal uncertainty caused by  $\delta P$ . It is clear that  $\alpha$  decreases with the increase of  $L_s$  according to Eq. (8.3). However, there are other factors limiting the length of  $L_s$  in a stereo deflectometry system. One is because the cameras in stereo deflectometry are required to focus on the measured surface, the fringe patterns on the screen are defocused due to the length of  $L_s$ , which results in the increase of  $\delta P$  and  $\alpha$ . In addition, the curvature of the measured surface blurs the mirrored screen. The increase of  $L_s$  enlarges the degree of fuzziness, which leads to the increase of  $\alpha$  as well.

### 8.1.3 Influence of $L_d$

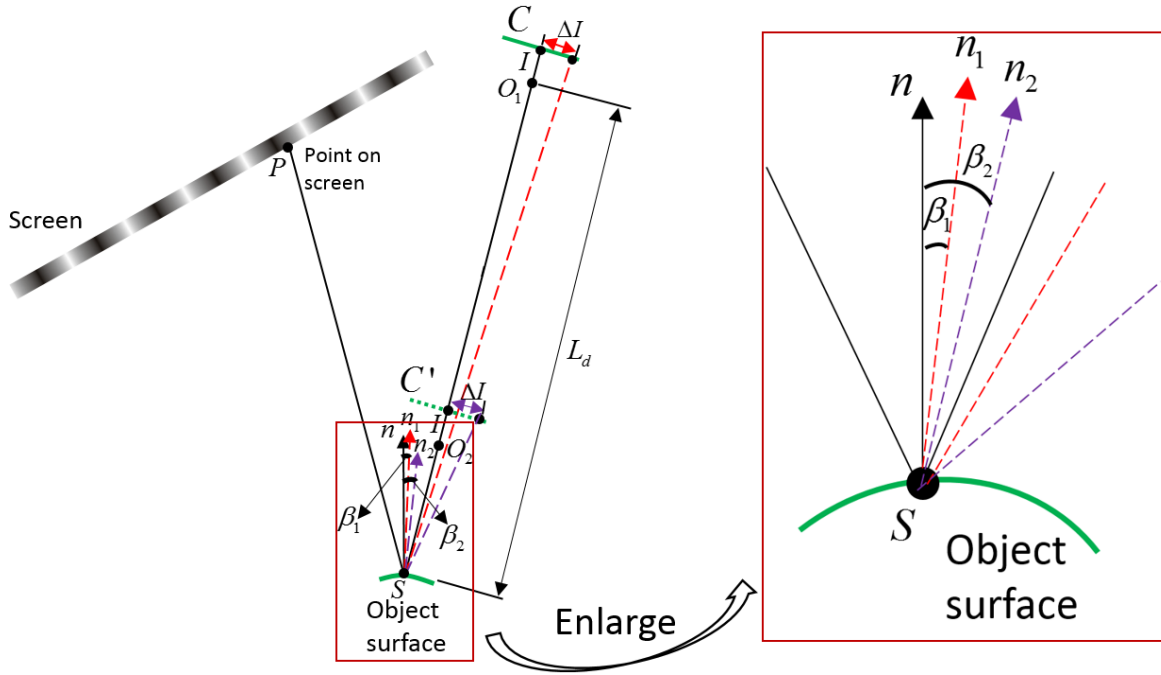


Figure 8.6 Illustration of the influence of  $L_d$ .

A camera is placed at  $C$  and  $C'$  successively to analyse the influence of  $L_d$ , as show in Fig. 8.6.  $O_1$  and  $O_2$  are the optical centre of  $C$  and  $C'$  respectively. The location uncertainty of  $I$  is denoted as  $\delta I$  due to the influence of phase error.  $n_1$  and  $n_2$  are the calculated normal values based on  $C$  and  $C'$  respectively considering the influence of  $\delta I$ . The calculation error of  $n_1$  and  $n_2$  are represented as  $\beta_1$  and  $\beta_2$ . Since  $L_d$  are much larger than  $\delta I$ ,  $\beta_1$  and  $\beta_2$  can be calculated based on Eq. (8.4):

$$\beta = \frac{\delta I}{2 \cdot L_d} \quad (8.4)$$

where  $\beta$  is the normal uncertainty caused by  $\delta I$ . On one hand,  $\beta$  decreases with the increase of  $L_d$  according to Eq. (8.4). On the other hand, based on the analysis of Eqs. (8.1)-(8.2), increasing  $L_d$  enlarges  $\delta s_2$  and  $\delta Z$ , which leads to the measurement error on the other hand. However, if the

camera has a long focus length,  $L_d$  is far greater than  $L_s$  and Eqs. (8.1)-(8.2) can be simplified to Eqs. (8.5)-(8.6):

$$\delta S_2 = \frac{1}{\cos \gamma} \delta S_1 = \frac{1}{\cos \gamma} \delta P'_L \quad (8.5)$$

$$\delta z = \tan \gamma \cdot \delta P'_L \quad (8.6)$$

Therefore, the influence of the change of  $L_d$  on  $\delta S_2$  and  $\delta Z$  can be neglected.

#### 8.1.4 Influence of $\mathcal{G}$

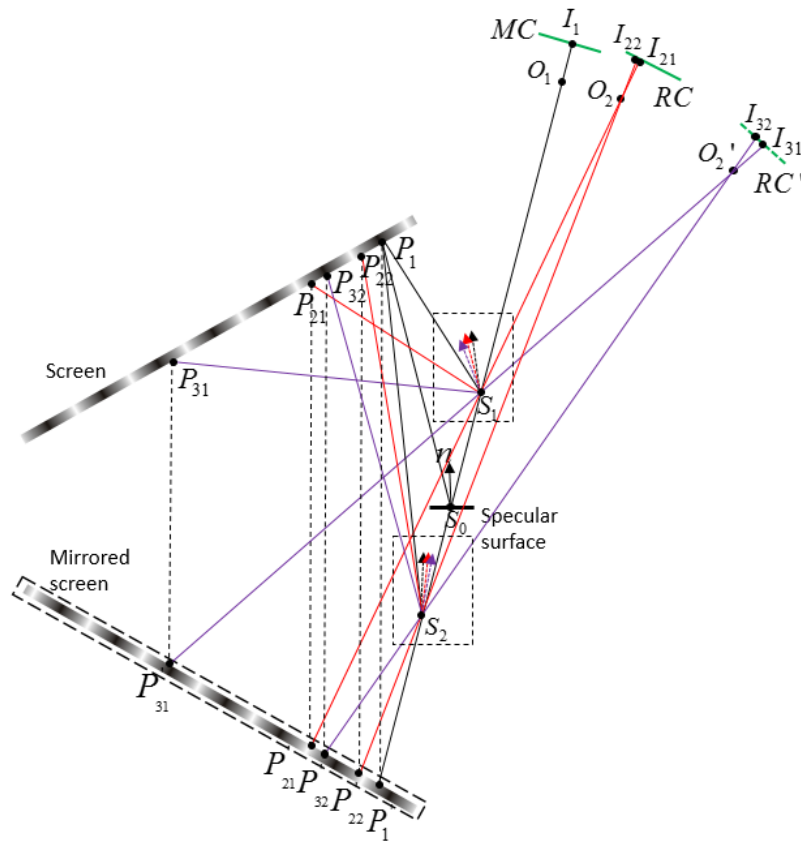


Figure 8.7 Illustration of the influence of  $\mathcal{G}$ .

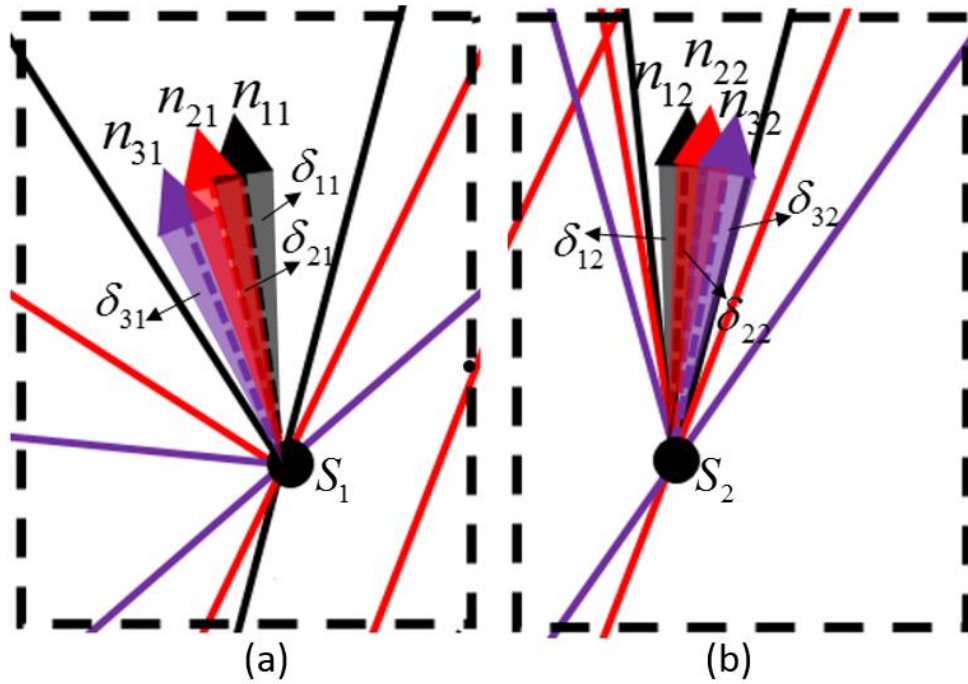


Figure 8.8 Enlarged view of the calculated normal values. (a) The enlarged view of  $S_1$  ; (a) The enlarged view of  $S_2$  .

The influence of  $\mathcal{G}$  is researched in Fig. 8.7. Main camera is placed at  $MC$  . Reference camera is tested at  $RC$  firstly and then moved to  $RC'$  to investigate the influence of  $\mathcal{G}$  .  $O_1$  ,  $O_2$  and  $O_2'$  are the optical center of  $MC$  ,  $RC$  and  $RC'$  respectively.  $S_0$  is a point on the measured surface and  $I_1$  is the image of  $S_0$  on  $MC$  .  $P_1'$  denotes the intersection of the camera ray  $I_1S_0$  and the mirrored screen.  $P_1$  represents the actual point on the Screen of  $P_1'$  . The normal  $n$  of  $S_0$  can be calculated according to the triangular relationship composed of  $P_1$  ,  $S_0$  , and  $I_1$  according to the reflection law. Based on the same principle, normal vectors of  $S_1$  and  $S_2$  which are two points on the camera ray of  $I_1S_0$  can be calculated. Fig. 8.8(a) is the enlarged view of  $S_1$  .  $n_{11}$  ,  $n_{21}$  and  $n_{31}$  denote the calculated normal vectors of  $S_1$  based on  $MC$  ,  $RC$  and  $RC'$  respectively. Similarly,  $S_2$  is enlarged in Fig. 8.8(b). The calculated normal vectors of  $S_2$  from  $MC$  ,  $RC$  and  $RC'$  are denoted as  $n_{12}$  ,  $n_{22}$  and  $n_{32}$  . Phase error leads to a measurement uncertainty for each calculated normal vector, as  $\delta_{11}$  ,  $\delta_{21}$  ,  $\delta_{31}$  ,  $\delta_{12}$  ,  $\delta_{22}$  ,  $\delta_{32}$  shown in Fig. 8.8. It is clear that the calculated normal vectors from  $MC$  and  $RC$  are overlapped. Therefore, points between  $S_1$  and  $S_2$  would be

wrongly judged to belong to the measured surface when using  $MC$  and  $RC$ . In contrast, there is no overlapping between the calculated normal vectors based on  $MC$  and  $RC'$ .  $S_1$  and  $S_2$  can be determined correctly to be not the points on the measured surface. The above analysis indicates that increasing  $\vartheta$  can increase the system measurement accuracy.

## 8.2 Simulation test

Simulations were performed to test the proposed performance analysis. The simulated main camera and reference camera both have a resolution of  $1616 \times 1216$  pixels. Pixel pitch of the cameras is 0.0035 mm. Fringe displaying screen in the simulation has a resolution of  $1024 \times 1024$  pixels and a 0.294 mm pixel pitch. Through the reflection of a simulated flat specular surface, sinusoidal fringe patterns whose period occupies eight pixels of the screen are displayed in turn and captured by the cameras simultaneously. In order to simulate actual measurement environment, random errors are added into the physical locations of the screen and the camera pixel location based on general experiment results.

### 8.2.1 Verification of the analysis of $\gamma$

A simulation was performed to test the influence of  $\gamma$ .  $L_d$ ,  $L_s$ ,  $\vartheta$  in the simulation are 300 mm, 80 mm and  $10^\circ$  respectively. Random errors with a maximum value of 0.0178 mm and 0.05 pixels were added into the physical locations of screen and camera pixel location respectively.  $\gamma$  varies from  $0^\circ$  to  $25^\circ$ . The relationship between  $\gamma$  and measurement error is acquired as shown in Fig. 8.9(a).

Figure 8.9(a) shows that with increasing  $\gamma$ , measurement error increases gradually. The increasing trend verifies the analysis of section 8.1.1. Therefore,  $\gamma$  should be  $0^\circ$  theoretically. However, because the fringe patterns on the screen are required to be captured by the cameras through the reflection of the surface,  $\gamma$  cannot be  $0^\circ$  in an actual stereo deflectometry system. In general,  $\gamma$  should be as small as possible.

### 8.2.2 Verification of the analysis of $L_S$

$L_S$  varies from 40 mm to 200 mm in increments of 40 mm. According to the results of actual experiment, random errors with a maximum values of 0.0170 mm, 0.0178 mm, 0.022 mm, 0.033 mm and 0.051 mm are added to the physical locations of the screen when  $L_S$  is 40 mm, 80 mm, 120 mm, 160 mm and 200 mm respectively. Random errors with a maximum value of 0.05 pixels were added to the camera pixel location. The relationship between  $L_S$  and measurement error is shown in Fig. 8.9 (b).

Fig. 8.9 (b) shows that the measurement error decreases dramatically when  $L_S$  increases from 40 mm to 120 mm. The main reason for this decreasing trend is that the gradient uncertainty caused by location uncertainty on the screen decreases with increasing  $L_S$  according to Eq. (8.3). However, because phase errors are magnified with the increase of  $L_S$ , the measurement error increases gradually when  $L_S$  changes from 120 mm to 200 mm.

### 8.2.3 Verification of the analysis of $L_d$

$L_S$ ,  $\vartheta$ , and  $\gamma$  are 80 mm,  $10^\circ$ ,  $0^\circ$  respectively in a simulation for study  $L_d$ . Increasing  $L_d$  from 200 mm to 700 mm in increments of 50 mm, Fig. 8.9(c) shows the relationship between  $L_d$  and measurement error.

Simulation result shows that with increasing  $L_d$ , measurement error decreases gradually. The decreasing trend confirms the analysis of section 8.1.3. Hence, theoretically  $L_d$  should be as large as possible. However, large  $L_d$  results in a similarly large sized stereo deflectometry system. In general,  $L_d$  should be determined by overall considering the measurement accuracy and the application.

### 8.2.4 Verification of the analysis of $\mathcal{G}$

The relationship between  $\mathcal{G}$  and measurement error is studied through a simulation with  $L_s$ ,  $L_d$ ,  $\gamma$  equaling 80 mm, 300 mm and  $0^\circ$  respectively. Fig. 8.9(d) shows the experimental result which reflects that measurement error decreases gradually with increasing  $\mathcal{G}$  and is almost stable from  $10^\circ$ . The decreasing trend verifies the analysis of section 8.1.4. Therefore, in general,  $\mathcal{G}$  should be no less  $10^\circ$ .

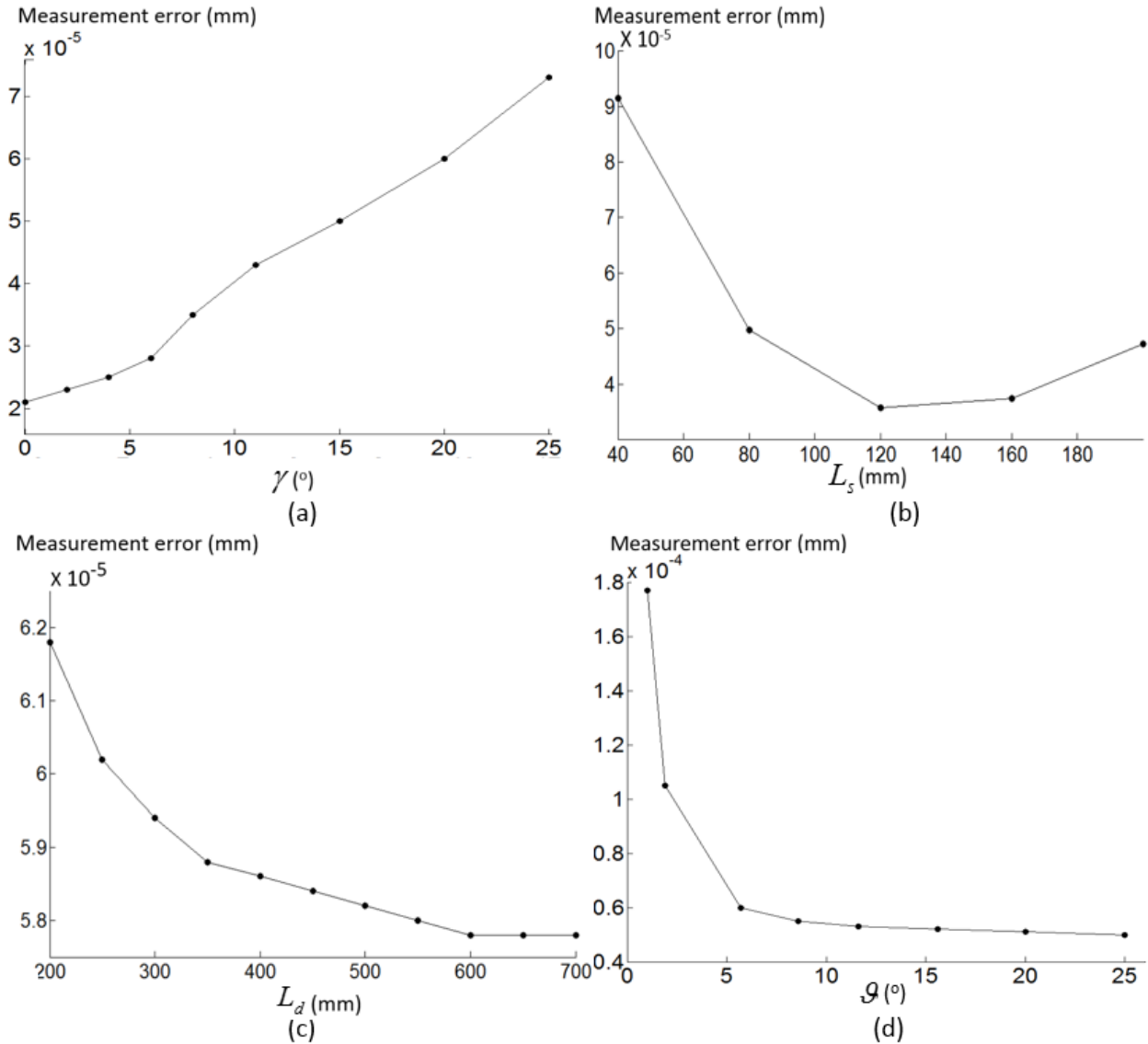


**Figure 8.9** The obtained relation between geometric parameters and measurement error based on simulation results. (a) Relation between  $\gamma$  and measurement error; (b) relation between  $L_s$  and measurement error; (c) relation between  $L_d$  and measurement error; (d) relation between  $\mathcal{G}$  and measurement error.

### 8.3 Actual experiments

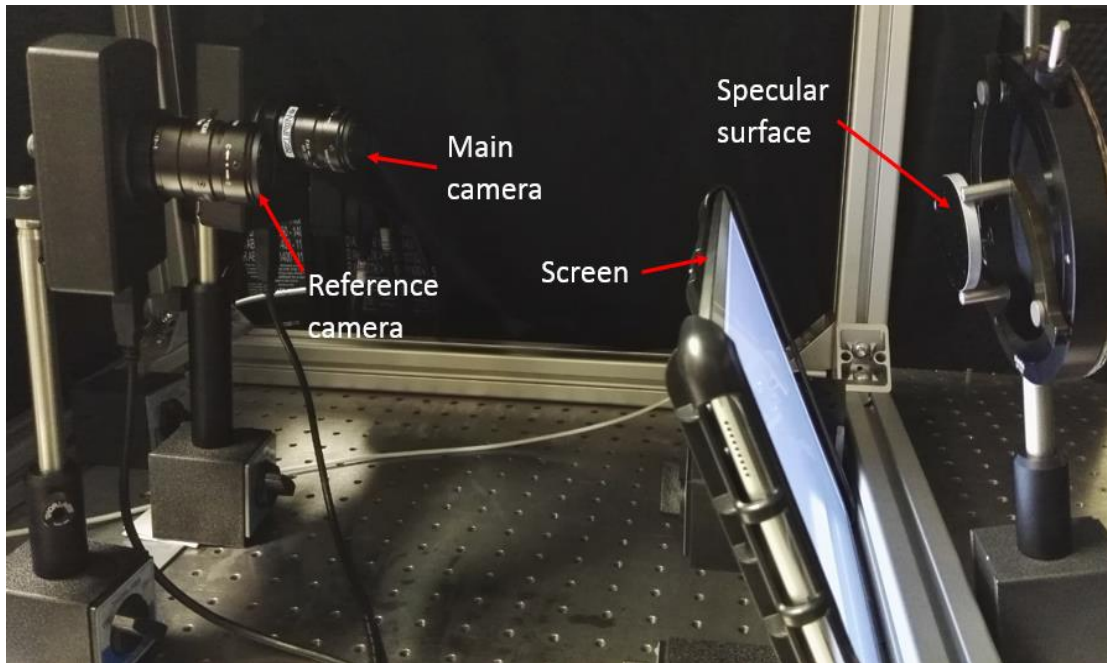


**Figure 8.10** The setup of stereo deflectometry system.

Based on the above analysis and simulation results, a measurement system was set up as shown in Fig. 8.10. Two Lumenera CCD sensors (Model Lw235M) are used as main camera and reference camera of the system. Resolution of the sensors is  $1616 \times 1216$  pixels. Chapter 7 have determined that decreasing the pixel size of the fringe displaying screen can increase measurement accuracy. iPad Pro (<https://www.apple.com/uk/ipad-pro/>) has a ultra-fine pixel size of 0.096 mm which is much smaller than the most common display pixel size (around 0.3 mm). Therefore, under the control of Display Duet (<https://www.duetdisplay.com/>), an iPad Pro with a 12.9 inch size is applied as the displaying fringe screen. The system was calibrated with the method proposed in Chapter 6.

Firstly, experiments were conducted to investigate the influence of  $L_s$  on phase error. Since the cameras in a stereo deflectometry system are required to focus on the measured surface,  $L_s$  makes the mirrored screen out of the depth of focus of the cameras and results in a blur of the captured fringe patterns. Phase error increases with the increase of the degree of fuzziness, which leads to a decrease in measurement accuracy. The relation between  $L_s$  and phase error is investigated based on an actual experiment. Errors of absolute phase maps can be obtained when  $L_s$  varies

from 0 mm to 200 mm in increments of 40 mm by applying phase-shifting and phase unwrapping technique (Zhang, Towers et al. 2006). Fig. 8.11 shows the experiment result. When  $L_s$  is 0 mm, phase error is 0.0415 rad which is significantly larger than the phase error (0.0151 rad) obtained when  $L_s$  is 40 mm. The reason for this phenomenon is because when the camera is focused on the mirrored screen, LCD pixel grids and moiré fringe (Xu, Gao et al. 2017) are recorded by the camera. The recorded pixel grids and moiré fringe generate large errors on phase maps. When  $L_s$  is larger than 40 mm, phase error increases dramatically with increasing  $L_s$ . The main reason leading to this increasing trend is that the degree of defocus of the mirrored screen is magnified with  $L_s$  increasing. Experimental results of this experiment were used to provide the correct phase errors for the above simulation study of  $L_s$ .

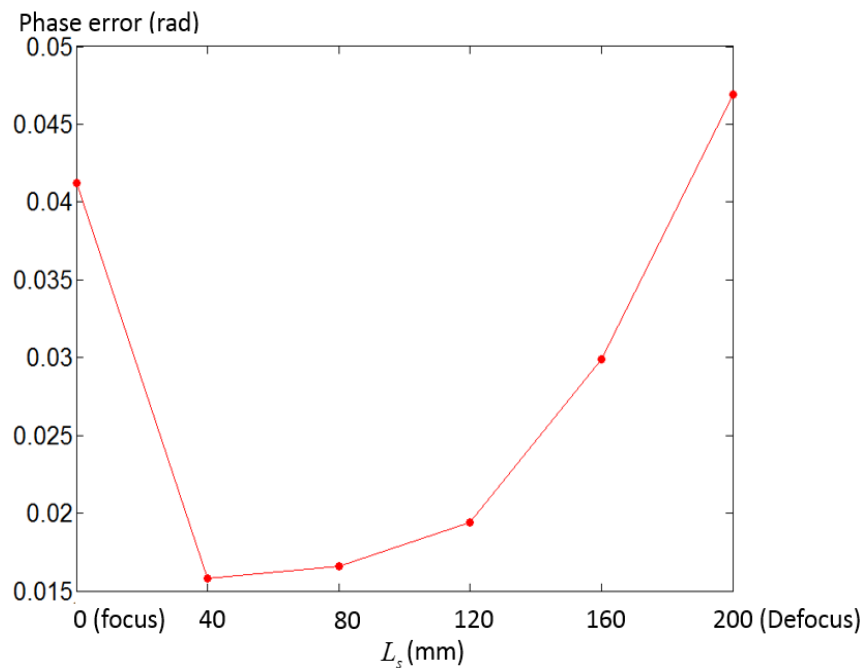


**Figure 8.11 Relation between  $L_s$  and phase error.**

Besides image blurring brought from defocus, curvature of the measured surface also blurs the mirrored fringe patterns. In order to demonstrate this point, an experiment was carried out by capturing fringe patterns reflected from mirrors with different curvatures. Three mirrors were tested: a flat mirror, a concave mirror with 200 mm radius of curvature, and a concave mirror with 100 mm radius of curvature. The captured fringe patterns when  $L_s$  is 80 mm and 120 mm are

shown in Fig. 8.12. Results demonstrate with increasing mirror curvature, fringe density decreases and blurring increases. Increasing  $L_s$  will amplify the influence of the mirror's curvature. Therefore,  $L_s$  should be around 80 mm by comprehensive considering measurement accuracy and measurement range of mirror curvature.

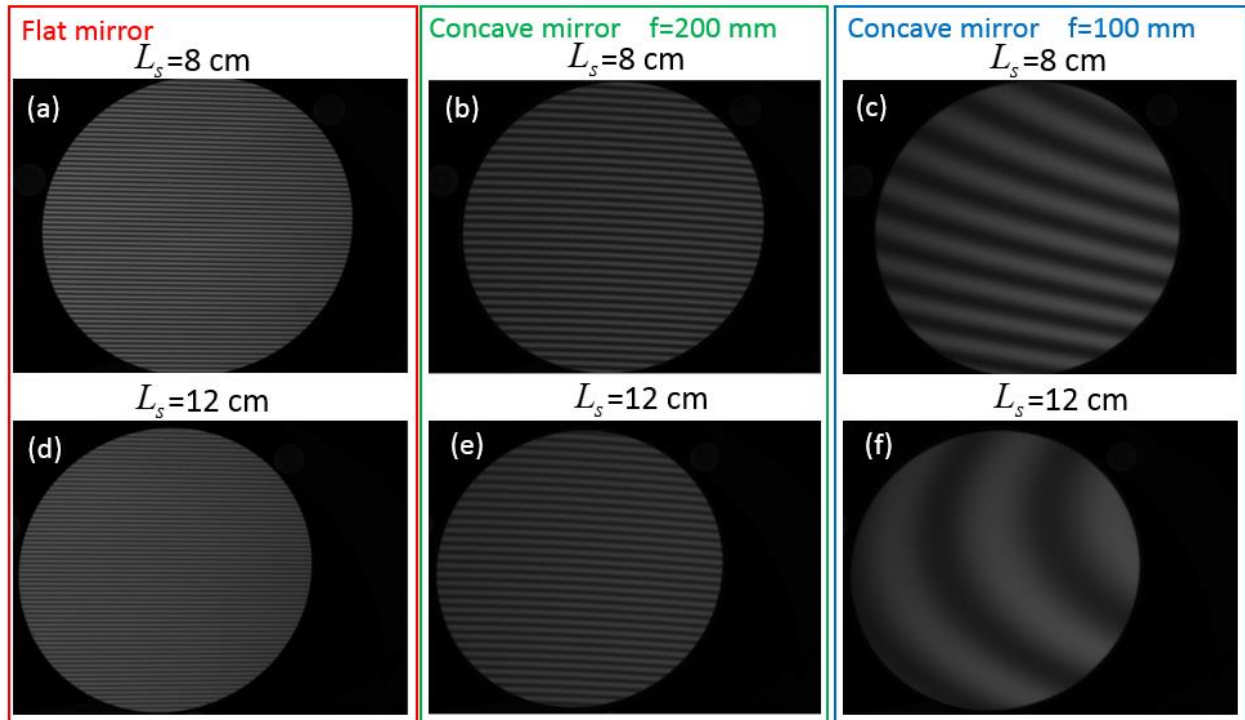


**Figure 8.12 Relation between mirrored fringe pattern and mirror curvature. (a) Flat mirror when  $L_s$  is 80 mm; (b) concave mirror with 200 mm radius of curvature when  $L_s$  is 80 mm; (c) concave mirror with 100 mm radius of curvature when  $L_s$  is 80 mm; (d) flat mirror when  $L_s$  is 120 mm; (e) concave mirror with 200 mm radius of curvature when  $L_s$  is 120 mm; (f) concave mirror with 100 mm radius of curvature when  $L_s$  is 120 mm.**

An additional experiment was performed using an optical flat with  $\lambda/20$  flatness from Edmund (<https://www.edmundoptics.com/>).  $\gamma$  was changed to four values in an experiment:  $10^\circ$ ,  $15^\circ$ ,  $20^\circ$  and  $25^\circ$ . Fig. 8.13(a) shows the measurement errors increase significantly with increasing  $\gamma$ . This confirms the results of the analysis described earlier. Altering  $L_s$  at 60 mm, 80 mm, 100 mm and 120 mm, Fig. 8.13 (b) shows the measurement errors have a similar trend to the simulation results. Fig. 8.13 (c) shows the influence of  $L_d$  on measurement accuracy. Increasing  $L_d$  from 240 mm to 320 mm in increments of 20 mm, measurement errors decrease gradually during the process. This result corresponds to the above analysis of  $L_d$ . Fig. 8.13 (d) shows the trend of measurement errors

for four different values of  $\mathcal{G}$  :  $10^\circ$ ,  $15^\circ$ ,  $20^\circ$  and  $25^\circ$ . Measurement errors change slightly from  $10^\circ$ , which corresponds to the trend as seen in the simulation.

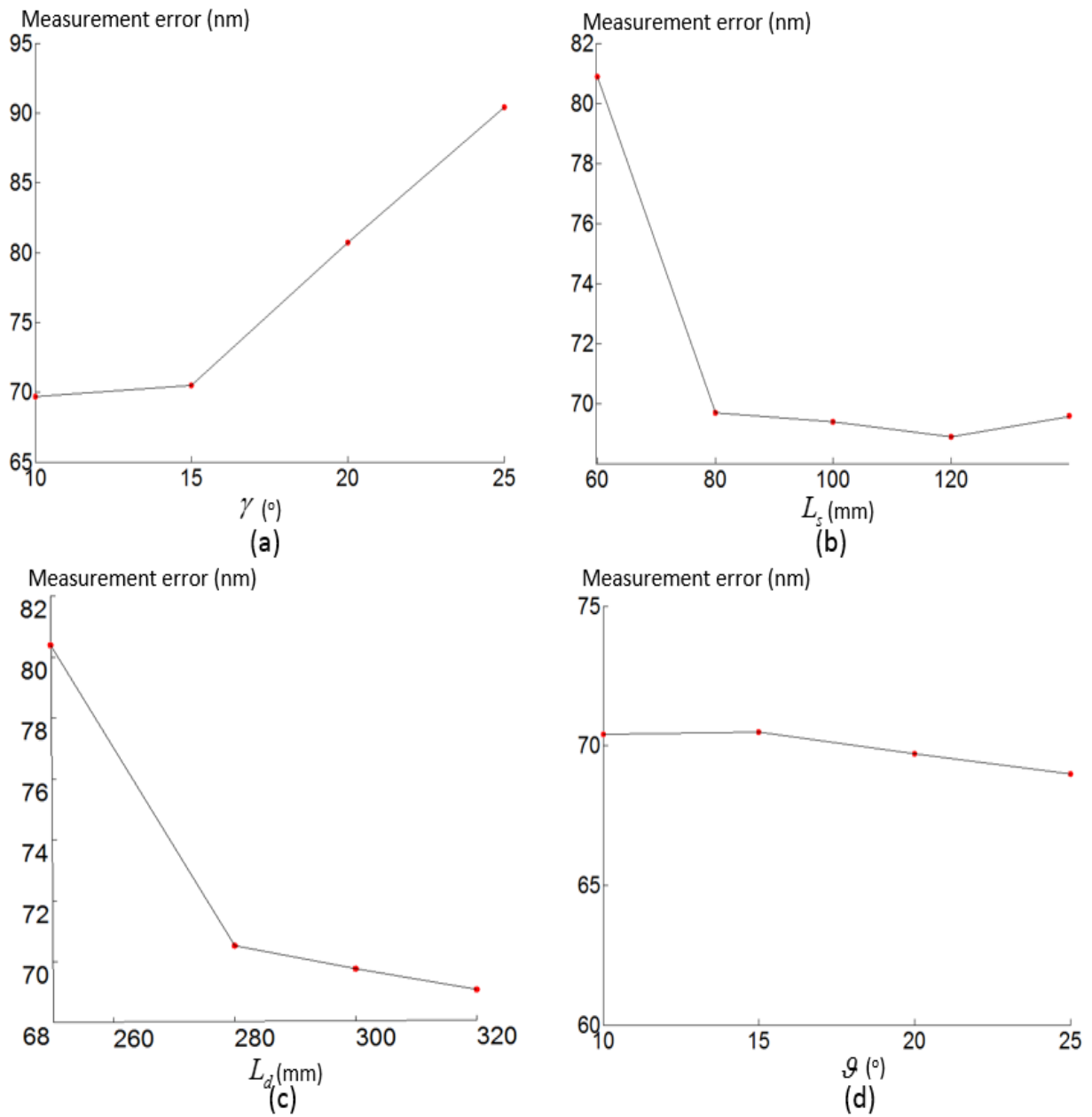


**Figure 8.13** The obtained relation between geometric parameters and measurement error based on actual experimental results. (a) Relation between  $\gamma$  and measurement error; (b) relation between  $L_s$  and measurement error; (c) relation between  $L_d$  and measurement error; (d) relation between  $\mathcal{G}$  and measurement error.

## **8.4 Summary**

The arrangement of the screen and the cameras in a stereo deflectometry system has influence on the measurement accuracy of the system. In order to analysis the influence of the arrangement and improve the measurement accuracy of stereo deflectometry, four geometric parameters, the angle between main camera and reference camera, the angle between the main camera ray and the normal of the measured surface, the distance between the main camera and the measured surface, and the distance between the screen and the measured surface, are investigated through error model analysis, simulation test and experimental verification. This performance analysis will optimize the design of a stereo defletometry system, decreasing measurement error caused by system component positioning error. In the next chapter, a stereo deflectometry system is set up based on the analysis in this chapter.

## 9. Experiment evaluation and future work

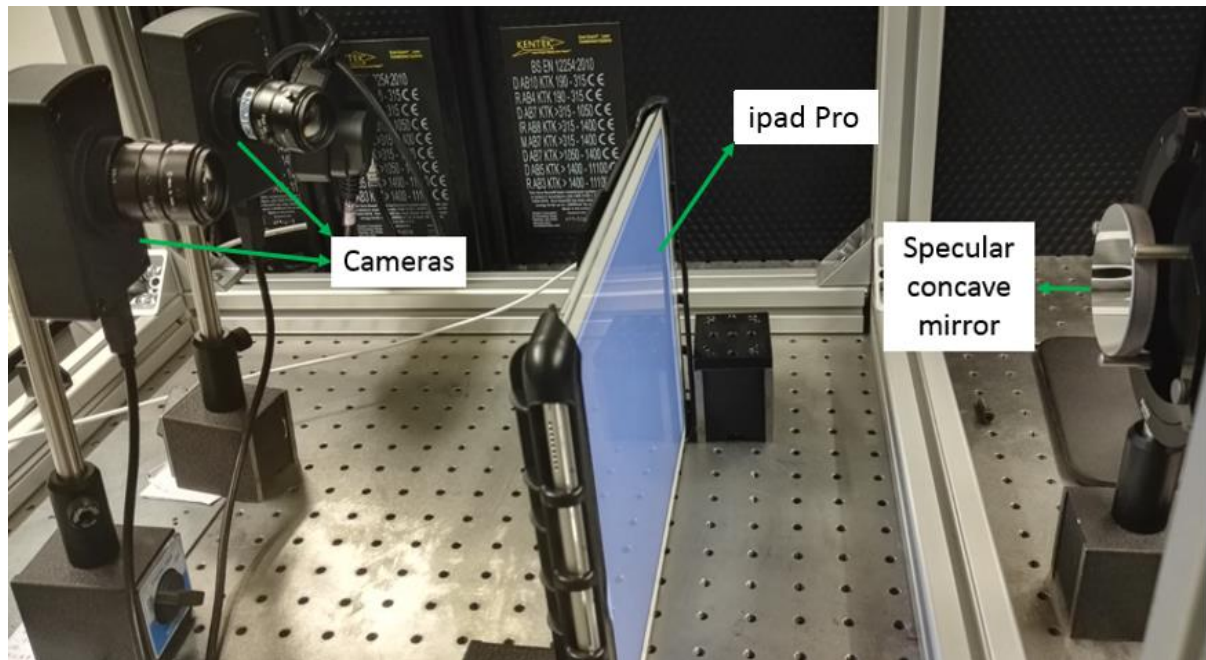
This chapter presents experimental results to evaluate the measurement accuracy of an optimised stereo deflectometry system. According to the investigation of Chapter 7, a stereo deflectometry system using an iPad Pro as the fringe-displaying screen was constructed. The arrangement of the system such as cameras, display screen and the measurement object were optimised based on the performance analysis studied in Chapter 8. The system was calibrated using the camera calibration and systemic calibration techniques investigated in Chapter 4-6. Evaluation experiments were performed by measuring a given optical flat and a given concave mirror.

This chapter also summarises the outcomes of this research and highlights the contribution to knowledge in the relevant research fields. Finally, the future work of the research is discussed.

### 9.1 Experiment evaluation

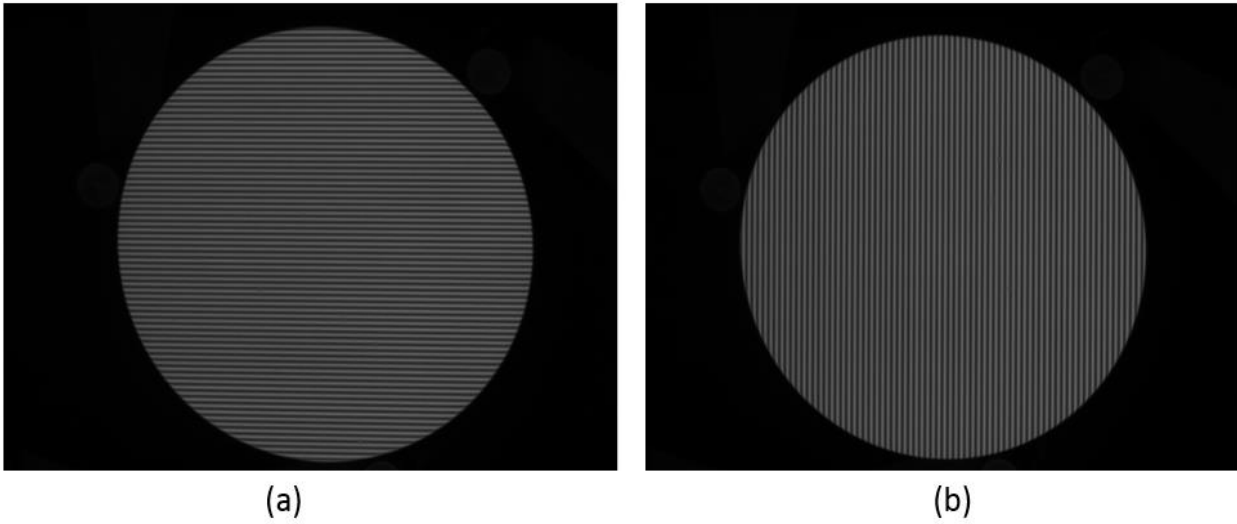
#### 9.1.1 System and measurement results

Fig. 9.1 shows a stereo deflectometry system designed based on the investigation of the above chapters. This system uses an iPad Pro as the fringe-displaying screen to display fringe patterns during measurement process. According to the study of chapter 7, the occupied screen pixel number per fringe period is set to eight pixels. Two CCD sensors from Lumenera (<https://www.lumenera.com/>) with 35 mm fixed focal lens are used as the main camera and the reference camera in stereo deflectometry. The model of the sensors is Lw235M. The image resolution of the sensors is 1616×1216 pixels. Geometric parameters of the measurement system were determined according to the studied performance analysis in Chapter 8.  $\theta$  is 10° and  $L_d$  is 300 mm in consideration of the size limit of the measurement system.  $L_s$  is chosen to be 80 mm. In order to guarantee that the displayed patterns can be ‘see’ by the cameras,  $\gamma$  is designed to be 10°. The measurement system was calibrated based on the calibration technique described in Chapter 4-6.



**Figure 9.1 A designed stereo deflectometry system.**

With the purpose of evaluating the system's measurement accuracy, an optical flat with  $\lambda/20$  flatness was tested with the system. The size of the optical flat is 2 inch. Fig. 9.2 shows one of the captured images with fringe information in the main camera. Fig. 9.2(a) is one of the captured images with horizontal fringe pattern. Fig. 9.2(b) is one of the captured images with vertical fringe pattern. By applying phase shifting and phase unwrapping algorithm, absolute phase maps can be obtained from the fringe patterns. The obtained absolute phase maps of the measured optical flat in the main camera are shown in Fig. 9.3. Fig. 9.3(a) is the absolute phase map extracted from the horizontal fringe patterns. Fig. 9.3(b) is the absolute phase map extracted from the vertical fringe patterns. Fig. 9.4 shows the measured gradient information of the optical flat based on the gradient calculation algorithm described in Chapter 3. Gradient data along x direction and along y direction are shown in Fig. 9.4(a) and Fig. 9.4(b) respectively. By using the integration technique studied by Ren et al. ([Ren, Gao et al. 2016](#)), the 3D form of the measured surface was reconstructed based on the gradient information. A plane was fitted based on the 3D form data and was used as a benchmark to evaluate the measurement accuracy. Fig. 9.5 shows the deviation between the measured 3D form and the plane. The PV of the deviation is 69.7 nm.



**Figure 9.2** One of the captured images with fringe information in the main camera. (a) One of the captured images with horizontal fringe pattern; (b) one of the captured images with vertical fringe pattern.

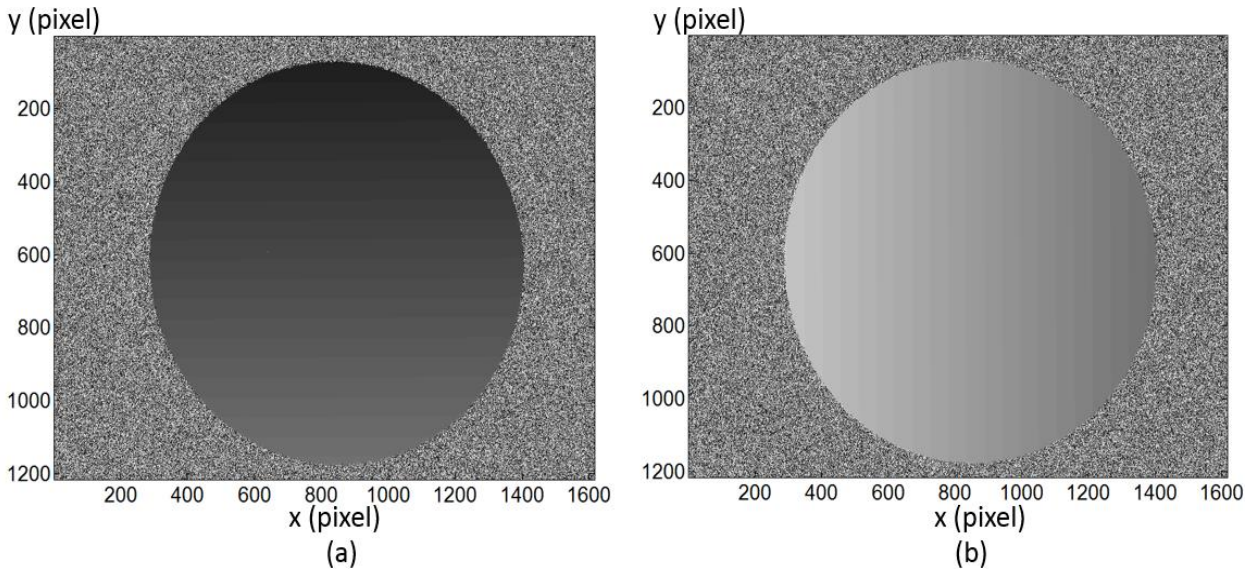


**Figure 9.3** The obtained absolute phase maps of the measured optical flat in main camera. (a) Horizontal absolute phase map; (b) vertical absolute phase map.

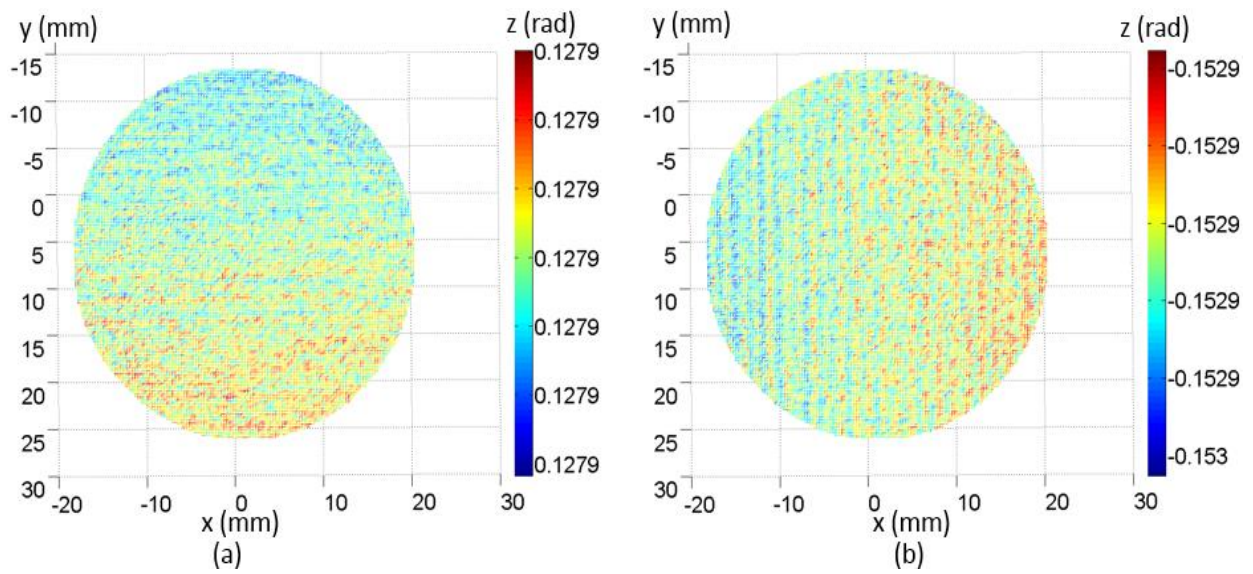


**Figure 9.4** The obtained gradient information. (a) Gradient data along x direction; (b) gradient data along y direction.

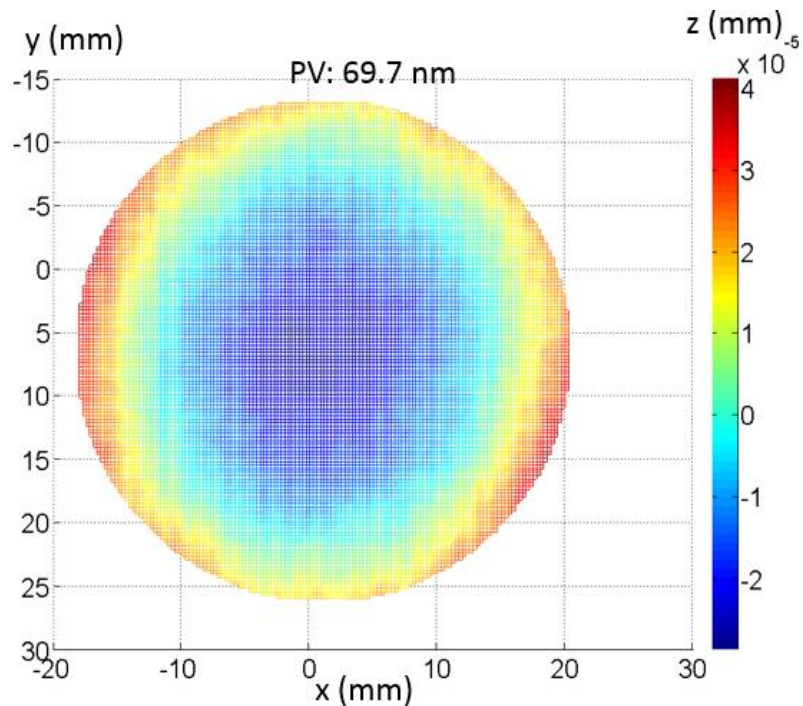


**Figure 9.5** Measurement error of an optical flat.

The system was also tested with a concave mirror from Edmund (<https://www.edmundoptics.com/>). Fig. 9.6(a) shows the measured concave mirror. The surface accuracy of the mirror is  $\lambda/8$ . One of the captured images in the main camera with deformed fringe information is shown in Fig. 9.6(b). The diameter of the measurement field of the system is

about 2 inches. The test mirror is larger than the measurement field, therefore central section of the mirror is measured, as shown in Fig. 9.6(b). Fig. 9.7(a) shows the absolute phase map of the concave mirror extracted from the horizontal fringe patterns. Fig. 9.7(b) shows the absolute phase map of the concave mirror extracted from the vertical fringe patterns. The reconstructed 3D form of the testing concave mirror is shown in Fig. 9.8(a). Fig. 9.8(b) shows the difference between the reconstructed 3D form and the surface parameters provided by the manufacturer. The PV of the difference is 154.2 nm. The experimental results of an optical flat and a concave mirror confirm the designed stereo deflectometry system can acquire the form information of a specular surface with a high precision.

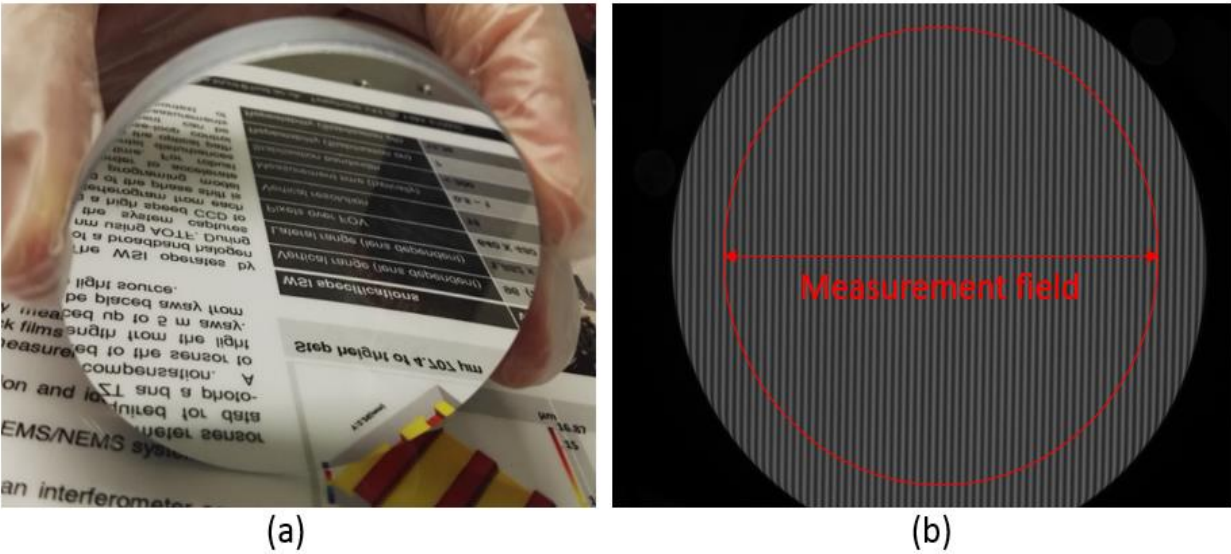


**Figure 9.6** A concave mirror was measured by the system. (a) The measured concave mirror; (b) one of the captured images from the main camera with deformed fringe information.

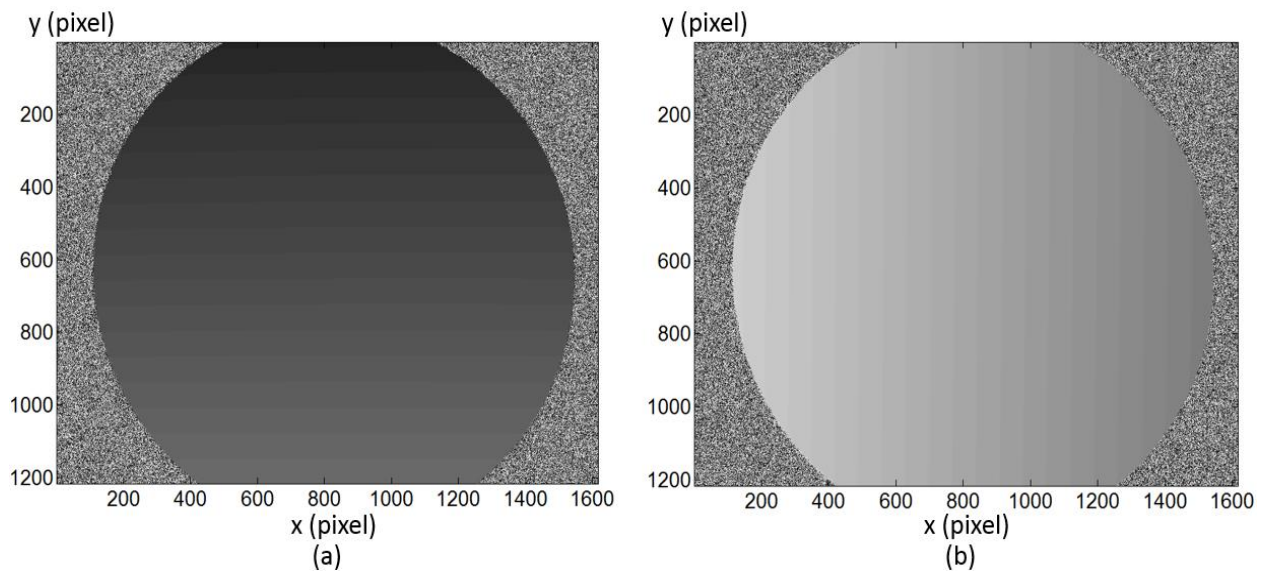


**Figure 9.7** The obtained absolute phase maps of the measured concave mirror in the main camera. (a) Horizontal absolute phase map; (b) vertical absolute phase map.

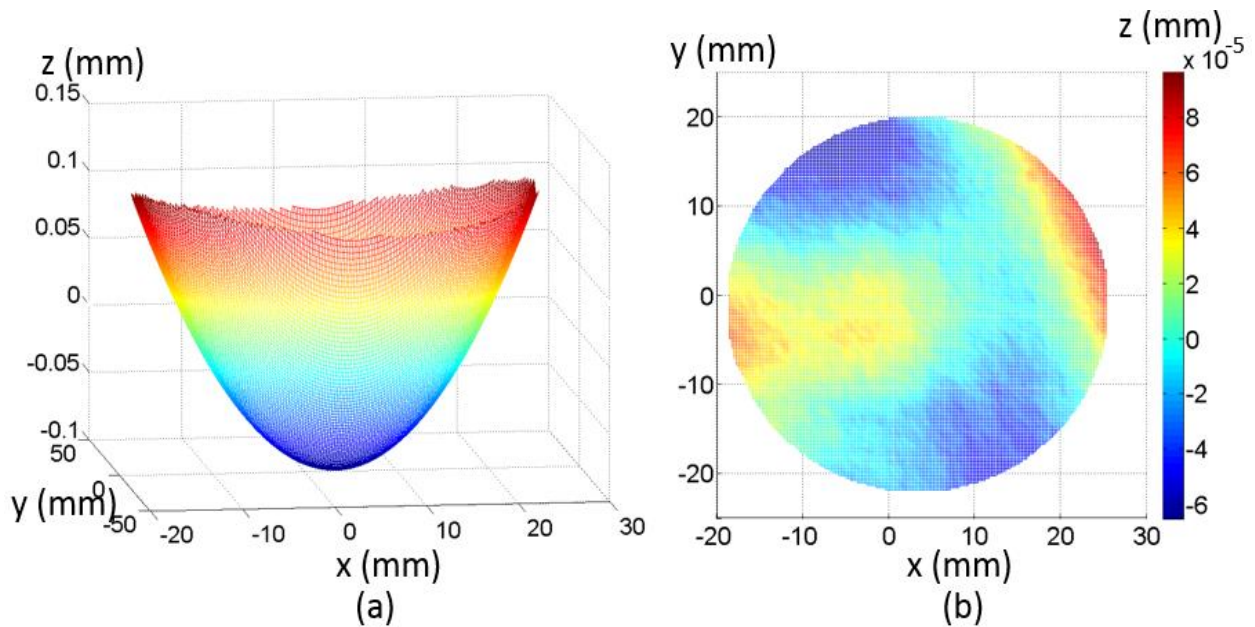


**Figure 9.8** Measurement result of a stock concave mirror. (a) The obtained form of the mirror; (b) the difference between the measurement result and the surface parameters provided by the manufacturer.

### 9.1.2 Summary

Based on the investigated calibration algorithms, phase analysis and performance analysis method, a stereo deflectometry system was designed and optimised. In order to evaluate the measurement accuracy of the designed system, two evaluation experiments were conducted. Experimental results show the measurement accuracy of the system can reach tens of nanometres.

## **9.2 Conclusions and future work**

### **9.2.1 Summary of contributions**

This thesis investigates key techniques of a stereo deflectometry system to improve the measurement accuracy of the system.

The first contribution of this thesis is the development of a camera calibration technique based on phase target. Camera distortion is eliminated with an iterative distortion compensation technique. Defocus techniques and fitting and interpolation techniques are developed to improve the feature extraction accuracy of the phase target. Comparing with traditional camera calibration methods, the developed camera calibration technique can achieve better calibration accuracy.

The second contribution of this thesis is the development of a calibration technique for calibrating non-overlapping camera system. The developed calibration technique is more suitable for stereo deflectometry than other calibration methods explored for non-overlapping camera system. Experimental results verified the flexibility and accuracy of the developed calibration technique.

The third contribution of this thesis is the development of a systemic calibration technique for stereo deflectometry. In order to improve the measurement accuracy of the system, a systemic calibration technique is developed based on the investigations described in Chapter 4 and Chapter 5. By applying an iterative distortion compensation algorithm, the developed calibration technique can significantly enhance calibration accuracy. The flexibility and accuracy of the developed calibration technique have been tested by simulation and experimental results. In a measuring of an optical flat, the PV of the measurement error using the developed calibration technique is 69.7 nm, which is about four times better than the traditional calibration method.

The fourth contribution of this thesis is the development of a search algorithm with an evaluation function for increasing the accuracy and robustness of stereo deflectometry's calibration process. The developed algorithm can solve the low-accuracy initial value problem caused by image distortion. Experimental results prove the developed calibration technique can effectively enhance stereo deflectometry's calibration accuracy and measurement accuracy. The RMS of calibration error can be reduced to 0.05 pixels from 0.31 pixels by using the developed algorithm.

The fifth contribution of this thesis is the development of a mathematical model to study the influence of phase ambiguity and gradient ambiguity in stereo deflectometry. The pixel size of the fringe-displaying screen and the occupied LCD pixels per fringe period are investigated through systematically analysing their influence on phase ambiguity and gradient ambiguity. Experimental results confirm the analysis developed in this thesis could considerably enhance stereo deflectometry's measurement accuracy.

The sixth contribution of this thesis is the development of a performant analysis for a stereo deflectometry system. This analysis is developed to improve the system's measurement accuracy. Four geometric parameters of the system are analysed based on the investigated error models. Experiments were performed based on simulation test and experimental verification. Experimental results confirm the effects of these four parameters on the measurement results.

### **9.2.2 Future work**

Detailed work in the development of the key techniques of stereo deflectometry in this thesis revealed more interesting issues, some of which require to be investigated further:

- In Chapter 9, the tested mirrors have high form accuracy and are treated as benchmarks to evaluate the stereo deflectometry system's measurement accuracy. In order to make the evaluation more convincing, the measurement results obtained with stereo deflectometry need to be compared with interferometry such as a ZYGO Verifire interferometer system (<https://www.zygo.com/?/met/interferometers/>) or 4D interferometer.
- The stereo deflectometry system described in this thesis can only accurately measure the surface with small gradient. When measuring a surface with big gradient surface, the measurement accuracy of the system cannot reach nanometres' level because the curvature of the measured surface leads to big phase error. New calibration method and imaging model need to be investigated for the applications of large gradient specular surfaces to enable the stereo deflectometry for these kind of applications.
- The current applied fringe-displaying screen in a stereo deflectometry system is not an ideal screen. For example, there is a glass layer in front of its displaying plane. The refraction of the light through the glass layer will cause errors in the calibration and

measurement processes. The influence of the glass layer on measurement accuracy need to be considered in order to further increase the measurement accuracy of the system.

- The camera calibration method described in this thesis is based on pinhole model. This model is simplified imaging model which cannot match real imaging process perfectly. It will bring errors to the calibration and measurement of stereo deflectometry. A new imaging model which can represent the real imaging process is necessary in order to further improve calibration accuracy.
- Introducing data fusion to the system by using different field view CCD cameras to improve surface measurement accuracy. When deflectometry is used for measuring large specular surfaces, lateral resolution is significantly decreased. By installing the third CCD camera with a smaller field view can result in the surface measurement with increased lateral resolution. By fusing the two sets of measurement together, surface measurement may be improved.

## References

- Adhikari, R. (2004). Sensitivity and noise analysis of 4 km laser interferometric gravitational wave antennae, Massachusetts Institute of Technology.
- Alvarez, L., L. Gómez and P. Henríquez (2012). "Zoom dependent lens distortion mathematical models." Journal of Mathematical Imaging and Vision **44**(3): 480-490.
- Balzer, J., S. Hofer and J. Beyerer (2011). Multiview specular stereo reconstruction of large mirror surfaces. Computer Vision and Pattern Recognition (CVPR), 2011 IEEE Conference on, IEEE.
- Bell, T., J. Xu and S. Zhang (2016). "Method for out-of-focus camera calibration." Applied optics **55**(9): 2346-2352.
- Bittar, M. and R. Bartel (2001). Multi-frequency electromagnetic wave resistivity tool with improved calibration measurement, Google Patents.
- Bothe, T., W. Li, C. von Kopylow and W. P. Juptner (2004). High-resolution 3D shape measurement on specular surfaces by fringe reflection. Optical metrology in production engineering, International Society for Optics and Photonics.
- Bowe, B. W. and V. Toal (1998). "White light interferometric surface profiler." Optical Engineering **37**(6): 1796-1800.
- Breitbarth, M., P. Kühmstedt and G. Notni (2009). Calibration of a combined system with phase measuring deflectometry and fringe projection. Optical Measurement Systems for Industrial Inspection VI, International Society for Optics and Photonics.
- Brigham, E. O. and E. O. Brigham (1988). The fast Fourier transform and its applications, prentice Hall Englewood Cliffs, NJ.
- Butel, G. P., G. A. Smith and J. H. Burge (2014). "Binary pattern deflectometry." Applied optics **53**(5): 923-930.
- Capanni, A., L. Pezzati, D. Bertani, M. Cetica and F. Francini (1997). "Phase-shifting speckle interferometry: a noise reduction filter for phase unwrapping." Optical Engineering **36**(9): 2466-2472.
- Chan, P. H., P. J. Bryanston-Cross and S. C. Parker (1995). "Fringe-pattern analysis using a spatial phase-stepping method with automatic phase unwrapping." Measurement Science and Technology **6**(9): 1250.
- Cui, H., W. Liao, N. Dai and X. Cheng (2012). "A flexible phase-shifting method with absolute phase marker retrieval." Measurement **45**(1): 101-108.

- de Groot, P. (2011). Coherence scanning interferometry. Optical measurement of surface topography, Springer: 187-208.
- De la Escalera, A. and J. M. Armingol (2010). "Automatic chessboard detection for intrinsic and extrinsic camera parameter calibration." Sensors **10**(3): 2027-2044.
- Deck, L. and P. De Groot (1994). "High-speed noncontact profiler based on scanning white-light interferometry." Applied optics **33**(31): 7334-7338.
- Dong, S., X. Shao, X. Kang, F. Yang and X. He (2016). "Extrinsic calibration of a non-overlapping camera network based on close-range photogrammetry." Applied optics **55**(23): 6363-6370.
- Donné, S., J. De Vylder, B. Goossens and W. Philips (2016). "MATE: Machine learning for adaptive calibration template detection." Sensors **16**(11): 1858.
- Dörband, B. and G. Seitz (2001). "Interferometric testing of optical surfaces at its current limit." Optik - International Journal for Light and Electron Optics **112**(9): 392-398.
- Duerr, F., Y. Nie and H. Thienpont (2015). Potential Benefits of Freeform Optics in On-Axis Imaging Applications. Imaging and Applied Optics 2015, Arlington, Virginia, Optical Society of America.
- Dursun, A., S. Özder and F. N. Ecevit (2004). "Continuous wavelet transform analysis of projected fringe patterns." Measurement Science and Technology **15**(9): 1768.
- Ettl, S., J. Kaminski, M. C. Knauer and G. Häusler (2008). "Shape reconstruction from gradient data." Applied Optics **47**(12): 2091-2097.
- Evans, C. J. and A. D. Davies (2015). Freeform Optical Surface Metrology: Challenges and Capabilities. Imaging and Applied Optics 2015, Arlington, Virginia, Optical Society of America.
- Faber, C. (2012). New methods and advances in deflectometry, Erlangen Scientific Press.
- Fang, F. Z., X. D. Zhang, A. Weckenmann, G. X. Zhang and C. Evans (2013). "Manufacturing and measurement of freeform optics." CIRP Annals - Manufacturing Technology **62**(2): 823-846.
- Ferrari, P. (2010). Coordinate measurement machine, Google Patents.
- G.Hausler, C.Richter, K.Leitz and M.Knauer (2008). "Microdeflectometry-a novel tool to acquire three-dimensional microtopography with nanometer height resolution." Opt.Lett.(4): 396-398.
- Ghiglia, D. C. and M. D. Pritt (1998). Two-dimensional phase unwrapping: theory, algorithms, and software, Wiley New York.
- Gorthi, S. S. and P. Rastogi (2010). "Fringe projection techniques: whither we are?" Optics and lasers in engineering **48**(IMAC-REVIEW-2009-001): 133-140.

- Graves, L. M. (1927). "Riemann integration and Taylor's theorem in general analysis." Transactions of the American Mathematical Society **29**(1): 163-177.
- Guan, B., Y. Shang, Q. Yu, Z. Lei and X. Zhang (2015). A simple and flexible calibration method of non-overlapping camera rig. Videometrics, Range Imaging, and Applications XIII, International Society for Optics and Photonics.
- Harasaki, A., J. Schmit and J. C. Wyant (2000). "Improved vertical-scanning interferometry." Applied optics **39**(13): 2107-2115.
- Harasaki, A. and J. C. Wyant (2000). "Fringe modulation skewing effect in white-light vertical scanning interferometry." Applied Optics **39**(13): 2101-2106.
- Hariharan, P. (2003). Optical interferometry. Boston, Academic Press.
- Hartley, R. and S. B. Kang (2007). "Parameter-free radial distortion correction with center of distortion estimation." IEEE Transactions on Pattern Analysis and Machine Intelligence **29**(8): 1309-1321.
- Häusler, G., C. Faber, E. Olesch and S. Ettl (2013). Deflectometry vs. interferometry. Optical Measurement Systems for Industrial Inspection VIII, International Society for Optics and Photonics.
- Häusler, G., C. Richter, K.-H. Leitz and M. C. Knauer (2008). "Microdeflectometry—a novel tool to acquire three-dimensional microtopography with nanometer height resolution." Optics letters **33**(4): 396-398.
- Häusler, G., M. Vogel, Z. Yang, A. Kessel, C. Faber and C. Kranitzky (2010). Microdeflectometry and structural illumination microscopy—new tools for 3D-metrology at nanometer scale. Proc Precision Interferometric Metrology, ASPE 2010 Summer Topical Meeting, Asheville, North Carolina, USA.
- Hemmelgarn, T. L., F. K. Bell, F. L. Raleigh and D. K. Greier (2000). Coordinate measuring machine, Google Patents.
- Hesch, J. A., A. I. Mourikis and S. I. Roumeliotis (2008). "Camera to robot-body calibration using planar mirror reflections." University of Minnesota, Dept. of Comp. Sci. & Eng., Tech. Rep 1.
- Heuermann, H. (2006). Calibration method for carrying out multiport measurements on semiconductor wafers, Google Patents.
- Hocken, R. J. and P. H. Pereira (2016). Coordinate measuring machines and systems, CRC Press.
- Huang, L. and A. Asundi (2012). "Improvement of least-squares integration method with iterative compensations in fringe reflectometry." Applied optics **51**(31): 7459-7465.

- Huang, L., M. Idir, C. Zuo, K. Kaznatcheev, L. Zhou and A. Asundi (2015). "Comparison of two-dimensional integration methods for shape reconstruction from gradient data." Optics and Lasers in Engineering **64**: 1-11.
- Huang, L., Q. Kemaoy, B. Pan and A. K. Asundi (2010). "Comparison of Fourier transform, windowed Fourier transform, and wavelet transform methods for phase extraction from a single fringe pattern in fringe projection profilometry." Optics and Lasers in Engineering **48**(2): 141-148.
- Huang, L., C. S. Ng and A. K. Asundi (2011). "Dynamic three-dimensional sensing for specular surface with monoscopic fringe reflectometry." Optics express **19**(13): 12809-12814.
- Huang, L., C. S. Ng and A. K. Asundi (2012). "Fast full-field out-of-plane deformation measurement using fringe reflectometry." Optics and Lasers in Engineering **50**(4): 529-533.
- Huang, L., J. Xue, B. Gao, C. McPherson, J. Beverage and M. Idir (2016). "Modal phase measuring deflectometry." Optics express **24**(21): 24649-24664.
- Huang, L., Q. Zhang and A. Asundi (2013). "Camera calibration with active phase target: improvement on feature detection and optimization." Optics letters **38**(9): 1446-1448.
- Huang, P. S., Q. Hu, F. Jin and F.-P. Chiang (1999). "Color-encoded digital fringe projection technique for high-speed 3-D surface contouring." Optical Engineering **38**(6): 1065-1072.
- Huang, R., P. Su, T. Horne, G. Brusa and J. H. Burge (2014). "Optical metrology of a large deformable aspherical mirror using software configurable optical test system." Optical Engineering **53**(8): 085106.
- Huntley, J. M. and H. O. Saldner (1997). "Error-reduction methods for shape measurement by temporal phase unwrapping." JOSA A **14**(12): 3188-3196.
- Huntley, J. M. and H. O. Saldner (1997). "Shape measurement by temporal phase unwrapping: comparison of unwrapping algorithms." Measurement Science and Technology **8**(9): 986.
- Javed, O., K. Shafique and M. Shah (2005). Appearance modeling for tracking in multiple non-overlapping cameras. Computer Vision and Pattern Recognition, 2005. CVPR 2005. IEEE Computer Society Conference on, IEEE.
- Jia, P., J. Kofman and C. E. English (2007). "Two-step triangular-pattern phase-shifting method for three-dimensional object-shape measurement." Optical Engineering **46**(8): 083201.
- Jiang, X., P. Scott and D. Whitehouse (2007). "Freeform Surface Characterisation - A Fresh Strategy." CIRP Annals - Manufacturing Technology **56**(1): 553-556.
- Jiang, X., K. Wang, F. Gao and H. Muhamedsalih (2010). "Fast surface measurement using wavelength scanning interferometry with compensation of environmental noise." Applied optics **49**(15): 2903-2909.

- Jiang, X. J. and D. J. Whitehouse (2012). "Technological shifts in surface metrology." CIRP Annals - Manufacturing Technology **61**(2): 815-836.
- Kemao, Q. (2007). "Two-dimensional windowed Fourier transform for fringe pattern analysis: principles, applications and implementations." Optics and Lasers in Engineering **45**(2): 304-317.
- Kim, J.-S., M. Hwangbo and T. Kanade (2008). Motion estimation using multiple non-overlapping cameras for small unmanned aerial vehicles. Robotics and Automation, 2008. ICRA 2008. IEEE International Conference on, Citeseer.
- Knauer, M. C., J. Kaminski and G. Hausler (2004). Phase measuring deflectometry: a new approach to measure specular free-form surfaces. Optical Metrology in Production Engineering, International Society for Optics and Photonics.
- Kou, L., X. Wang, M. Xiang and M. Zhu (2012). "Interferometric estimation of three-dimensional surface deformation using geosynchronous circular SAR." IEEE Transactions on Aerospace and Electronic Systems **48**(2): 1619-1635.
- Kumar, R. K., A. Ilie, J.-M. Frahm and M. Pollefeys (2008). Simple calibration of non-overlapping cameras with a mirror. Computer Vision and Pattern Recognition, 2008. CVPR 2008. IEEE Conference on, IEEE.
- Lamprecht, B., S. Rass, S. Fuchs and K. Kyamakyia (2007). Extrinsic camera calibration for an on-board two-camera system without overlapping field of view. Intelligent Transportation Systems Conference, 2007. ITSC 2007. IEEE, IEEE.
- Larkin, K. G. (1996). "Efficient nonlinear algorithm for envelope detection in white light interferometry." JOSA A **13**(4): 832-843.
- Leach, R. (2011). Optical measurement of surface topography, Springer.
- Lébraly, P., C. Deymier, O. Ait-Aider, E. Royer and M. Dhôme (2010). Flexible extrinsic calibration of non-overlapping cameras using a planar mirror: Application to vision-based robotics. Intelligent Robots and Systems (IROS), 2010 IEEE/RSJ International Conference on, IEEE.
- Lee, B. S. and T. C. Strand (1990). "Profilometry with a coherence scanning microscope." Applied optics **29**(26): 3784-3788.
- Li, Y. and P. Gu (2004). "Free-form surface inspection techniques state of the art review." Computer-Aided Design **36**(13): 1395-1417.
- Li, Y. and P. Gu (2005). "Inspection of free-form shaped parts." Robotics and Computer-Integrated Manufacturing **21**(4-5): 421-430.

- Liu, Y., S. Huang, Z. Zhang, N. Gao, F. Gao and X. Jiang (2017). "Full-field 3D shape measurement of discontinuous specular objects by direct phase measuring deflectometry." Scientific reports **7**(1): 10293.
- Liu, Y. and X. Su (2012). "Camera calibration with planar crossed fringe patterns." Optik-International Journal for Light and Electron Optics **123**(2): 171-175.
- Liu, Z., G. Zhang, Z. Wei and J. Sun (2011). "Novel calibration method for non-overlapping multiple vision sensors based on 1D target." Optics and Lasers in Engineering **49**(4): 570-577.
- Ma, M., X. Chen and K. Wang (2014). "Camera calibration by using fringe patterns and 2D phase-difference pulse detection." Optik-International Journal for Light and Electron Optics **125**(2): 671-674.
- Malacara-Doblado, D. and I. Ghozeil (2007). "Hartmann, Hartmann–Shack, and other screen tests." Optical Shop Testing, Third Edition: 361-397.
- Malacara, D. (2007). Optical shop testing. Chichester, Wiley-Blackwell.
- Maoling, Q., M. Songde and L. Yi (2000). "Overview of camera calibration for computer vision." Acta Automatica Sinica **26**(1): 43-55.
- McMurtry, D. R. (1982). Coordinate measuring machine, Google Patents.
- Mei, B., W. Zhu, K. Yuan and Y. Ke (2015). "Robot base frame calibration with a 2D vision system for mobile robotic drilling." The International Journal of Advanced Manufacturing Technology **80**(9-12): 1903-1917.
- Nelson E. Claytor, D. M. C., Oscar M. Lechuga (2004). AN OVERVIEW OF FREEFORM OPTICS PRODUCTION. Proc. of ASPE Winter Top. Meeting,, North Carolina, USA.
- Olesch, E., C. Faber and G. Häusler (2011). Deflectometric Self-Calibration for arbitrary specular surface. Proc. DGao.
- Pagel, F. (2010). Calibration of non-overlapping cameras in vehicles. Intelligent Vehicles Symposium (IV), 2010 IEEE, IEEE.
- Pages, J., J. Salvi, R. Garcia and C. Matabosch (2003). Overview of coded light projection techniques for automatic 3D profiling. Robotics and Automation, 2003. Proceedings. ICRA'03. IEEE International Conference on, IEEE.
- Pan, J., P. S. Huang and F.-P. Chiang (2005). "Color-coded binary fringe projection technique for 3-D shape measurement." Optical Engineering **44**(2): 023606.
- Pan, J., P. S. Huang and F.-P. Chiang (2006). "Color phase-shifting technique for three-dimensional shape measurement." Optical Engineering **45**(1): 013602.

- Percoco, G., M. G. Guerra, A. J. S. Salmeron and L. M. Galantucci (2017). "Experimental investigation on camera calibration for 3D photogrammetric scanning of micro-features for micrometric resolution." The International Journal of Advanced Manufacturing Technology **91**(9-12): 2935-2947.
- Pettersson, B. (2009). Coordinate measuring machine, Google Patents.
- Petz, M., M. Fischer and R. Tutsch (2013). Systematic errors in deflectometry induced by use of liquid crystal displays as reference structure. Proc. 21st IMEKO TC2 Symp. on Photonics in Measurement.
- Petz, M. and R. Ritter (2001). Reflection grating method for 3D measurement of reflecting surfaces. Optical Measurement Systems for Industrial Inspection II: Applications in Production Engineering, International Society for Optics and Photonics.
- Petz, M. and R. Tutsch (2005). Reflection grating photogrammetry: a technique for absolute shape measurement of specular free-form surfaces. Proc. of SPIE.
- Petz, M. and R. Tutsch (2005). Reflection grating photogrammetry: a technique for absolute shape measurement of specular free-form surfaces. Optical Manufacturing and Testing VI, International Society for Optics and Photonics.
- Pollicove, H. M. (2000). Next-generation optics manufacturing technologies.
- Quan, C., W. Chen and C. Tay (2010). "Phase-retrieval techniques in fringe-projection profilometry." Optics and Lasers in Engineering **48**(2): 235-243.
- Rahimi, A., B. Dunagan and T. Darrell (2004). Simultaneous calibration and tracking with a network of non-overlapping sensors. null, IEEE.
- Rapp, H. H. (2012). Reconstruction of specular reflective surfaces using auto-calibrating deflectometry, KIT Scientific Publishing.
- Rastogi, P. and E. Hack (2014). Phase estimation in optical interferometry, CRC Press.
- Rathjen, C. (1995). "Statistical properties of phase-shift algorithms." Journal of the Optical Society of America A **12**(9): 1997-2008.
- Reich, C., R. Ritter and J. Thesing (1997). White light heterodyne principle for 3D-measurement.
- Ren, H., F. Gao and X. Jiang (2015). "Improvement of high-order least-squares integration method for stereo deflectometry." Applied optics **54**(34): 10249-10255.
- Ren, H., F. Gao and X. Jiang (2015). "Iterative optimization calibration method for stereo deflectometry." Optics express **23**(17): 22060-22068.
- Ren, H., F. Gao and X. Jiang (2016). "Least-squares method for data reconstruction from gradient data in deflectometry." Applied optics **55**(22): 6052-6059.

- Ritter, R. and R. Hahn (1983). "Contribution to analysis of the reflection grating method." Optics and Lasers in Engineering **4**(1): 13-24.
- Sagawa, R., M. Takatsuji, T. Echigo and Y. Yagi (2005). Calibration of lens distortion by structured-light scanning. Intelligent Robots and Systems, 2005.(IROS 2005). 2005 IEEE/RSJ International Conference on, IEEE.
- Saldner, H. O. and J. M. Huntley (1997). "Temporal phase unwrapping: application to surface profiling of discontinuous objects." Applied optics **36**(13): 2770-2775.
- Saldner, H. O. and J. M. Huntley (1997). "Temporal phase unwrapping: application to surface profiling of discontinuous objects." Appl. Opt. **36**(13): 2770-2775.
- Sandoz, P. (1997). "Wavelet transform as a processing tool in white-light interferometry." Optics letters **22**(14): 1065-1067.
- Santana-Cedr s, D., L. Gomez, M. Alem n-Flores, A. Salgado, J. Esclar n, L. Mazorra and L. Alvarez (2017). "Estimation of the lens distortion model by minimizing a line reprojection error." IEEE Sensors Journal **17**(9): 2848-2855.
- Sanz-Ablanedo, E., J. R. Rodr guez-P rez, J. Armesto and M. F.  . Taboada (2010). "Geometric stability and lens decentering in compact digital cameras." Sensors **10**(3): 1553-1572.
- Savio, E., L. De Chiffre and R. Schmitt (2007). "Metrology of freeform shaped parts." CIRP Annals - Manufacturing Technology **56**(2): 810-835.
- Schmalz, C., F. Forster and E. Angelopoulou (2011). "Camera calibration: active versus passive targets." Optical Engineering **50**(11): 113601.
- Schreiber, H. and J. H. Bruning (2007). "Phase shifting interferometry." Optical shop testing: 547-666.
- Sommargren, G. E. (1999). Phase shifting interferometer, Google Patents.
- Su, P., M. Khreishi, T. Su, R. Huang, M. Z. Dominguez, A. V. Maldonado, G. P. Butel, Y. Wang, R. E. Parks and J. H. Burge (2013). "Aspheric and freeform surfaces metrology with software configurable optical test system: a computerized reverse Hartmann test." Optical Engineering **53**(3): 031305.
- Su, P., R. E. Parks, L. Wang, R. P. Angel and J. H. Burge (2010). "Software configurable optical test system: a computerized reverse Hartmann test." Applied Optics **49**(23): 4404-4412.
- Su, P., Y. Wang, J. H. Burge, K. Kaznatcheev and M. Idir (2012). "Non-null full field X-ray mirror metrology using SCOTS: a reflection deflectometry approach." Optics Express **20**(11): 12393-12406.
- Takeda, M., H. Ina and S. Kobayashi (1982). "Fourier-transform method of fringe-pattern analysis for computer-based topography and interferometry." JosA **72**(1): 156-160.

- Tang, B., L. Zhou, Z. Xiong, J. Wang and M. Zhan (2014). "A programmable broadband low frequency active vibration isolation system for atom interferometry." Review of Scientific Instruments **85**(9): 093109.
- Tang, Y., X. Su, Y. Liu and H. Jing (2008). "3D shape measurement of the aspheric mirror by advanced phase measuring deflectometry." Optics express **16**(19): 15090-15096.
- Tang, Y., X. Su, F. Wu and Y. Liu (2009). "A novel phase measuring deflectometry for aspheric mirror test." Optics express **17**(22): 19778-19784.
- Tang, Z., R. G. von Gioi, P. Monasse and J.-M. Morel (2017). "A precision analysis of camera distortion models." IEEE Transactions on Image Processing **26**(6): 2694-2704.
- Thirithala, S. and M. Pollefeys (2005). Multi-view geometry of 1d radial cameras and its application to omnidirectional camera calibration. Computer Vision, 2005. ICCV 2005. Tenth IEEE International Conference on, IEEE.
- Thompson, J. P. R. a. K. P. (2012). Freeform optics: Evolution? No, revolution! SPIE Newsroom.
- Towers, C., D. Towers and J. Jones (2005). "Absolute fringe order calculation using optimised multi-frequency selection in full-field profilometry." Optics and Lasers in Engineering **43**(7): 788-800.
- Towers, C. E., D. P. Towers and J. D. C. Jones (2005). "Absolute fringe order calculation using optimised multi-frequency selection in full-field profilometry." Optics and Lasers in Engineering **43**(7): 788-800.
- Wang, Y., X. Chen, J. Tao, K. Wang and M. Ma (2016). "Accurate feature detection for out-of-focus camera calibration." Applied optics **55**(28): 7964-7971.
- Wei, Z. and K. Zhao (2016). "Structural parameters calibration for binocular stereo vision sensors using a double-sphere target." Sensors **16**(7): 1074.
- Weng, J., P. Cohen and M. Herniou (1992). "Camera calibration with distortion models and accuracy evaluation." IEEE Transactions on Pattern Analysis & Machine Intelligence(10): 965-980.
- Werling, S. B. (2011). Deflektometrie zur automatischen Sichtprüfung und Rekonstruktion spiegelnder Oberflächen, KIT Scientific Publishing.
- Whitehouse, D. J. (2002). Surfaces and their Measurement.
- Williamson, D. M. (2015). Freeforms in EUV Lithography Projection Optics. Imaging and Applied Optics 2015, Arlington, Virginia, Optical Society of America.
- Wissmann, P., R. Schmitt and F. Forster (2011). Fast and accurate 3D scanning using coded phase shifting and high speed pattern projection. 3D Imaging, Modeling, Processing, Visualization and Transmission (3DIMPVT), 2011 International Conference on, IEEE.

- Wu, Y., H. Yue, J. Yi, M. Li and Y. Liu (2015). "Phase error analysis and reduction in phase measuring deflectometry." Optical Engineering **54**(6): 064103.
- Wyant, J. C. (2002). White light interferometry. Holography: A Tribute to Yuri Denisyuk and Emmett Leith, International Society for Optics and Photonics.
- Wyant, J. C. (2003). "Dynamic Interferometry." Optics and Photonics News **14**(4): 36-41.
- Xiao, Y.-L., X. Su and W. Chen (2012). "Flexible geometrical calibration for fringe-reflection 3D measurement." Optics letters **37**(4): 620-622.
- Xiao, Y.-L., X. Su, W. Chen and Y. Liu (2012). "Three-dimensional shape measurement of aspheric mirrors with fringe reflection photogrammetry." Applied optics **51**(4): 457-464.
- Xiao, Y.-L., X. Su, W. Chen and Y. Liu (2012). "Three-dimensional shape measurement of aspheric mirrors with fringe reflection photogrammetry." Appl. Opt. **51**(4): 457-464.
- Xu, J., J. Douet, J. Zhao, L. Song and K. Chen (2013). "A simple calibration method for structured light-based 3D profile measurement." Optics & Laser Technology **48**: 187-193.
- Xu, J., S. Liu, A. Wan, B. Gao, Q. Yi, D. Zhao, R. Luo and K. Chen (2012). "An absolute phase technique for 3D profile measurement using four-step structured light pattern." Optics and Lasers in Engineering **50**(9): 1274-1280.
- Xu, Y., C. Chen, S. Huang and Z. Zhang (2014). "Simultaneously measuring 3D shape and colour texture of moving objects using IR and colour fringe projection techniques." Optics and Lasers in Engineering **61**: 1-7.
- Xu, Y., F. Gao and X. Jiang (2018). "Enhancement of measurement accuracy of optical stereo deflectometry based on imaging model analysis." Optics and Lasers in Engineering **111**: 1-7.
- Xu, Y., F. Gao, H. Ren, Z. Zhang and X. Jiang (2017). "An iterative distortion compensation algorithm for camera calibration based on phase target." Sensors **17**(6): 1188.
- Xu, Y., F. Gao, Z. Zhang and X. Jiang (2018). "A calibration method for non-overlapping cameras based on mirrored absolute phase target." The International Journal of Advanced Manufacturing Technology: 1-7.
- Xu, Y., F. Gao, Z. Zhang and X. Jiang (2018). "A holistic calibration method with iterative distortion compensation for stereo deflectometry." Optics and Lasers in Engineering **106**: 111-118.
- Xue, J., X. Su, L. Xiang and W. Chen (2012). "Using concentric circles and wedge grating for camera calibration." Applied optics **51**(17): 3811-3816.
- Yue, H., Y. Wu, B. Zhao, Z. Ou, Y. Liu and Y. Liu (2013). "A carrier removal method in phase measuring deflectometry based on the analytical carrier phase description." Optics express **21**(19): 21756-21765.

- Zhan, Q. and X. Wang (2012). "Hand-eye calibration and positioning for a robot drilling system." The International Journal of Advanced Manufacturing Technology **61**(5-8): 691-701.
- Zhang, G., J. He and X. Yang (2003). "Calibrating camera radial distortion with cross-ratio invariability." Optics & Laser Technology **35**(6): 457-461.
- Zhang, H., L. Ji, S. Liu, S. Li, S. Han and X. Zhang (2012). "Three-dimensional shape measurement of a highly reflected, specular surface with structured light method." Appl. Opt. **51**(31): 7724-7732.
- Zhang, S. (2010). "Recent progresses on real-time 3D shape measurement using digital fringe projection techniques." Optics and lasers in engineering **48**(2): 149-158.
- Zhang, S., D. Van Der Weide and J. Oliver (2010). "Superfast phase-shifting method for 3-D shape measurement." Optics express **18**(9): 9684-9689.
- Zhang, Z. (2000). "A flexible new technique for camera calibration." IEEE Transactions on pattern analysis and machine intelligence **22**.
- Zhang, Z. (2012). "Review of single-shot 3D shape measurement by phase calculation-based fringe projection techniques." Optics and Lasers in Engineering **50**(8): 1097-1106.
- Zhang, Z., C. E. Towers and D. P. Towers (2006). "Time efficient color fringe projection system for 3D shape and color using optimum 3-frequency selection." Optics express **14**(14): 6444-6455.
- Zhao, P., N. Gao, Z. Zhang, F. Gao and X. Jiang (2018). "Performance analysis and evaluation of direct phase measuring deflectometry." Optics and lasers in engineering **103**: 24-33.
- Zhao, W., X. Su, Y. Liu and Q. Zhang (2009). "Testing an aspheric mirror based on phase measuring deflectometry." Optical Engineering **48**(10): 103603.
- Zheng, D. and F. Da (2012). "Phase coding method for absolute phase retrieval with a large number of codewords." Optics express **20**(22): 24139-24150.
- Zorich, V. A. (2002). Mathematical Analysis I, Springer-Verlag Berlin Heidelberg.
- Zuo, C., Q. Chen, G. Gu, S. Feng, F. Feng, R. Li and G. Shen (2013). "High-speed three-dimensional shape measurement for dynamic scenes using bi-frequency tripolar pulse-width-modulation fringe projection." Optics and Lasers in Engineering **51**(8): 953-960.
- Zuo, C., L. Huang, M. Zhang, Q. Chen and A. Asundi (2016). "Temporal phase unwrapping algorithms for fringe projection profilometry: A comparative review." Optics and Lasers in Engineering **85**: 84-103.